technische universität
dortmund

Dissertation zur Erlangung des akademischen Grades
Dr. rer. nat.

Measurements of *CP* violation in decays of beauty mesons to two charmed mesons at the LHCb experiment

vorgelegt von
Louis Lenard Gerken
geboren in Witten

2024

Fakultät Physik
Technische Universität Dortmund

Der Fakultät Physik der Technischen Universität Dortmund zur Erlangung des akademischen Grades eines Dr. rer. nat. vorgelegte Dissertation.

1. Gutachter: Prof. Dr. Johannes Albrecht
2. Gutachter: PD Dr. Dominik Elsässer

Abstract

In this thesis, two measurements of *CP* violation in the $B \to D\overline{D}$ system are presented. Both analyses explore proton-proton collision data corresponding to an integrated luminosity of $6\,\text{fb}^{-1}$ collected by the LHCb experiment at a centre-of-mass energy of 13 TeV. The flavour-tagged decay-time-dependent analysis of about 5 700 $B^0 \to D^+D^-$ signal candidates yields the *CP* observables

$$\begin{aligned} S_{D^+D^-} &= -0.552 \pm 0.100\,(\text{stat}) \pm 0.010\,(\text{syst})\,, \\ C_{D^+D^-} &= 0.128 \pm 0.103\,(\text{stat}) \pm 0.010\,(\text{syst})\,. \end{aligned}$$

In the second measurement, approximately 13 000 $B_s^0 \to D_s^+D_s^-$ signal candidates are selected, and the *CP* observables are determined to be

$$\begin{aligned} \phi^{\text{eff}}_{s,D_s^+D_s^-} &= -0.086 \pm 0.106\,(\text{stat}) \pm 0.028\,(\text{syst})\,\text{rad}\,, \\ |\lambda_{D_s^+D_s^-}| &= 1.145 \pm 0.126\,(\text{stat}) \pm 0.031\,(\text{syst})\,. \end{aligned}$$

These results represent the most precise measurements of *CP* violation in their respective channels to date and are consistent with Standard Model predictions. For the first time, *CP* symmetry in $B^0 \to D^+D^-$ decays is excluded by a single measurement with a significance of more than six standard deviations.

Kurzfassung

In dieser Arbeit werden zwei Messungen von *CP*-Verletzung im $B \to D\overline{D}$ System vorgestellt. Beide Analysen verwenden Daten des LHCb-Experiments, welche einer integrierten Luminosität von $6\,\text{fb}^{-1}$ entsprechen und in Proton-Proton Kollisionen bei einer Schwerpunktsenergie von 13 TeV aufgezeichnet wurden. Die zerfallszeitabhängige Analyse von etwa 5 700 $B^0 \to D^+D^-$ Signalkandidaten ergibt

$$\begin{aligned} S_{D^+D^-} &= -0.552 \pm 0.100\,(\text{stat}) \pm 0.010\,(\text{syst})\,, \\ C_{D^+D^-} &= 0.128 \pm 0.103\,(\text{stat}) \pm 0.010\,(\text{syst})\,. \end{aligned}$$

In der zweiten Messung werden etwa 13 000 $B_s^0 \to D_s^+D_s^-$ Signalkandidaten selektiert, und die Messung der *CP*-Observablen ergibt

$$\begin{aligned} \phi^{\text{eff}}_{s,D_s^+D_s^-} &= -0.086 \pm 0.106\,(\text{stat}) \pm 0.028\,(\text{syst})\,\text{rad}\,, \\ |\lambda_{D_s^+D_s^-}| &= 1.145 \pm 0.126\,(\text{stat}) \pm 0.031\,(\text{syst})\,. \end{aligned}$$

Diese Ergebnisse stellen die bisher präzisesten Messungen von *CP*-Verletzung in den jeweiligen Zerfallskanälen dar und sind kompatibel mit Vorhersagen des Standardmodells. Zum ersten Mal kann *CP*-Symmetrie in $B^0 \to D^+D^-$ Zerfällen durch eine einzelne Messung mit einer Signifikanz von mehr als sechs Standardabweichungen ausgeschlossen werden.

Table of Contents

1 Introduction

In the past century, our understanding of the universe has been revolutionised by the development of the Standard Model of particle physics (SM) [1–3]. The SM is a quantum field theory that describes the fundamental particles and their interactions. This model has been proven to accurately describe nature on the smallest scales to exceptional precision. With the discovery of the Higgs boson in 2012 [4,5], all particles predicted by the SM have been found. Despite its success, the SM is known to be incomplete. Observations of neutrino oscillations [6, 7] indicate that neutrinos have mass, while in the SM they are assumed to be massless. Cosmological measurements show that only 5% of the energy content of the universe is described by the SM. The remaining 95% are attributed to dark matter and dark energy [8]. However, even the existence of the 5% ordinary matter raises another interesting question. According to our current understanding of the universe, equal amounts of matter and antimatter should have been created after the Big Bang. Still, there is no sign of large-scale antimatter clusters that could compensate for the observed matter in the universe. In 1967, Sakharov proposed three necessary conditions to produce such an imbalance of matter and antimatter in the early universe [9]. The baryon number conservation has to be violated, departure from thermal equilibrium is required, and finally, C and CP symmetries have to be violated.

Both C and CP violation have been observed in the weak interaction and are well established in the SM [10, 11]. Nevertheless, no theory has been able to explain the matter-antimatter asymmetry in the universe with the observed amount of CP violation [12]. In the SM, the violation of CP symmetry is manifested by a complex phase in the Cabibbo-Kobayashi-Maskawa (CKM) matrix, which is a unitary matrix that describes the transitions between different quark flavours. The unitarity of the CKM matrix is a fundamental property, and any deviation would indicate the presence of New Physics beyond the SM. Hence, the test of the unitarity conditions is an excellent test of the SM. The so-called unitarity triangles are a geometric representation of these conditions, which are tested by measuring the angles and side lengths of the triangles. One of these angles, the angle β_s, is particularly interesting, as it has a very precise prediction [13]. It is predicted to be small and has been measured with high precision in $B_s^0 \to J/\psi\phi$, $B_s^0 \to J/\psi K^+K^-$ and $B_s^0 \to J/\psi\pi^+\pi^-$ decays [14–18]. However, with increasing experimental precision, higher-order SM corrections become the limiting factor in measurements of β_s. These contributions have to be constrained to distinguish them from potential New Physics effects, which is a major challenge in most decay modes. In the measurement of β_s using $B_s^0 \to D_s^+D_s^-$ decays this can be accomplished by measuring

U-spin-related decays [19–23]. In particular, the measurement of the CKM angle β in $B^0 \to D^+D^-$ decays is of great interest. Although this measurement cannot compete with the precision achieved by β measurements using $B^0 \to J/\psi K^0_S$ decays, the significant contribution of higher-order effects can be determined. This allows for the control of similar contributions in the $B^0_s \to D^+_s D^-_s$ measurement within a global analysis that includes various *CP*-violation and branching-fraction measurements in the $B \to D\overline{D}$ system [23].

In this thesis, the measurements of *CP* violation in $B^0 \to D^+D^-$ and $B^0_s \to D^+_s D^-_s$ decays are presented [24]. The two decay modes are analysed in parallel to exploit the similarities of the two decays. A data set collected by the LHCb experiment at the LHC is analysed. The LHCb experiment conducts precision measurements, which can reveal New Physics effects through loop processes at a much higher energy scale than the LHC centre-of-mass energy. It is designed for measurements in decays of b and c hadrons and is therefore well suited for measuring *CP* violation with extraordinary precision. The analyses use proton-proton collision data recorded during the years 2015–2018 at a centre-of-mass energy of 13 TeV. The data set corresponds to an integrated luminosity of $6\,\text{fb}^{-1}$.

This thesis is structured as follows: The origin of *CP* violation in the SM, with particular focus on the $B \to D\overline{D}$ system, is explained in Chap. 2. In Chap. 3, the LHCb experiment is introduced and the methods used in this analysis are described in Chap. 4. The strategy of decay-time-dependent *CP*-violation measurements is discussed in Chap. 5. Measurements-specific considerations and the results of the $B^0 \to D^+D^-$ and $B^0_s \to D^+_s D^-_s$ analyses are presented in Chap. 6 and Chap. 7, respectively. Finally, the results are summarised in Chap. 8, and the possibilities for future measurements are discussed.

2 Origin of *CP* violation in the Standard Model

In this chapter, the Standard Model of particle physics [1–3] is introduced and the origin of *CP* violation within this theory is explained. The fundamental particles and their interactions are described in Sec. 2.1 based on Ref. [25, 26]. Symmetries, which play a crucial role in the SM, are discussed in Sec. 2.2. The violation of *CP* symmetry in the SM is introduced by the CKM mechanism as explained in Sec. 2.3. The time evolution of the neutral B mesons is described in Sec. 2.4. In Sec. 2.5, an overview of the three manifestations of *CP* violation is given. Sections 2.3 to 2.5 are based on Refs. [27–32]. Finally, Sec. 2.6 describes how *CP* violation is measured in the $B \to D\overline{D}$[1] decays based on Ref. [19].

2.1 Fundamental particles and interactions

The SM is a quantum field theory that describes the fundamental particles and their interactions. The particles are represented by quantum fields and the dynamics are described by a Lagrangian density. An overview of the fundamental particles is shown in Fig. 2.1. The SM comprises fermions with spin 1/2, gauge bosons with spin one and the Higgs boson with spin zero. Each fermion, f, has an associated antiparticle, $\overline{f}$, with inverted quantum numbers.

The fermions form the known matter of the universe and are divided into six quarks and six leptons. The three up-type quarks (u, c, t) have an electric charge of $+2/3\,e$, and the three down-type quarks (d, s, b) have an electric charge of $-1/3\,e$, where e is the elementary charge. Additionally, the quarks carry a colour charge and can interact via the strong force. Due to confinement [34], they always occur in colour-neutral bound states, which are called hadrons. Baryons are hadrons that are composed of three quarks. The most widely known baryons are the proton and the neutron, which consist of u and d quarks. They are the building blocks of atomic nuclei. Additionally, there are colourless states comprised of a quark and an antiquark called mesons. The B^0 meson, which is of particular interest in this thesis, consists of a $\overline{b}$ and a d quark. Exotic four-quark states have been discovered by the Belle experiment [35]. Later, the LHCb experiment has observed additional four-quark states [36, 37] and the first five-quark states [38, 39].

[1] Throughout this thesis, B refers to the neutral B^0 and B_s^0 mesons and D to the charged $D^\pm$ and $D_s^\pm$ mesons

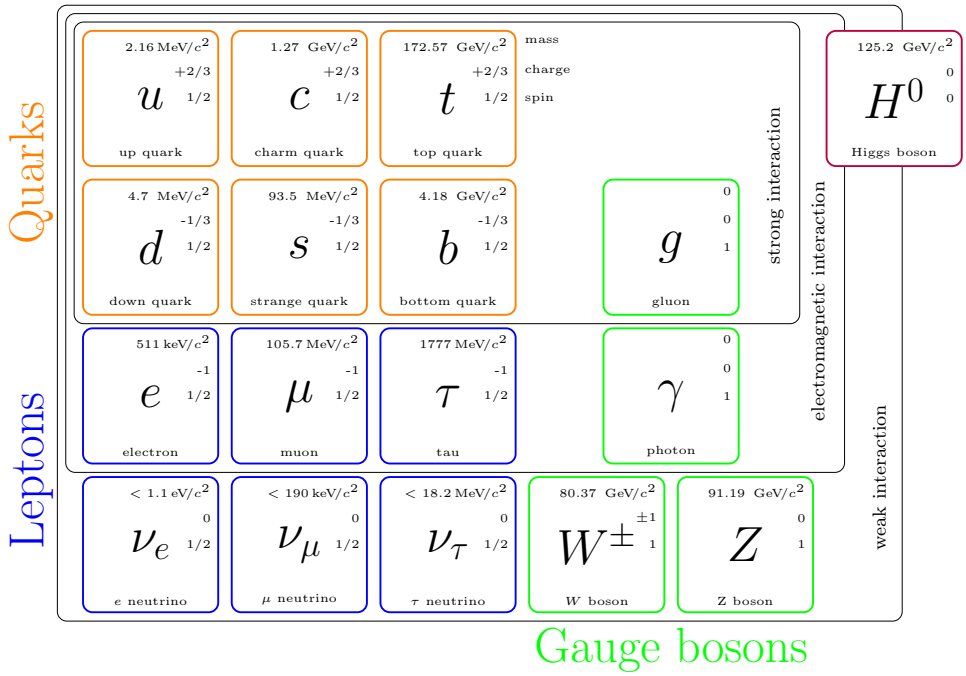

Figure 2.1: Overview of the fundamental particles of the SM. The properties are taken from the Ref. [33].

The leptons are divided into three charged leptons and three neutral neutrinos. The charged leptons have an electric charge of $-1\,e$ and are massive particles, while the neutrinos are assumed to be massless in the SM. However, neutrinos are known to have a mass, which is a consequence of the observed neutrino mixing [6, 7]. In contrast to the quarks, leptons do not carry a colour charge and thus cannot interact via the strong force. All fermions are grouped into three generations with increasing mass.

The gauge bosons are the mediators of the fundamental forces. Eight massless gluons mediate the strong interaction and couple to the colour charge. They carry colour charge themselves and can interact with each other. The massless photon mediates the electromagnetic interaction. It couples to the electric charge and is itself electrically neutral. The weak force is mediated by the $W^{\pm}$ and Z bosons. They are the only massive gauge bosons and couple to left-handed particles and right-handed antiparticles.

Finally, the Higgs boson, H^0, is a scalar particle introduced as a consequence of the Higgs mechanism [40, 41]. It was discovered in 2012 by the ATLAS and CMS collaborations [4, 5]. The Higgs mechanism is responsible for the masses of the $W^{\pm}$ and Z bosons. Section 2.3 explains how the Yukawa interaction with the Higgs field generates the masses of the fermions and enables *CP* violation in the weak interaction.

2.2 Symmetries

Symmetries are a key concept in physics. They are associated with conservation laws according to Noether's theorem [42]. In the SM, they play a crucial role in the description of the fundamental forces, which are the consequence of local gauge symmetries.

This thesis focuses on symmetries under the three discrete transformations C, P and T. The charge conjugation C transforms all particles into their antiparticles, $\psi(\vec{x},t) \rightarrow \overline{\psi}(\vec{x},t)$. The parity transformation P inverts the spatial coordinates, $\psi(\vec{x},t) \rightarrow \psi(-\vec{x},t)$, and the time coordinate is inverted by the time reversal T, $\psi(\vec{x},t) \rightarrow \psi(\vec{x},-t)$. According to the *CPT* theorem [43, 44] the combined *CPT* symmetry is conserved in the SM. While the electromagnetic interaction is invariant under the C and P transformations, the strong and weak interactions are allowed to violate these symmetries. In 1957, the violation of P symmetry in the weak interaction was observed in β decays by Wu et al. [10]. Here, the combined *CP* symmetry was still believed to be conserved. However, in 1964, *CP* violation was discovered in the neutral kaon system [11]. Later, *CP* violation was observed in B^0 decays by the BaBar and Belle collaborations [45,46] and in B_s^0 decays by the LHCb collaboration [47]. In 2019, the LHCb collaboration reported the first observation of *CP* violation in the charm system [48]. To this day, no violation of *CP* symmetry has been observed in the strong interaction. The mechanism that embeds the *CP* violation in the SM is the CKM mechanism described in the following.

2.3 The CKM mechanism

The *CP* violation in the SM is caused by the complex phase of the CKM matrix. The CKM matrix describes the quark mixing and enables transitions between different quark generations. In the following, the CKM matrix is derived from the Yukawa interaction between the quarks and the Higgs field using the notation of Ref. [33].

The Lagrangian of the Yukawa interaction between quarks and the Higgs field ϕ is given by

$$\mathcal{L}_{\text{Yukawa}} = -Y_{ij}^{d}\overline{Q_{Li}^{I}}\phi d_{Rj}^{I} - Y_{ij}^{u}\overline{Q_{Li}^{I}}\epsilon\phi^{*}u_{Rj}^{I} + \text{h.c.}\,, \tag{2.1}$$

where $Y^{u,d}$ are complex 3×3 matrices, Q_L^I are the left-handed quark doublets, d_R^I and u_R^I are the right-handed quark singlets, i and j are the generation indices and ϵ is the 2×2 antisymmetric tensor. The mass terms for the quarks are obtained by the substitution of the Higgs doublet with its vacuum expectation value $\langle\phi\rangle = (0, \nu/\sqrt{2})$, which yields

$$\mathcal{L}_{\text{mass}} = -Y_{ij}^{d}\overline{d_{Li}^{I}}d_{Rj}^{I}\frac{\nu}{\sqrt{2}} - Y_{ij}^{u}\overline{u_{Li}^{I}}u_{Rj}^{I}\frac{\nu}{\sqrt{2}} + \text{h.c.}\,. \tag{2.2}$$

Unitary transformations of the quark fields

$$\begin{aligned} u^I_{L,R} &\to V^u_{L,R} u^I_{L,R}\,, \\ d^I_{L,R} &\to V^d_{L,R} d^I_{L,R}\,, \end{aligned} \tag{2.3}$$

are introduced and chosen such that the mass terms

$$M^{u,d}_{\text{diag}} = V^{u,d}_L Y^{u,d} V^{u,d\dagger}_R \frac{\nu}{\sqrt{2}}\,, \tag{2.4}$$

are diagonal. The Lagrangian of the charged current interaction mediated by the $W^\pm$ bosons can be written in terms of the quark mass eigenstates

$$\mathcal{L}_{\text{CC}} = -\frac{g}{\sqrt{2}} (\overline{u_L}, \overline{c_L}, \overline{t_L}) \gamma^\mu W^+_\mu V_{\text{CKM}} \begin{pmatrix} d_L \\ s_L \\ b_L \end{pmatrix} + \text{h.c.}\,, \tag{2.5}$$

with the Dirac matrices, γ^μ, the weak coupling constant, g, and the CKM matrix

$$V_{\text{CKM}} = V^u_L V^{d\dagger}_L = \begin{pmatrix} V_{ud} & V_{us} & V_{ub} \\ V_{cd} & V_{cs} & V_{cb} \\ V_{td} & V_{ts} & V_{tb} \end{pmatrix}. \tag{2.6}$$

The CKM matrix is a complex 3×3 matrix that describes the mixing between the quark mass eigenstates and the eigenstates of the weak interaction. Since $V^{u,d}$ are unitary matrices, the CKM matrix itself is unitary. It enables transitions between different quark generations. Due to the unitarity and the invariance under rephasing of the quark fields, the CKM matrix has only four independent parameters. The standard parameterisation was proposed by Chau and Keung [49]. In this parameterisation, the CKM matrix is defined as

$$V_{\text{CKM}} = \begin{pmatrix} c_{12}c_{13} & s_{12}c_{13} & s_{13}e^{-i\delta} \\ -s_{12}c_{23} - c_{12}s_{23}s_{13}e^{i\delta} & c_{12}c_{23} - s_{12}s_{23}s_{13}e^{i\delta} & s_{23}c_{13} \\ s_{12}s_{23} - c_{12}c_{23}s_{13}e^{i\delta} & -c_{12}s_{23} - s_{12}c_{23}s_{13}e^{i\delta} & c_{23}c_{13} \end{pmatrix}, \tag{2.7}$$

where $c_{ij} = \cos\theta_{ij}$ and $s_{ij} = \sin\theta_{ij}$ with the Euler angles θ_{12}, θ_{13} and θ_{23} and one overall phase δ. The phase δ is the only source of *CP* violation in the SM. Transitions within quark generations are highly favoured, and it is convenient to use the Wolfenstein parametrisation [50] to represent this hierarchy. Therefore, the CKM matrix is expressed in terms of

$$\begin{aligned} s_{12} &= \lambda\,, \\ s_{23} &= A\lambda^2\,, \\ s_{13}\exp^{i\delta} &= A\lambda^3\rho\,, \end{aligned} \tag{2.8}$$

and the expansion in powers of λ up to $\mathcal{O}(\lambda^4)$ is given by

$$V_{\text{CKM}} = \begin{pmatrix} 1 - \frac{\lambda^2}{2} & \lambda & A\lambda^3(\rho - i\eta) \\ -\lambda & 1 - \frac{\lambda^2}{2} & A\lambda^2 \\ A\lambda^3(1 - \rho - i\eta) & -A\lambda^2 & 1 \end{pmatrix} + \mathcal{O}(\lambda^4)\,. \tag{2.9}$$

The unitarity of the CKM matrix imposes the following conditions

$$\sum_{i=u,c,t} V_{ij}V_{ik}^* = \delta_{jk} \text{ and } \sum_{j=d,s,b} V_{ij}V_{kj}^* = \delta_{ik}\,. \tag{2.10}$$

The off-diagonal conditions can be represented as so-called unitarity triangles in the complex plane. All unitarity triangles have the same area, which is equal to half of the Jarlskog invariant J [51]. This phase-convention-independent quantity, defined by

$$J\sum_{m,n}\epsilon_{ikm}\epsilon_{jln} = \text{Im}\left(V_{ij}V_{kl}V_{il}^*V_{kj}^*\right)\,. \tag{2.11}$$

is a measure of the *CP* violation in the SM.

The most prominent unitarity triangle corresponds to the condition

$$\begin{aligned} V_{ud}V_{ub}^* + V_{cd}V_{cb}^* + V_{td}V_{tb}^* &= 0\,, \\ \Leftrightarrow \frac{V_{ud}V_{ub}^*}{V_{cd}V_{cb}^*} + \quad 1 \quad + \frac{V_{td}V_{tb}^*}{V_{cd}V_{cb}^*} &= 0\,, \end{aligned} \tag{2.12}$$

where the side represented by $V_{cd}V_{cb}^*$ is chosen as the base of the triangle. This choice fixes two vertices at $(0,0)$ and $(1,0)$, while the apex is at $(\bar{\rho},\bar{\eta})$. In contrast to the other unitarity triangles, its side lengths are of similar size. This, and the fact that its properties can be measured in B^0 decays, makes this triangle an interesting choice for *CP*-violation studies. The unitarity condition can be tested by measuring the angles

$$\alpha = \arg\left(-\frac{V_{td}V_{tb}^*}{V_{ud}V_{ub}^*}\right)\,, \quad \beta = \arg\left(-\frac{V_{cd}V_{cb}^*}{V_{td}V_{tb}^*}\right)\,, \quad \gamma = \arg\left(-\frac{V_{ud}V_{ub}^*}{V_{cd}V_{cb}^*}\right)\,, \tag{2.13}$$

and the side lengths

$$R_b = \left|\frac{V_{ud}V_{ub}^*}{V_{cd}V_{cb}^*}\right|\,, \quad R_t = \left|\frac{V_{td}V_{tb}^*}{V_{cd}V_{cb}^*}\right|\,. \tag{2.14}$$

New Physics can be revealed if the triangle does not close at the apex. The triangle with the current experimental constraints is shown in Fig. 2.2.

In the B_s^0 system, the properties of the triangle corresponding to the condition

$$V_{us}V_{ub}^* + V_{cs}V_{cb}^* + V_{ts}V_{tb}^* = 0\,, \tag{2.15}$$

can be measured. It is shown in Fig. 2.3. The angle

$$\beta_s = \arg\left(-\frac{V_{ts}V_{tb}^*}{V_{cs}V_{cb}^*}\right)\,, \tag{2.16}$$

is of particular interest. Its precise SM prediction [13] makes β_s a promising observable for the search of New Physics effects.

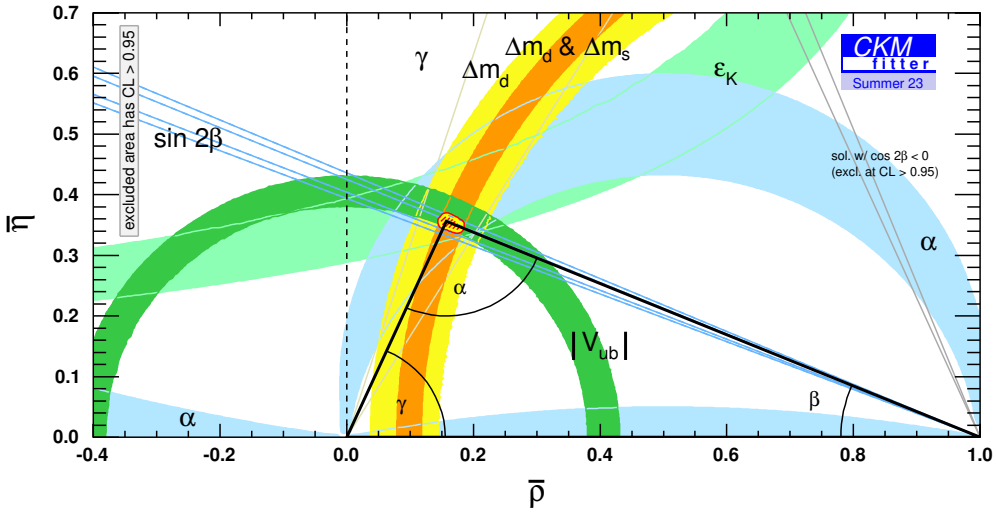

Figure 2.2: Unitarity triangle corresponding to the unitarity condition in Eq. (2.12) and its current experimental constraints. The figure is taken from Ref. [52].

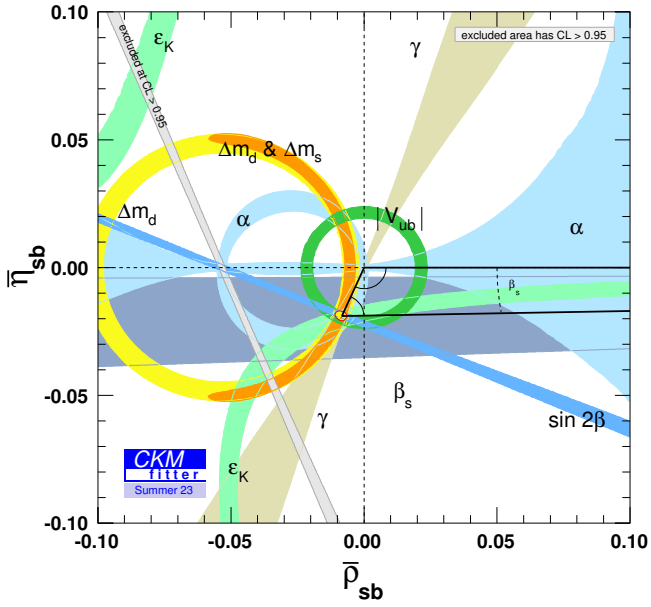

Figure 2.3: Unitarity triangle corresponding to the unitarity condition in Eq. (2.15) and its current experimental constraints. The figure is taken from Ref. [52].

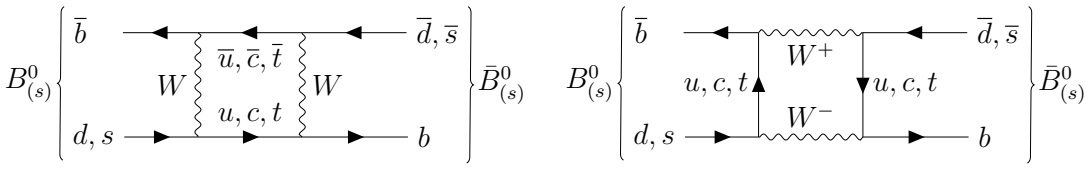

Figure 2.4: Dominant box diagrams contribution to the mixing of neutral B mesons.

2.4 Time evolution of neutral B mesons

The mixing of the quarks through the weak interaction enables the oscillations of neutral B mesons between B and $\overline{B}$ states. This is governed by the box diagrams shown in Fig. 2.4. For measurements involving neutral B-meson decays, it is essential to describe the time evolution of the system.

Different neutral states are used to describe the time evolution of the neutral B mesons. The flavour eigenstates are states of definite quark content and are useful to describe the production of the mesons. The time evolution is described by the Schrödinger-like equation

$$i\frac{\mathrm{d}}{\mathrm{d}t}\begin{pmatrix}|B(t)\rangle\\|\overline{B}(t)\rangle\end{pmatrix} = \mathcal{H}\begin{pmatrix}|B(t)\rangle\\|\overline{B}(t)\rangle\end{pmatrix} . \tag{2.17}$$

The Hamiltonian, $\mathcal{H}$, is not Hermitian because the B mesons can decay. However, it can be written as

$$\mathcal{H} = M - \frac{i}{2}\Gamma = \begin{pmatrix}M_{11} - \frac{i}{2}\Gamma_{11} & M_{12} - \frac{i}{2}\Gamma_{12}\\ M_{21} - \frac{i}{2}\Gamma_{21} & M_{22} - \frac{i}{2}\Gamma_{22}\end{pmatrix} , \tag{2.18}$$

with the Hermitian mass and the decay matrix M and Γ. Imposing CPT invariance requires

$$M_{11} = M_{22} \quad \text{and} \quad \Gamma_{11} = \Gamma_{22} \tag{2.19}$$

to ensure that B and $\overline{B}$ mesons have the same mass and lifetime. The non-zero off-diagonal elements are responsible for the oscillation between the two flavour states. Thus, a pure $|B\rangle$ or $|\overline{B}\rangle$ state will eventually evolve into a mixture of $|B\rangle$ and $|\overline{B}\rangle$. The eigenstates of the Hamiltonian are used to describe the time evolution of the system. These are called mass eigenstates because they have a definite mass and lifetime. The mass eigenstates can be written as a linear combination of the flavour eigenstates

$$\begin{aligned}|B_L\rangle &= p\,|B\rangle + q\,|\overline{B}\rangle ,\\ |B_H\rangle &= p\,|B\rangle - q\,|\overline{B}\rangle ,\end{aligned} \tag{2.20}$$

with $|p|^2 + |q|^2 = 1$. Calculating the eigenvalues of the Hamiltonian yields the ratio of the coefficients

$$\frac{q}{p} = \sqrt{\frac{M_{12}^* - \frac{i}{2}\Gamma_{12}^*}{M_{12} - \frac{i}{2}\Gamma_{12}}} . \tag{2.21}$$

Equation (2.17) with the diagonalised Hamiltonian yields the time evolution of the mass eigenstates

$$|B_{L,H}(t)\rangle = e^{-(iM_{L,H}+\Gamma_{L,H}/2)t}\,|B_{L,H}\rangle \tag{2.22}$$

with the eigenvalues $M_{L,H} - i\Gamma_{L,H}/2$. Using Eq. (2.20) a state initially produced as a pure $|B\rangle$ or $|\overline{B}\rangle$ state at $t = 0$ evolves in time according to

$$\begin{aligned} |B(t)\rangle &= \frac{|B_L(t)\rangle + |B_H(t)\rangle}{2p}\,, \\ |\overline{B}(t)\rangle &= \frac{|B_L(t)\rangle - |B_H(t)\rangle}{2q}\,. \end{aligned} \tag{2.23}$$

The time evolution of the mass eigenstates can be substituted using Eq. (2.22). Expressing the mass eigenstates in terms of the flavour eigenstates using Eq. (2.20) yields the time evolution

$$\begin{aligned} |B(t)\rangle &= g_+(t)\,|B\rangle + \frac{q}{p} g_-(t)\,|\overline{B}\rangle\ , \\ |\overline{B}(t)\rangle &= \frac{p}{q} g_-(t)\,|B\rangle + g_+(t)\,|\overline{B}\rangle\ , \end{aligned} \tag{2.24}$$

with

$$\begin{aligned} g_+(t) &= \frac{e^{-(iM_L+\Gamma_L/2)t} + e^{-(iM_H+\Gamma_H/2)t}}{2}\,, \\ g_-(t) &= \frac{e^{-(iM_L+\Gamma_L/2)t} - e^{-(iM_H+\Gamma_H/2)t}}{2}\,. \end{aligned} \tag{2.25}$$

The mean and difference of the mass and decay width

$$\begin{aligned} m &= \frac{M_H + M_L}{2}\,, & \Gamma &= \frac{\Gamma_L + \Gamma_H}{2}, \\ \Delta m &= M_H - M_L\,, & \Delta\Gamma &= \Gamma_L - \Gamma_H\,, \end{aligned} \tag{2.26}$$

are introduced and Eq. (2.25) can be written as

$$\begin{aligned} g_+(t) &= e^{-imt}\exp^{-\Gamma t/2}\left[\ \ \cos\frac{\Delta m}{2}t\cosh\frac{\Delta\Gamma}{4}t - i\sin\frac{\Delta m}{2}t\sinh\frac{\Delta\Gamma}{4}t\right]\,, \\ g_-(t) &= e^{-imt}\exp^{-\Gamma t/2}\left[-\cos\frac{\Delta m}{2}t\sinh\frac{\Delta\Gamma}{4}t + i\sin\frac{\Delta m}{2}t\cosh\frac{\Delta\Gamma}{4}t\right]\,. \end{aligned} \tag{2.27}$$

To calculate the time-dependent decay rates, the decay amplitudes

$$A_f = \langle f|B\rangle\ , \quad \overline{A}_f = \langle f|\overline{B}\rangle\ , \tag{2.28}$$

and the parameter

$$\lambda_f = \eta_{CP}\frac{q}{p}\frac{\bar{A}_f}{A_f}\,, \tag{2.29}$$

are introduced, where $\eta_{CP} = \pm 1$ is the *CP* eigenvalue of the final state f, which is reachable from both B and $\overline{B}$ mesons. Using these definitions, the time-dependent decay rates are given by

$$\begin{aligned}\Gamma(B(t)\to f) &= |\langle f|B(t)\rangle|^2 \propto \quad |A_f|^2(1+|\lambda_f|^2)e^{-\Gamma t} \\ &\left[\cosh\frac{\Delta\Gamma t}{2} + D\sinh\frac{\Delta\Gamma t}{2} + C\cos\Delta m t - S\sin\Delta m t\right], \\ \Gamma(\overline{B}(t)\to f) &= |\langle f|\overline{B}(t)\rangle|^2 \propto \left|\frac{p}{q}\right|^2 |A_f|^2(1+|\lambda_f|^2)e^{-\Gamma t} \\ &\left[\cosh\frac{\Delta\Gamma t}{2} + D\sinh\frac{\Delta\Gamma t}{2} - C\cos\Delta m t + S\sin\Delta m t\right].\end{aligned} \tag{2.30}$$

The *CP* observables are defined as

$$D = -\frac{2\,\mathrm{Re}(\lambda_f)}{1+|\lambda_f|^2}, \quad C = \frac{1-|\lambda_f|^2}{1+|\lambda_f|^2}, \quad S = \frac{2\,\mathrm{Im}(\lambda_f)}{1+|\lambda_f|^2}, \tag{2.31}$$

and fulfil the normalisation condition

$$D^2 + C^2 + S^2 = 1. \tag{2.32}$$

These *CP* observables are related to the CKM matrix elements. The relation between the *CP* observables in the $B\to D\overline{D}$ system and the properties of the CKM triangles is discussed in Sec. 2.6.

2.5 Manifestations of *CP* violation

CP violation in the SM can be divided into three categories. In the following, the quantities related to the different types of *CP* violation are introduced, and the measurement strategies are discussed.

2.5.1 *CP* violation in the decay

The quantity to measure *CP* violation in the decay is the ratio of the amplitudes

$$\left|\frac{\bar{A}_{\bar{f}}}{A_f}\right| = \left|\frac{\sum_i A_i e^{i(\delta_i-\phi_i)}}{\sum_i A_i e^{i(\delta_i+\phi_i)}}\right|, \tag{2.33}$$

where δ_i are the strong phases, ϕ_i are the weak phases and A_i is the magnitude of the individual amplitudes, i, contributing to the decay. Weak phases change the sign under the *CP* transformation and thus appear with different signs in the two amplitudes, while the strong phases do not change the sign. *CP* symmetry is violated when $\left|\bar{A}_{\bar{f}}/A_f\right| \neq 1$. The ratio is independent of phase conventions, and

for *CP* symmetry to be violated, at least two amplitudes with different weak and strong phases are required. This becomes apparent when calculating

$$|A_f|^2 - |\bar{A}_{\bar{f}}|^2 = -2\sum_{i,j} A_i A_j \sin(\phi_i - \phi_j)\sin(\delta_i - \delta_j)\,. \tag{2.34}$$

Experimentally, the amplitude ratio is usually measured using the charged $B^{\pm}$ mesons to avoid contributions from mixing. Hence, any asymmetry in

$$a_f = \frac{\Gamma(B^+ \to f) - \Gamma(B^- \to \bar{f})}{\Gamma(B^+ \to f) + \Gamma(B^- \to \bar{f})} = \frac{1 - \left|\frac{\bar{A}_{\bar{f}}}{A_f}\right|^2}{1 + \left|\frac{\bar{A}_{\bar{f}}}{A_f}\right|^2}\,, \tag{2.35}$$

is caused by *CP* violation in the decay.

2.5.2 *CP* violation in the mixing

In decays of neutral mesons, the mixing enables additional manifestations of *CP* violation. *CP* violation in the mixing refers to different rates of $B \to \overline{B}$ and $\overline{B} \to B$ transitions. Equation (2.24) shows that the difference between these transitions is purely driven by the ratio q/p. Thus, the rate difference depends on $|q/p|^2$. *CP* violation in the mixing is present when the mass eigenstates are not *CP* eigenstates, which leads to $|q/p| \neq 1$. Asymmetries in semi-leptonic B decays can be used to measure *CP* violation in the mixing via

$$a_{\mathrm{sl}}(t) = \frac{\Gamma(\overline{B}(t) \to f) - \Gamma(B(t) \to \bar{f})}{\Gamma(\overline{B}(t) \to f) + \Gamma(B(t) \to \bar{f})} = \frac{1 - \left|\frac{q}{p}\right|^4}{1 + \left|\frac{q}{p}\right|^4}\,. \tag{2.36}$$

While *CP* violation in the kaon mixing was already observed in 1964 [11], the effect in the B system is expected to be small. The current experimental precision is not yet sufficient to measure any significant deviation of $|q/p|$ from unity [53].

2.5.3 *CP* violation in the interference of mixing and decay

In decays where the final state is a *CP* eigenstate and is accessible in B and $\overline{B}$ decays, *CP* violation can arise in the interference of mixing and decay. The quantity to measure this effect, λ_f, was already introduced in Eq. (2.29). *CP* violation in the interference implies $\lambda_f \neq \pm 1$. This is possible even if *CP* is conserved in the decay and mixing ($|\lambda_f| = 1$) if λ_f has a non-zero imaginary part. The time-dependent *CP* asymmetry can be measured by

$$a_{f_{CP}}(t) = \frac{\Gamma(B(t) \to f_{CP}) - \Gamma(\overline{B}(t) \to f_{CP})}{\Gamma(B(t) \to f_{CP}) + \Gamma(\overline{B}(t) \to f_{CP})}\,. \tag{2.37}$$

Using the decay rates from Eq. (2.30) and neglecting *CP* violation in the mixing, the asymmetry can be written in terms of the *CP* observables

$$a_{f_{CP}}(t) = \frac{C\cos\Delta mt - S\sin\Delta mt}{\cosh\frac{\Delta\Gamma t}{2} + D\sinh\frac{\Delta\Gamma t}{2}}\,. \tag{2.38}$$

Equation (2.31) shows that this asymmetry vanishes if $\lambda_f = 1$.

2.6 *CP* violation in $B^0 \to D^+D^-$ and $B_s^0 \to D_s^+D_s^-$ decays

An exciting field to study *CP* violation in the interference is the B to double charm system. In this thesis, the decays $B^0 \to D^+D^-$ and $B_s^0 \to D_s^+D_s^-$ are studied. The final states D^+D^- and $D_s^+D_s^-$ are both *CP* eigenstates with *CP* eigenvalues $\eta_{CP} = 1$. The tree-level $b \to c\bar{c}d$ and $b \to c\bar{c}s$ quark transitions are sensitive to different angles of the unitarity triangles. A unique property of these decays is the control over higher-order SM contributions, explained in the following.

In Fig. 2.5, the dominant Feynman diagrams contributing to the decays are shown. The higher-order contributions arise due to the penguin diagrams. Hence, these contributions are often referred to as penguin pollution. The two decay channels are very similar, with the only difference being that all d quarks are replaced by s quarks. To calculate $\lambda_{D^+D^-}$ and $\lambda_{D_s^+D_s^-}$, the amplitude with the contributions shown in Fig. 2.5 is constructed

$$\begin{aligned} A(B_q^0 \to D_q^+D_q^-) = {} & V_{cq}V_{cb}^*(T + E + P^c + PA^c) \\ & + V_{uq}V_{ub}^*(P^u + PA^u) \\ & + V_{tq}V_{tb}^*(P^t + PA^t)\,, \end{aligned}$$

where $q \in \{d, s\}$, the strong amplitudes T, E, P^c, PA^c, P^u, PA^u, P^t and PA^t correspond to diagrams shown in Fig. 2.5 and the superscripted values denote the internal quark in the loop of the penguin diagrams. The strong amplitudes are separated from the CKM matrix elements originating from the weak quark-level transitions. This is convenient because the strong phases are separated from the weak phases that change sign under the *CP* transformation. Using Eq. (2.12) this can be simplified to

$$\begin{aligned} A(B_q^0 \to D_q^+D_q^-) = {} & V_{cq}V_{cb}^*(T + E + P^c + PA^c - P^t - PA^t) \\ & + V_{uq}V_{ub}^*(P^u + PA^u - P^t - PA^t)\,, \end{aligned} \tag{2.39}$$

and introducing

$$\mathcal{A} = T + E + P^c + PA^c - P^t - PA^t\,, \tag{2.40}$$

yields

$$A(B_q^0 \to D_q^+D_q^-) = V_{cq}V_{cb}^*\mathcal{A}\left[1 + \frac{V_{uq}V_{ub}^*}{V_{cq}V_{cb}^*}\frac{(P^u + PA^u - P^t - PA^t)}{\mathcal{A}}\right]. \tag{2.41}$$

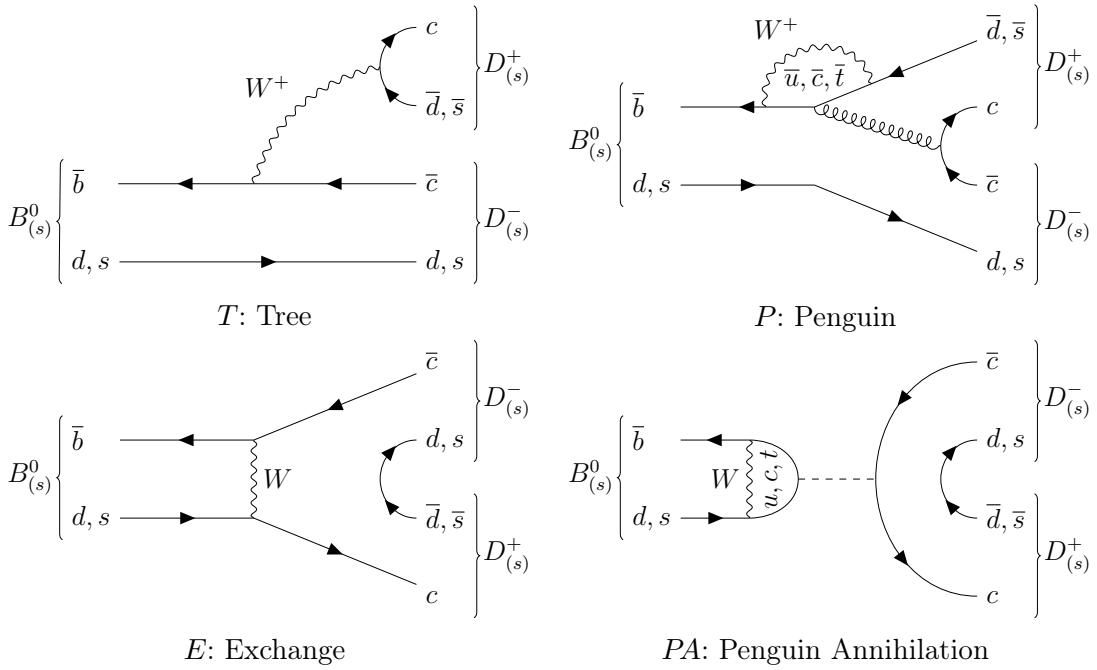

Figure 2.5: Dominant Feynman diagrams contributing to the decays $B^0 \to D^+D^-$ and $B_s^0 \to D_s^+D_s^-$. The (top left) tree-level, (bottom left) exchange, (top right) penguin and (bottom right) penguin annihilation diagrams are shown.

In $B^0 \to D^+D^-$ decays ($q = d$), the ratio of CKM elements can be rewritten using the definition of the angle γ from Eq. (2.13) and the side length R_b from Eq. (2.14). Using the following substitution

$$\frac{V_{ud}V_{ub}^*}{V_{cd}V_{cb}^*} = -\left|\frac{V_{ud}V_{ub}^*}{V_{cd}V_{cb}^*}\right| e^{i\gamma} = -R_b e^{i\gamma} \tag{2.42}$$

and absorbing the *CP*-conserving part in the hadronic parameters

$$ae^{i\theta} = R_b \left[\frac{P^u + PA^u - P^t - PA^t}{\mathcal{A}}\right] \tag{2.43}$$

the amplitude results in

$$A(B^0 \to D^+D^-) = V_{cd}V_{cb}^* \mathcal{A} \left[1 - ae^{i\theta}e^{i\gamma}\right] . \tag{2.44}$$

The *CP* conjugated amplitude is determined by flipping the sign of the weak phases and the ratio of amplitudes is given by

$$\frac{A(\overline{B}^0 \to D^+D^-)}{A(B^0 \to D^+D^-)} = \frac{V_{cd}^*V_{cb}}{V_{cd}V_{cb}^*} \frac{\left[1 - ae^{i\theta}e^{-i\gamma}\right]}{\left[1 - ae^{i\theta}e^{i\gamma}\right]} . \tag{2.45}$$

To calculate the parameter $\lambda_{D^+D^-}$ using Eq. (2.29) the ratio q/p is needed. In the B sector, this is dominated by the t quark [54] in the box diagrams shown in Fig. 2.4 and the ratio for B^0 mesons can be approximated by

$$\frac{q}{p} \approx \frac{V_{td}V_{tb}^*}{V_{td}^*V_{tb}} . \tag{2.46}$$

The parameter $\lambda_{D^+D^-}$ in the $B^0 \to D^+D^-$ system results in

$$\lambda_{D^+D^-} = \frac{q}{p}\frac{A(\overline{B}^0 \to D^+D^-)}{A(B^0 \to D^+D^-)} = \frac{V_{td}V_{tb}^*}{V_{td}^*V_{tb}}\frac{V_{cd}^*V_{cb}}{V_{cd}V_{cb}^*}\frac{\left[1 - ae^{i\theta}e^{-i\gamma}\right]}{\left[1 - ae^{i\theta}e^{i\gamma}\right]}\,. \tag{2.47}$$

In this expression, the definition of the angle β can be identified, yielding

$$\lambda_{D^+D^-} = e^{-i2\beta}\frac{1 - ae^{i\theta}e^{-i\gamma}}{1 - ae^{i\theta}e^{i\gamma}}\,. \tag{2.48}$$

Finally, the *CP* observables are calculated according to Eq. (2.31) and are given by

$$\begin{aligned} D_{D^+D^-} &= -\frac{\cos 2\beta - 2a\cos\theta\cos(2\beta+\gamma) + a^2\cos(2\beta+2\gamma)}{1 - 2a\cos\theta\cos\gamma + a^2}\,, \\ S_{D^+D^-} &= -\frac{\sin 2\beta - 2a\cos\theta\sin(2\beta+\gamma) + a^2\sin(2\beta+2\gamma)}{1 - 2a\cos\theta\cos\gamma + a^2}\,, \\ C_{D^+D^-} &= \frac{2a\sin\theta\sin\gamma}{1 - 2a\cos\theta\cos\gamma + a^2}\,. \end{aligned} \tag{2.49}$$

Due to $\Delta\Gamma_d \approx 0$, the parameter $D_{D^+D^-}$ is not observable because the corresponding term in Eq. (2.30) vanishes. However, the time-dependent asymmetry is still sensitive to the mixing phase $\phi_d = 2\beta$. In the case of negligible penguin pollution, the angle β could be measured according to $S_{D^+D^-} \approx -\sin 2\beta$ and $C_{D^+D^-} \approx 0$. Since this is not the case in $B^0 \to D^+D^-$ decays, the measured phase is referred to as an effective phase

$$\phi_{d,D^+D^-}^{\text{eff}} = \phi_d + \Delta\phi_{d,D^+D^-}\,. \tag{2.50}$$

This is a problem for measuring the angle β in this channel. However, the effective phase can be used to measure the phase shift $\Delta\phi_{d,D^+D^-}$ by using external clean β measurements from *e.g.* $B^0 \to J/\psi K_S^0$ decays [55]. As shown in the following the phase shifts in $B^0 \to D^+D^-$ and $B_s^0 \to D_s^+D_s^-$ decays are related and a measurement of $\Delta\phi_{d,D^+D^-}$ can be used to control the penguin pollution in the measurement of ϕ_s.

The phase shift is calculated using the relations

$$\begin{aligned} \sin\phi_{d,D^+D^-}^{\text{eff}} &= \sin(\phi_d + \Delta\phi_{d,D^+D^-}) = -\frac{S_{D^+D^-}}{\sqrt{1 - C_{D^+D^-}^2}}\,, \\ \cos\phi_{d,D^+D^-}^{\text{eff}} &= \cos(\phi_d + \Delta\phi_{d,D^+D^-}) = -\frac{D_{D^+D^-}}{\sqrt{1 - C_{D^+D^-}^2}}\,, \end{aligned} \tag{2.51}$$

to construct the ratio

$$\begin{aligned} \frac{\sin(\phi_d + \Delta\phi_{d,D^+D^-})}{\cos(\phi_d + \Delta\phi_{d,D^+D^-})} &= \frac{\sin\phi_d\cos\Delta\phi_{d,D^+D^-} + \cos\phi_d\sin\Delta\phi_{d,D^+D^-}}{\cos\phi_d\cos\Delta\phi_{d,D^+D^-} - \sin\phi_d\sin\Delta\phi_{d,D^+D^-}} \\ \Leftrightarrow \frac{S_{D^+D^-}}{D_{D^+D^-}} &= \frac{\sin\phi_d + \cos\phi_d\tan\Delta\phi_{d,D^+D^-}}{\cos\phi_d - \sin\phi_d\tan\Delta\phi_{d,D^+D^-}}\,. \end{aligned} \tag{2.52}$$

With the results from Eq. (2.49), the phase shift is given by

$$\begin{aligned}\tan\Delta\phi_{d,D^+D^-} &= \frac{S_{D^+D^-}\cos\phi_{d,D^+D^-} - D_{D^+D^-}\sin\phi_{d,D^+D^-}}{D_{D^+D^-}\cos\phi_{d,D^+D^-} + S_{D^+D^-}\sin\phi_{d,D^+D^-}} \\ &= \frac{a^2\sin 2\gamma - 2a\sin\gamma\cos\theta}{1 - 2a\cos\gamma\cos\theta + a^2\cos 2\gamma}\,.\end{aligned} \tag{2.53}$$

The *CP* observables in $B_s^0 \to D_s^+ D_s^-$ decays are derived similarly. Different CKM-matrix elements are involved in the decay, and the amplitude is given by

$$\begin{aligned}A(B_s^0 \to D_s^+ D_s^-) &= V_{cs}V_{cb}^*\mathcal{A}'\left[1 + \frac{V_{us}V_{ub}^*}{V_{cs}V_{cb}^*}\frac{(P^{u\prime} + PA^{u\prime} - P^{t\prime} - PA^{t\prime})}{\mathcal{A}'}\right] \\ &= V_{cs}V_{cb}^*\mathcal{A}'\left[1 + \frac{V_{us}V_{cd}}{V_{cs}V_{ud}}\frac{V_{ud}V_{ub}^*}{V_{cd}V_{cb}^*}\frac{(P^{u\prime} + PA^{u\prime} - P^{t\prime} - PA^{t\prime})}{\mathcal{A}'}\right] \\ &= V_{cs}V_{cb}^*\mathcal{A}'\left[1 - \frac{V_{us}V_{cd}}{V_{cs}V_{ud}}a' e^{i\theta'}e^{i\gamma}\right]\,.\end{aligned} \tag{2.54}$$

Due to the different quark transitions, the primed hadronic parameters of the $B_s^0 \to D_s^+ D_s^-$ decay are suppressed by the ratio of CKM elements

$$\epsilon = -\frac{V_{us}V_{cd}}{V_{cs}V_{ud}}\,. \tag{2.55}$$

As for B^0 mesons, the mixing of B_s^0 mesons is dominated by the t quark. The ratio q/p is approximated by

$$\frac{q}{p} \approx \frac{V_{ts}V_{tb}^*}{V_{ts}^*V_{tb}}\,, \tag{2.56}$$

and Eq. (2.29) is used to calculate the parameter

$$\begin{aligned}\lambda_{D_s^+D_s^-} &= \frac{q}{p}\frac{A(\overline{B}_s^0 \to D_s^+D_s^-)}{A(B_s^0 \to D_s^+D_s^-)} = \frac{V_{ts}V_{tb}^*}{V_{ts}^*V_{tb}}\frac{V_{cs}^*V_{cb}}{V_{cs}V_{cb}^*}\frac{\mathcal{A}'\left[1 + \epsilon a' e^{i\theta'}e^{-i\gamma}\right]}{\mathcal{A}'\left[1 + \epsilon a' e^{i\theta'}e^{i\gamma}\right]} \\ &= e^{i2\beta_s}\frac{1 + \epsilon a' e^{i\theta'}e^{-i\gamma}}{1 + \epsilon a' e^{i\theta'}e^{i\gamma}}\,.\end{aligned} \tag{2.57}$$

Finally, the *CP* observables in $B_s^0 \to D_s^+ D_s^-$ are given by

$$\begin{aligned}D_{D_s^+D_s^-} &= -\frac{\cos(-2\beta_s) + 2\epsilon a'\cos\theta'\cos(-2\beta_s + \gamma) + \epsilon^2 a'^2\cos(-2\beta_s + 2\gamma)}{1 + 2\epsilon a'\cos\theta'\cos\gamma + \epsilon a'^2}\,, \\ S_{D_s^+D_s^-} &= -\frac{\sin(-2\beta_s) + 2\epsilon a'\cos\theta'\sin(-2\beta_s + \gamma) + \epsilon^2 a'^2\sin(-2\beta_s + 2\gamma)}{1 + 2\epsilon a'\cos\theta'\cos\gamma + \epsilon a'^2}\,, \\ C_{D_s^+D_s^-} &= -\frac{2\epsilon a'\sin\theta'\sin\gamma}{1 + 2\epsilon a'\cos\theta'\cos\gamma + \epsilon^2 a'^2}\,.\end{aligned} \tag{2.58}$$

The phase shift is defined similarly to $\Delta\phi_{d,D^+D^-}$, but the angle β_s contributes with a minus sign to the effective phase, resulting in

$$\phi_{s,D_s^+D_s^-}^{\text{eff}} = \phi_s + \Delta\phi_{s,D_s^+D_s^-} = -2\beta_s + \Delta\phi_{s,D_s^+D_s^-}\,. \tag{2.59}$$

with the phase shift in $B_s^0 \to D_s^+D_s^-$ decays

$$\tan \Delta\phi_{s,D_s^+D_s^-} = \frac{\epsilon^2 a'^2 \sin 2\gamma + 2\epsilon a \sin\gamma \cos\theta'}{1 + 2\epsilon a' \cos\gamma \cos\theta' + \epsilon^2 a'^2 \cos 2\gamma} \,. \tag{2.60}$$

In the presence of New Physics contributions, Eq. (2.59) has to be extended to

$$\phi^{\text{eff}}_{s,D_s^+D_s^-} = \phi_s + \Delta\phi_{s,D_s^+D_s^-} + \phi_s^{\text{NP}} \,, \tag{2.61}$$

and it becomes apparent that $\Delta\phi_{s,D_s^+D_s^-}$ has to be determined to separate New Physics effects from higher-order SM contributions. In contrast to the $B^0 \to D^+D^-$ channel, the phase shift is suppressed by the small CKM ratio ϵ. In the limit of U-spin symmetry of the strong interaction, the hadronic parameters in the two decays are expected to be equal, *i.e.* $ae^{i\theta} = a'e^{i\theta'}$. The parameters a and θ can be determined precisely using the non-suppressed phase shift in $B^0 \to D^+D^-$ decays and the results can be used to control penguin pollution in $B_s^0 \to D_s^+D_s^-$ decays. Apart from the $B^0 \to D^+D^-$ channel many other $B \to D\overline{D}$ decay modes provide constraints on the hadronic parameters. Ultimately, a global analysis of a large set of *CP*-violation and branching-fraction measurements as presented in Ref. [23] enables searches for New Physics beyond the SM.

3 The LHCb experiment at the LHC

B mesons are unstable particles that, on average, decay within picoseconds. They can be found in nature, *e.g.* in interactions of cosmic rays with the earth's atmosphere. However, to precisely measure their properties and decay, a large sample of B mesons produced in a controlled environment is advantageous. These requirements are fulfilled at the Large Hadron Collider (LHC), the world's largest and most powerful particle accelerator to date, where B mesons are produced in proton-proton collisions. At one of the interaction points of the LHC, the LHCb detector is located. The data set used in the presented analyses was collected by the LHCb experiment during the years 2015–2018. This chapter provides an overview of the LHC and the LHCb detector, as well as the processing of the data.

In Sec. 3.1, the LHC and the complex of pre-accelerators are described based on Ref. [56]. The LHCb detector and its components are discussed in Sec. 3.2 using information from Refs. [57,58]. The tools and software used at LHCb to process the data are introduced in Sec. 3.3. A more specific tool for CP-violation measurements is the flavour tagging (FT) described in Sec. 3.4. It is essential for measurements of neutral B mesons as it enables the determination of the production flavour.

3.1 The Large Hadron Collider

The LHC is located near Geneva at the European Organisation for Nuclear Research (CERN) at the border between Switzerland and France. It is a circular collider with a circumference of 27 km, installed in a tunnel between 45 m and 170 m below the surface. Its main purpose is the acceleration of protons. However, the LHC is also regularly injected with heavy ions during dedicated runs. The operation with heavy ions is not relevant to this thesis and will not be discussed further.

The LHC is designed to collide protons at a centre-of-mass energy of up to 14 TeV with a luminosity of $10^{34}\,\mathrm{cm}^{-1}\,\mathrm{s}^{-1}$. In 2011, the LHC operated at a centre-of-mass energy of 7 TeV, and in 2012, the energy was increased to 8 TeV. This period is referred to as Run 1. In Run 2, which started in 2015 and lasted until 2018, the LHC operated at a centre-of-mass energy of 13 TeV. To reach these high energies, the protons are pre-accelerated in several stages before they are injected into the LHC. This is accomplished by the accelerator complex shown in Fig. 3.1. The protons are produced from a bottle of hydrogen gas by removing the electrons from the hydrogen atoms using an electric field. They are divided into bunches of about 10^{11}

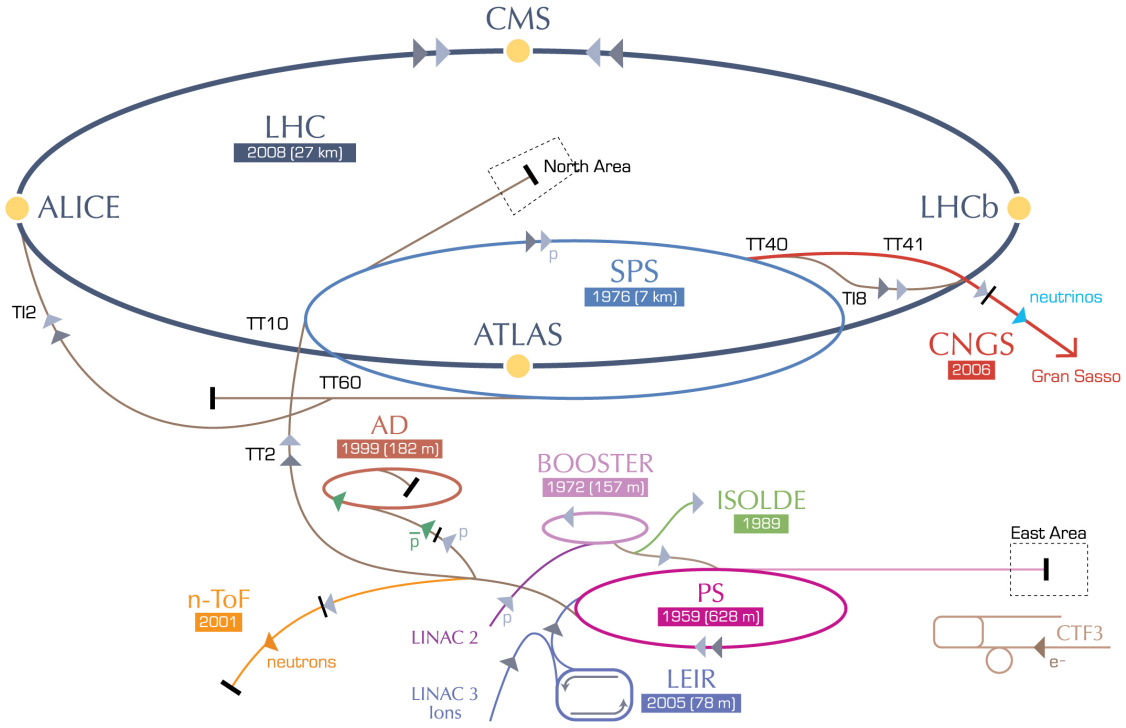

Figure 3.1: Layout of the CERN accelerator complex [59].

protons and are accelerated by a linear accelerator, the LINAC 2. Afterwards, the protons pass through several circular accelerators, starting with the BOOSTER, followed by the Proton Synchrotron (PS). Finally, the protons are accelerated in the Super Proton Synchrotron (SPS) to reach energies of 450 GeV/c^2. The protons are injected into the LHC in two beams that circulate in opposite directions.

The LHC has 16 radio frequency cavities to accelerate the protons to their final energy of up to 7 TeV per beam. When the final energy is reached, these cavities need to account for the energy loss due to synchrotron radiation. The protons are kept on their circular path by 1232 dipole magnets, and the beams are focused using quadrupole magnets. To reach a magnetic field strength of up to 8 T, the LHC uses superconducting magnets, which have to be cooled to 1.9 K. The two beams are brought to collision at four interaction points, where the detectors of the experiments ALICE [60], ATLAS [61], CMS [62] and LHCb [58] are located.

3.2 The LHCb detector

The LHCb detector is designed to study the decays of particles containing b and c quarks. At the LHC, the heavy quarks are dominantly produced with large boosts in the forward and backward directions. Thus, the LHCb detector, illustrated in Fig. 3.2, is a single-arm forward spectrometer covering an angular range from 10

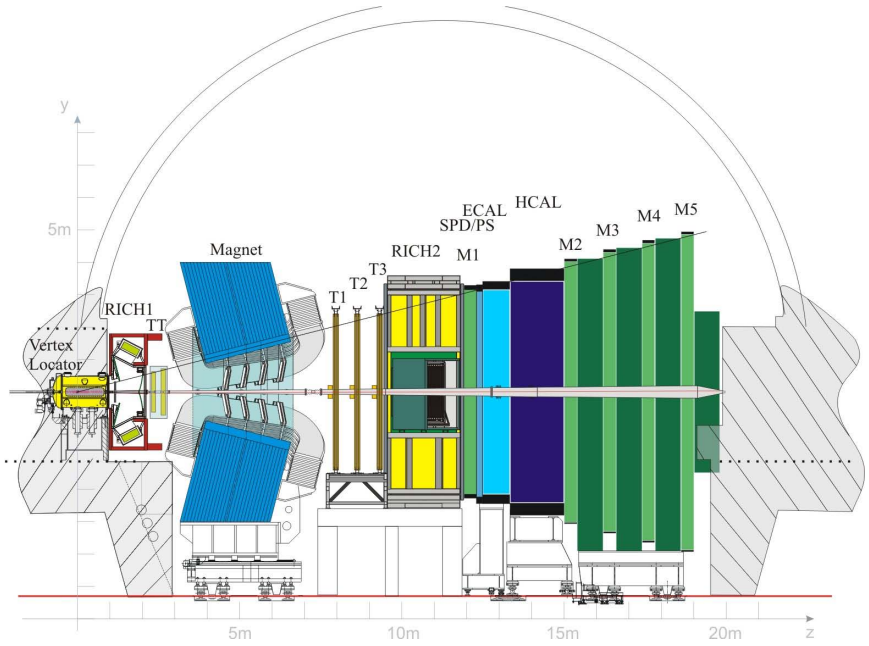

Figure 3.2: Schematic view of the LHCb-detector layout [58].

to 300 (250) mrad in the vertical (horizontal) plane. In contrast to the other large experiments at the LHC, the instantaneous luminosity at LHCb is intentionally reduced. This is achieved by adjusting the transversal beam overlap [63]. During the LHC run, the overlap is increased to account for beam losses and keep the instantaneous luminosity stable. With roughly one proton-proton interaction per bunch crossing, the occupancy in the LHCb detector is much lower than in the other detectors at the LHC. However, this improves data quality, which is essential for LHCb physics programme, and reduces radiation damage.

To further prevent the sensitive parts of the detector near the beam pipe from radiation damage due to unstable beam conditions, the Beam Conditions Monitor system is installed [64]. It monitors the particle flux around the beam pipe at two locations, and if the flux exceeds certain thresholds, a beam dump is triggered. Each station consists of eight radiation-hard diamond sensors placed around the beam pipe.

Since B mesons only travel a few centimetres before they decay, they are not directly detected. They can only be reconstructed through the interaction of their decay products with the detector material. Particles that leave clear signatures in the detector are charged and neutral pions, charged kaons, protons, antiprotons, muons, electrons and photons. The average lifetime of these particles is sufficiently long to traverse the detector. The components of the LHCb detector are designed to measure their properties. They can be divided into tracking and particle identification (PID) components, which are described in the following.

3.2.1 Tracking system

The tracking system of the LHCb detector is composed of the Vertex Locator (VELO), the Tracker Turicensis (TT), the T1–T3 tracking stations and a dipole magnet. Tracks are reconstructed by measuring the position of charged particles at different points along their trajectories. Charged particles interact with the detector material, thereby depositing energy that is converted into an electric signal. The detector material is segmented in order to determine the position associated with these so-called hits. From the spatial information of the hits, algorithms can reconstruct the trajectories.

Vertex Locator

The VELO [65] is the innermost part of the LHCb detector. It provides precise tracking information close to the primary vertex (PV), which is the position of the initial pp interaction. The PV and decay vertices can be measured with high precision. This is essential for time-dependent measurements because the decay time of a B meson is computed from the distance between its decay vertex and the PV. A decay-time resolution of less than 50 fs is achieved. The VELO consists of silicon modules with R and ϕ sensors measuring the hit position in polar coordinates. Each module is a half-disc, and the two halves of the detector can be moved to increase the distance from the beam. This is necessary to protect the modules from radiation damage during unstable beam conditions, *e.g.* the injection of the protons into the LHC. During physics data taking, the VELO halves are located at a distance of 7 mm from the beam.

Tracking stations

The tracking stations, the TT and T1–T3, are placed downstream of the VELO. The tracking stations T1–T3 are divided into an inner and an outer part. The inner part and the TT use silicon strip sensors. Electron-hole pairs are produced by charged particles passing through the sensor, inducing a current pulse. The outer modules are made of drift tubes filled with a mixture of Argon, CO_2 and O_2 [66]. Charged particles ionise the gas, and the electrons drift to the anode wire in the middle of the tube, inducing a signal. Each of the modules consists of four layers. The first and last layers are vertically aligned, while the inner two layers are tilted by $\pm 5°$, which enables two-dimensional measurements of the hit positions in each module.

Dipole magnet

A dipole magnet is placed between the TT and the T1–T3 stations to bend the trajectories of charged particles. The momentum and charge of the particles can be determined from the measurement of the tracks downstream and upstream of

the magnet. A conventional dipole magnet with an integrated magnetic field of 4 Tm is used. Occasionally, the magnet polarity is switched to study detection asymmetries.

3.2.2 Particle identification system

In measurements using hadronic final states, it is essential to distinguish between charged pions, kaons and protons. These particles are commonly used to reconstruct decays of beauty hadrons. The chaotic environment of a hadron collider produces many charged hadrons, especially pions, and often unrelated particles are combined to reconstruct a beauty-meson candidate. This leads to a high contribution of combinatorial background. To differentiate between combinatorial background and beauty hadrons, the invariant mass of the B candidates has to be calculated correctly. Thus, PID is essential to assign the correct masses to the final-state particles. Ultimately, this also makes it possible to distinguish between signal decays and backgrounds caused by other decays.

Ring Imaging Cherenkov detectors

At LHCb, two Ring Imaging Cherenkov (RICH) detectors are used to mainly distinguish between charged pions, kaons and protons. These detectors make use of the Cherenkov effect to assign particle hypotheses. They consist of gas radiators, producing a Cherenkov radiation cone when a charged particle travels through the medium faster than light. The emission angle depends on the velocity of the particle and the refractive index of the medium. A system of mirrors is used to focus the radiation into ring images and guide it out of the detector acceptance, where it is detected with hybrid photodetectors. The radius of the ring image is proportional to the Cherenkov angle and, thus, the velocity of the particle. In combination with the momentum measurements, the masses of charged particles can be inferred.

RICH1 is placed between the VELO and the TT covering a momentum range of 2–40 GeV/c and an angular acceptance of 25–300 mrad. It uses C_4F_{10} gas radiators to produce the Cherenkov radiation. Since the refractive index of C_4F_{10} is not sufficient to distinguish between low momentum kaons and protons, a second aerogel radiator is placed at the entrance [67].

RICH2 is placed downstream of T1–T3 and covers a momentum range of 15–100 GeV/c and an angular acceptance of 15–120 mrad. The smaller angular coverage is chosen because particles with high momentum are usually produced with smaller angles with respect to the beam pipe. The higher momentum range is achieved using a CF_4 gas radiator.

Calorimeter system

The calorimeter system of LHCb serves several purposes. It provides additional spatial information and measures the energy of particles. The layout of the calorimeter system makes it possible to distinguish between neutral pions, photons, electrons and hadrons. The two main components are the electromagnetic calorimeter (ECAL) and the hadronic calorimeter (HCAL). They are built using a similar sampling calorimeter layout with layers of a dense material inducing particle showers and scintillator material, which absorbs the energy of incoming particles and emits it as light. The light is transmitted to photo multipliers by wavelength-shifting fibres. The energy of the incoming particle can be deduced from the measured photon yield. The ECAL is made of scintillator tiles and layers of lead. It measures the energy of electrons and photons, which induce an electromagnetic shower in the material. To ensure that the electromagnetic shower does not reach the HCAL, the ECAL is 25 radiation lengths thick to contain the whole electromagnetic shower. A preshower detector is placed upstream of the ECAL to separate electromagnetic and hadronic showers. Since photons and neutral pions have a similar signature in the ECAL, a scintillating pad detector (SPD) is placed in front of the preshower detector. Neutral particles are not detected in the SPD, but a thin lead converter is placed in between, causing a signal in the preshower detector and the ECAL. The HCAL is composed of scintillator tiles and iron plates and is 5.6 interaction lengths thick. In contrast to purely electromagnetic showers, a shower induced by charged hadrons mainly deposits energy in the HCAL.

Muon chambers

Finally, the LHCb detector has one muon chamber upstream and four downstream of the calorimeter system. The muon chambers [68] are made of multi-wire proportional chambers able to measure the tracks of charged particles. Since the muons are the only particles that can still be detected after the calorimeters, they can be reliably identified. Iron absorber layers are placed between the muon chambers to select penetrating muons.

3.3 Data processing at LHCb

The processing of the Run 2 data at LHCb is structured as shown in Fig. 3.3. At the first stage, the events are filtered through a trigger system explained in Sec. 3.3.1. Events that pass the trigger selection are fully reconstructed by the algorithms outlined in Sec. 3.3.2. Before the data can be used for offline analysis, an online preselection, called Stripping, is applied as described in Sec. 3.3.3. Finally, the production of simulated data at LHCb, which is used for dedicated studies and cross-checks, is explained in Sec. 3.3.4. The applications built for the individual processing steps are based on the Gaudi framework [70].

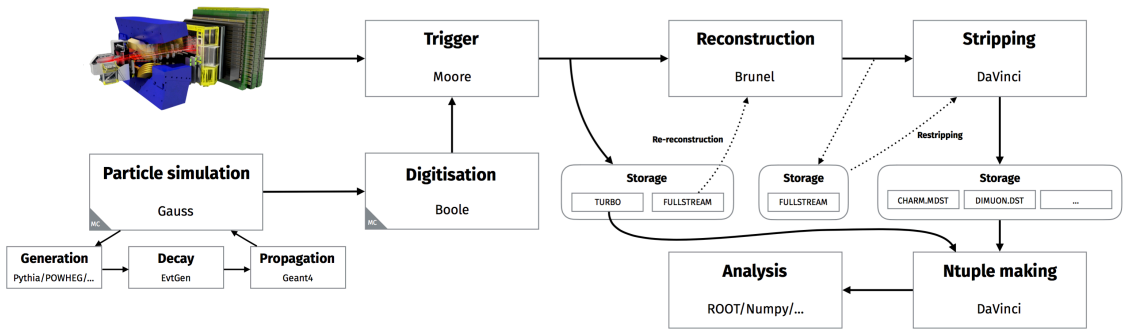

Figure 3.3: Schematic view of the data flow at the LHCb experiment [69].

3.3.1 Trigger

Most of the data produced at the LHCb detector cannot be stored due to storage and bandwidth limitations. The trigger system is designed to reduce the input rate by applying selections to retain events that are most likely relevant for physics analyses. In Run 2, the trigger system was composed of three stages: the Level-0 (L0) trigger and the two high-level triggers, HLT1 and HLT2. The L0 trigger is implemented in hardware, while the HLT is software-based and run by the MOORE application [71].

Hardware trigger

The L0 trigger is the first stage, and it is designed to reduce the 40 MHz proton-proton collision rate to the 1 MHz readout limit of the detector. Since B mesons are heavy, their final-state particles usually have high transverse momentum, p_{T}, or energy, E_{T}. In the case of muons, this can be used by the L0 muon trigger, which reconstructs tracks in the muon chambers and selects the two highest p_{T} muons in each quadrant of the detector. The L0 calorimeter trigger, on the other hand, reconstructs E_{T} deposits in the calorimeters. In combination with the SPD and preshower information, a first particle hypothesis is assigned to distinguish between neutral pions, photons, electrons and hadrons. The highest E_{T} particle of each type is selected. The VELO is equipped with a pile-up system to estimate the number of primary proton-proton interactions in each bunch crossing. These events are rejected because they have a high detector occupancy, making them difficult to reconstruct and less suitable for analysis. The final L0 trigger decision is made by combining the information of these three systems.

Software trigger

Events that pass the L0 trigger are processed by HLT1. This software-based trigger runs on the LHCb event filter farm, a high-capacity computing cluster at CERN. The main goal is to confirm the L0 trigger decisions by individually reconstructing tracks in the VELO and the other tracking stations corresponding to the particles

reconstructed at L0 level. Requirements on the p_{T} and the impact parameter (IP) with respect to the PV, which is the distance between a track and the PV, are applied. To improve discrimination between B decays and background, additional particles may be reconstructed. The events that pass HLT1 are stored on local hard drives of the event filter farm.

These events are further processed by HLT2, which is the second level of the software trigger running on the remaining resources of the event filter farm. HLT2 is structured in different selection algorithms denoted as trigger lines, which apply inclusive and exclusive selections based on fully reconstructed events. The topological lines relevant to this analysis apply inclusive selections using multivariate algorithms. The decisions are based on displaced vertices reconstructed from two, three or four tracks and kinematic properties. Additional lines are used, which select ϕ decays that are likely to originate from B decays.

3.3.2 Reconstruction

Events that pass the trigger selections are fully reconstructed using the Brunel application [72]. First, individual track segments are reconstructed independently in the VELO and the tracking stations. These so-called track seeds are constructed from a fit to the hits in each station. They have to fulfil certain requirements, such as a minimum number of hits to be considered for reconstruction. The track seeds are matched by linear extrapolation into the magnet area. The track segments that belong to each other are refitted using a Kalman filter [73], which accounts for multiple scattering and energy loss. Each measurement is added recursively to the fit until the entire particle trajectory is reconstructed.

In the next step, the tracks are combined with information from the PID detectors. The expected hit pattern from a track under different particle hypotheses is compared to the observed pattern in the RICH detectors. This algorithm provides the best hypothesis for each track and the decrease in the likelihood when changing to different particle hypotheses. The tracks are further extrapolated and matched with observed clusters in the calorimeter system. Photons can be detected by a cluster in the ECAL and the absence of an associated track. The π^0 mesons can be reconstructed from two separate photon clusters in the ECAL. However, if the two clusters cannot be resolved, SPD information is used to distinguish between photons and π^0 mesons. Finally, the extrapolated particle trajectories are matched with hits in the muon chambers. The particles are considered muons if a minimum number of hits in the muon chambers can be assigned to their trajectory. The minimum number of hits depends on the transverse momentum of the particle. Information from the RICH detectors, the calorimeter system and the muon stations are combined for particle identification. The final output of the reconstruction software is stored as so-called proto particles. A proto particle contains all reconstruction information

of a single particle. The reconstructed events are then written to tape and stored long-term.

3.3.3 Stripping

The reconstructed data contain various decay modes, most of which are irrelevant to the specific analyses. Therefore, a final online preselection is performed before the data are available for individual offline analyses. The preselection is referred to as stripping and is implemented in the DaVinci framework [74]. It is structured in stripping lines each designed to select a specific decay topology. Proto particles are combined to reconstruct intermediate states and, ultimately, the head of the decay chain. The combination is performed by the OfflineVertexFitter, which fits the vertices of the intermediate states using the tracks of the proto particles. Their momentum components and energy are calculated, and the procedure is repeated until the head of the decay chain is reached. The properties of the reconstructed vertices and particles are used to impose loose selection requirements and further reduce the amount of data. Finally, the output of each stripping line, which contains a set of decay modes with similar topologies, is available for offline analysis. Due to the loose selection requirements and the similar topologies, the $B^0 \to D^+D^-$ and $B_s^0 \to D_s^+D_s^-$ decays relevant for this thesis are contained in the same stripping line.

Most observables used throughout the offline analysis are calculated by the DecayTreeFitter (DTF) [75]. In contrast to the OfflineVertexFitter, the DTF performs a fit to the whole decay chain using a Kalman filter. This can be used to improve the resolution by applying constraints to the decay chain. The invariant masses and momenta are computed by a fit, in which the masses of intermediate particles are constrained to their known value. In order to avoid a correlation between the decay time and invariant mass, these constraints are not applied in the computation of the decay-time-related observables. In this case, however, the head of the decay chain is required to originate from the PV.

3.3.4 Simulation

Analysis techniques are developed and validated using simulated data. In the presented analysis, simulated samples are used to train multivariate algorithms, calculate efficiencies and study parameterisations of mass and decay-time distributions.

At LHCb, the simulated samples are generated using the Gauss application [76]. The initial proton-proton interaction is generated by Pythia [77] with a specific LHCb configuration. Decays of unstable particles are implemented in EvtGen [78], and the photon radiation of final-state particles is generated by Photos [79]. The Geant4 toolkit [80] is used to model the whole detector and its interaction with

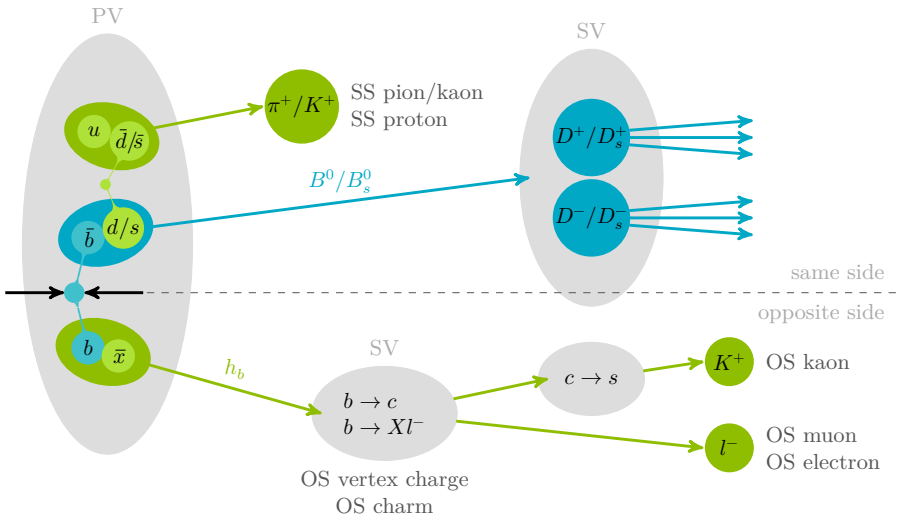

Figure 3.4: Schematic view of a B-meson production in proton-proton collisions adapted from [84]. The tagging particles and the taggers are explained in the text.

the generated particles. Finally, the detector response and digitisation of the data is simulated using Boole [81]. At this stage, the simulated data has the same format as the recorded raw data and is passed through the same processing chain. To save resources, the samples used in this analysis are generated by reusing the underlying proton-proton collision multiple times and only the signal decays are generated independently for each event [82].

These tools combine the current knowledge of particle physics to generate simulated data that is as close to the real signal as possible. However, several aspects are not properly described by the simulation. This applies to the PID variables, which are known to be different in simulation and recorded signal data. The PID variables used in the presented analyses are corrected using the PIDCalib package [83].

3.4 Flavour tagging at LHCb

To measure CP violation in decays of neutral B mesons, it is essential to know if a candidate was produced as a B meson or a $\overline{B}$ meson. At LHCb, a set of FT algorithms, referred to as taggers, determine the production flavour of the B mesons. Each tagger assigns a tagging decision that represents the production flavour based on the charges of particles associated with the B-meson production. The basic concept of the taggers is illustrated in Fig. 3.4. The production of a (blue) signal B meson in a proton-proton collision is accompanied by (green) secondary charged tagging particles whose charges are correlated with the production flavour of the signal. The taggers are divided into two categories, the opposite-side (OS) and the same-side (SS) taggers, which are explained in the following.

Opposite-side taggers

Beauty quarks at LHCb are dominantly produced in $b\bar{b}$ pairs. If one of the b quarks hadronises to a meson, which proceeds to decay as signal, the other quark, referred to as OS b quark, has the opposite flavour and can be used to assign a tag. The OS taggers [85] select particles that are likely to originate from the decay of the OS b quark. The single-particle taggers determine the production flavour based on the charge of a single tagging particle. This includes the OS electron and muon taggers, which select leptons produced in semi-leptonic decays of the OS b quark, and the OS kaon tagger, which selects charged kaons from $b \to c \to s$ transitions. The OS vertex charge tagger uses a more inclusive approach. Potential secondary vertices from particles produced in the same proton-proton interaction as the signal b quark are reconstructed. Kinematic and geometric properties are used to choose the candidate that is most likely originating from the OS b decay. A charge prediction is assigned by computing the sum of the charges of the tracks associated with this vertex, weighted by their transverse momenta. The production flavour is inferred from this prediction. The OS charm tagger [86] reconstructs charm-hadron decays originating from $b \to c$ transitions. The charge and, thus, the production flavour is determined by the charges of the decay products.

Same-side taggers

The SS taggers select particles produced in the hadronisation of the signal b quark. As shown in Fig. 3.4, a charged pion can be produced from the hadronisation. Pions are selected by the SS pion tagger [87] and the tag can be inferred from the pion charge because of correlated quark flavours. Alternatively, a proton can hadronise instead of a pion, which is selected by the SS proton tagger. In the case of B_s^0 mesons, a strange quark takes the place of the down quark, which means a charged kaon can be produced. These kaons are selected by the SS kaon tagger.

3.4.1 Flavour-tagging implementation and performance

Flavour tagging in hadronic environments such as the LHC is a challenging endeavour. Several factors can reduce the performance of a tagger. Neutral mesons produced in the OS decay chain can oscillate before they decay, which leads to the wrong tag. Moreover, the taggers may not be able to reconstruct a tagging particle, or the reconstructed particle may not be associated with the signal b quark. These factors must be quantified and taken into account in the analysis.

A tagger assigns each candidate a decision, referred to as a tag, d, and an estimate of this decision being wrong, the predicted mistag, η. The tag takes the values $d = 1$ for a B meson at production, $d = -1$ for a $\overline{B}$ meson at production and $d = 0$ if no decision can be made. The predicted mistag is a continuous variable ranging from 0 to 0.5. A predicted mistag of $\eta = 0$ represents a perfect tag decision, while

a predicted mistag of $\eta = 0.5$ is equivalent to a random decision and corresponds to a tag of $d = 0$. The predicted mistag is calculated by a multivariate classifier, usually a boosted decision tree (BDT) (see Sec. 4.1). The classifier is trained on samples of flavour-specific decays, *i.e.* decays where the flavour at the time of the decay can be determined from the charges of the final-state particles. Either self-tagging $B^{\pm}$ decays, for which the decay flavour is equal to the production flavour, or flavour-specific neutral B decays are used to train the taggers. When neutral B mesons are involved, their oscillation has to be taken into account.

The tagging efficiency, ε_{tag}, accounts for the fact that not all candidates can be tagged. The mistag rate introduces another dilution factor of $1 - 2\omega_i$, where ω_i is the true mistag probability of the candidate i (details on ω_i are given in Sec. 3.4.2). To assess the performance of a tagger on a sample of N candidates, the tagging power

$$\varepsilon_{\text{eff}} = \frac{1}{N}\sum_i (1 - 2\omega_i)^2 \tag{3.1}$$

is defined, where the sum iterates over all candidates. The tagging power represents the loss of statistical power due to the imperfect tagging *i.e.* the *CP* observables could be measured with the same statistical uncertainty on a perfectly tagged sample of $\varepsilon_{\text{eff}} \cdot N$ candidates.

3.4.2 Flavour-tagging calibration and combination

The training of the taggers relies on the kinematic properties of the tagged candidate and the other particles in the event. These are usually different for training samples and the data set used in the analysis. Therefore, the taggers have to be calibrated to represent the mistag probability, $\omega(\eta)$, of the signal decay. Flavour-specific control channels can be used to measure the actual mistag rate and compare it to the predicted mistag. A calibration function is optimised, which measures the dependence of the predicted mistag on the actual mistag. The control channels have to be kinematically similar to the signal channel to ensure that the calibration is valid for the signal sample. A linear calibration function of the form

$$\omega(\eta) = p_0 + p_1(\eta - \langle\eta\rangle) \tag{3.2}$$

is usually sufficient to describe the dependence of the measured mistag on the predicted mistag. The average predicted mistag, $\langle\eta\rangle$, is subtracted to reduce the correlation between the calibration parameters p_0 and p_1. The predicted and measured mistag are equal if $p_0 = \langle\eta\rangle$ and $p_1 = 1$. To account for differences in the calibration of B and $\overline{B}$ mesons, two calibration functions are used and the mean and difference of the calibration parameters

$$p_{0,1} = \frac{p_{0,1}^{B} + p_{0,1}^{\overline{B}}}{2} \quad \text{and} \quad \Delta p_{0,1} = p_{0,1}^{B} - p_{0,1}^{\overline{B}} \tag{3.3}$$

are reported.

To utilise the full potential of the FT, the individual taggers are combined to provide a single tag decision and mistag. Assuming that the calibrated mistags can be treated as probabilities, the combined probabilities for initial B and $\overline{B}$ mesons are given by

$$P(B) = \frac{p(B)}{p(B) + p(\overline{B})} \text{ and } P(\overline{B}) = 1 - P(B)\,. \tag{3.4}$$

The probabilities $p(B)$ and $p(\overline{B})$ are computed according to

$$p(B) = \prod_i \frac{1 - d^i}{2} + d(1 - \omega^i)\,, \tag{3.5}$$

$$p(\overline{B}) = \prod_i \frac{1 + d^i}{2} - d(1 - \omega^i)\,, \tag{3.6}$$

where the product iterates over the individual taggers. The combined tag decision and mistag are assigned as follows:

$$(d, \omega) = \begin{cases} (\ \ 1, P(\overline{B})) & \text{,if } P(B) > P(\overline{B}) \\ (-1, P(B)) & \text{,if } P(B) < P(\overline{B}) \\ (\ \ 0, 0.5) & \text{,if } P(B) = P(\overline{B}) \end{cases}. \tag{3.7}$$

The combined mistag has to be calibrated again to account for non-linearities in the combination. In this analysis, the FT calibration and combination is performed using the EspressoPerformanceMonitor (EPM) [88].

4 Methods

In high-energy physics, measurements are often highly complex, and various statistical methods are required to extract relevant information from the data. This chapter briefly introduces some of these methods relevant to the analyses presented in this thesis. In Sec. 4.1, BDTs are explained, which are used to classify events from different origins. The maximum likelihood method, described in Sec. 4.2, is used for parameter estimation by fitting data to a given model. Additionally, these fits serve to unfold data distributions from different sources as described in Sec. 4.3. The bootstrap method explained in Sec. 4.4 is used to verify the uncertainties of fit parameters. Finally, in Sec. 4.5, Wilks' theorem is presented, which is used to determine the significance of a measurement.

4.1 Boosted decision trees

A common task in high-energy physics is classifying events from different sources, *e.g.* signal and background. In rare cases, this can be achieved using simple cut-based requirements on variables with good separation power. However, this is usually inefficient and more sophisticated methods are required. Multivariate classifiers, such as decision trees, classify events by evaluating a sequence of decision rules based on multiple input features.

Figure 4.1 shows a schematic example of a decision tree. At the root node, a cut-based requirement on one feature from the set is applied to split the data sample. This is repeated at each internal node of the tree with different features and thresholds until a leaf node is reached. This happens when certain criteria are met, *e.g.* the maximum depth of the tree is reached, the purity of the node is high enough or too few events are left in the node. These criteria are decision-tree hyperparameters that can be adjusted to optimise the model's performance. A final classification decision is assigned to the events at each leaf node. The feature and threshold at each node are chosen to maximise a performance metric. They are determined during the training of the decision tree using a sample of labelled training data.

A single decision tree is a weak learner because it provides only limited separation power for a complex classification task. In a BDT, decision trees are iteratively added to the model to improve the classification performance. Each decision tree is weighted, which is referred to as boosting [89, 90]. A loss function is used to assess the performance of the model in each training iteration. The loss function

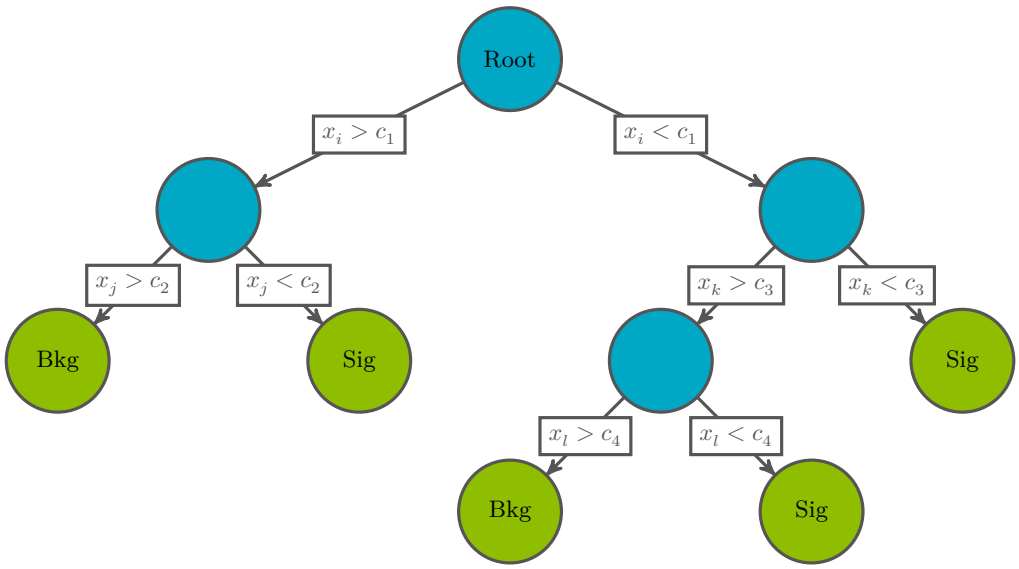

Figure 4.1: Schematic view of a single decision tree. The variables $\vec{x}$ are used to distinguish between the two classes (Sig) signal and (Bkg) background.

compares the prediction of the model, $\hat{y}_i$, with the true labels of the training data, y_i. For classification problems, $y_i \in \{0, 1\}$, with gradient boosting [91] the logistic loss function

$$L(y, \hat{y}) = -\sum_i y_i \log \hat{y}_i + (1 - y_i) \log (1 - \hat{y}_i) \,, \tag{4.1}$$

is used, where i iterates over all events of the training sample. In each training step, the new decision tree is trained on the residuals of the previous model's prediction with respect to the true labels. Thus, the new decision tree is trained to correct the mistakes of the previous model. A learning rate is used to modify the contribution of each new decision tree to the model.

Boosted decision trees can be prone to overfitting, which means they are sensitive to statistical fluctuations in the data and thus may have a good performance on the training data but perform poorly on unseen data. The training data is usually split into training and validation samples to prevent overfitting. In each iteration, the model performance is computed on the validation sample. The training is stopped when the performance does not increase over a certain number of iterations. The number of iterations required to stop the training is a tunable hyperparameter. In addition, the k-fold cross-validation method [92] can be used, where the training data is split into k equally sized samples. A BDT is trained on $k - 1$ samples and applied to the remaining events. The procedure is repeated until the model has been applied to the entire data set. This allows the entire data set to be used for further analysis and reduces the risk of overfitting. The BDTs presented in this thesis are trained with the XGBoost package [93].

4.2 Maximum likelihood method

The (unbinned) maximum likelihood method is commonly used to estimate the parameters of a model given a set of observations. Assuming that the observed data, $\vec{x} = \{\vec{x}_1, \vec{x}_2, \ldots, \vec{x}_n\}$, follows a certain probability density function (PDF), $\mathcal{P}(\vec{x}\,|\,\vec{\theta})$, the maximum likelihood method can be used to find a set of parameters, $\vec{\theta}$, that maximises the likelihood of observing the data. This set is found by maximising the likelihood function

$$\mathcal{L}(\vec{\theta}|\vec{x}) = \prod_{i=1}^{n} \mathcal{P}(\vec{x}_i\,|\,\vec{\theta})\,. \tag{4.2}$$

To account for n itself being a random variable following the Poisson distribution with the expected number of observations, N, the likelihood function can be extended as explained in Ref. [94] to

$$\mathcal{L}(\vec{\theta}|\vec{x}) = \frac{e^{-N}N^n}{n!} \prod_{i=1}^{n} \mathcal{P}(\vec{x}_i\,|\,\vec{\theta})\,. \tag{4.3}$$

This is particularly useful when the PDF is a sum of multiple contributions, c, each with its own set of parameters, $\vec{\theta}_c$, and the number of observations N_c. The PDF can be written according to

$$\mathcal{P}(\vec{x}\,|\,\vec{\theta}) = \sum_c N_c\,\mathcal{P}_c(\vec{x}\,|\,\vec{\theta}_c)\,. \tag{4.4}$$

In this case, the extended maximum likelihood method provides an accurate estimate of N_c and its uncertainty. Usually, the negative logarithm of the likelihood function is minimised, which is equivalent to maximising the likelihood function. The logarithm makes the procedure numerically more stable while changing the sign exploits the fact that most optimisation algorithms are designed to minimise functions.

If the PDF depends on an input parameter, θ_i, with a central value, μ_i, and an uncertainty, σ_i, the likelihood can be modified to take this uncertainty into account. This is referred to as Gaussian constraint and is implemented by multiplying the likelihood function with a Gaussian function of the form

$$\mathcal{G}(\theta_i|\mu_i,\sigma_i) = \frac{1}{\sigma_i\sqrt{2\pi}} e^{-(\theta_i-\mu_i)^2/2\sigma_i^2}\,. \tag{4.5}$$

In the presented analyses, the fits are performed within the ROOT framework [95] using the minimisation algorithms of the MINUIT package [96].

4.3 Unfolding data distributions

The *sPlot* technique [97] is a tool to unfold the distribution of a target variable that contains contributions from different sources. Given a data sample that is a mixture of n_s different sources of events, the *sPlot* technique allows to reconstruct the

distribution of the target variable for each source separately by assigning weights to each event. A set of discriminating variables, y, is used to determine these weights. The discriminating variables have to be uncorrelated with the target variable. The weight of the event, e, to unfold the component, c is calculated using the formula

$$ {}_s\mathcal{P}_c(y_e) = \frac{\sum_{j=1}^{n_s} V_{cj}\, \mathcal{P}_j(y_e)}{\sum_{k=1}^{n_s} N_k \mathcal{P}_k(y_e)}\,, \tag{4.6} $$

where the yields, N_k, and the parameters of the PDFs are determined by an extended maximum likelihood fit to the distributions of the discriminating variables. The covariance matrix of the yields, V_{cj}, is determined by a second fit, where only the yields are free to vary. These weights are normalised such that the sum of the weights for each source is equal to the observed number of events N_c.

Maximum likelihood fits to weighted target distributions are known to underestimate the uncertainty of the fit parameters. As described in Ref. [98], modifications to the likelihood can be used to obtain the correct uncertainties. However, this approach can be computationally expensive and a simpler approach is used in the presented analyses. The weights are scaled by the factor

$$ \frac{\sum_e {}_s\mathcal{P}_c(y_e)}{\sum_e {}_s\mathcal{P}_c(y_e)^2}\,. \tag{4.7} $$

Since this scaling does not generally provide the correct uncertainty, the uncertainties of the fit parameters are validated using the bootstrap method described in the following.

4.4 Bootstrap method

The bootstrap method [99] is a model-independent resampling technique which can be used to estimate the variance of fit parameters. Bootstrap samples are generated by drawing n events with replacement from the original data sample. The total number, n, is drawn from a Poisson distribution whose expectation value corresponds to the number of events in the original data sample. This preserves correlations between the observables. Parameters of interest are determined as for the original data sample by performing maximum likelihood fits to the bootstrap samples. The residual distributions are obtained, which is the difference between the fit results of the bootstrap samples and the fit results of the original data sample. The uncertainties of the fit parameters are estimated by the standard deviations of the residual distributions. The number of bootstrap samples is chosen so that statistical fluctuations do not significantly affect the estimated uncertainties.

4.5 Wilks' theorem

Wilks' theorem [100] is used to determine the significance of a measurement by comparing the result against a null hypothesis. The relevant parameters for this thesis are determined by a maximum likelihood fit. The negative log-likelihood value of this fit is denoted as $\mathrm{NLL}_{\mathrm{baseline}}$. To obtain the significance of the result, a second maximum likelihood fit is performed with the parameters of interest fixed to certain values that correspond to the null hypothesis. This fit provides the negative log-likelihood value NLL_0. Using Wilks' theorem, the likelihood ratio of the baseline fit with respect to the fit under the null hypothesis is used to calculate a χ^2 value according to

$$\chi^2 = -2 \ln \frac{\mathcal{L}_0}{\mathcal{L}_{\mathrm{baseline}}} = 2 \left[\mathrm{NLL}_0 - \mathrm{NLL}_{\mathrm{baseline}} \right]. \tag{4.8}$$

The χ^2 value can be converted to a p-value using the χ^2 distribution, where the number of degrees of freedom corresponds to the difference in the number of free parameters of the two fits. Since, in particle physics, the significance is usually presented in terms of standard deviations, the p-value is converted to a significance using the inverse of the cumulative distribution function of the standard normal distribution.

5 Analysis strategy

This chapter outlines the analysis strategy for the measurements of *CP* violation with $B^0 \to D^+D^-$ and $B_s^0 \to D_s^+D_s^-$ decays[1]. The two decay modes are analysed in parallel, as the analysis strategy is very similar and the similarities between the two decays can be exploited. Considerations specific to the individual measurements and the results are presented in Chap. 6 and Chap. 7.

The analyses were developed in collaboration with Philipp Ibis and Antje Mödden within the LHCb group in Dortmund and Conor Fitzpatrick from the University of Manchester. The results have been published in the Journal of High Energy Physics [24]. The author contributed to almost all parts of the project. The FT calibration was developed by Aron Kordt in his Bachelor thesis [101], which was supervised by the authors of the analyses. To give a comprehensive overview, all analysis steps are presented, with particular focus on the author's significant contributions to the multivariate selection, the final decay-time fit, and the systematic studies. Additional information regarding the other parts of the project can be found in the doctoral theses of Philipp Ibis [102] and Antje Mödden [103].

The analyses are conducted using the Run 2 data set collected by the LHCb experiment corresponding to an integrated luminosity of $6\,\text{fb}^{-1}$. A considerable amount of background is present in the data. To be able to measure the *CP* observables, the two signal decays, $B^0 \to D^+D^-$ and $B_s^0 \to D_s^+D_s^-$, are at first selected as described in Sec. 5.1. The *CP* observables derived in Sec. 2.6 are measured using the selected signal candidates as explained in Sec. 5.2.

5.1 Selection of signal candidates

A B-meson candidate is reconstructed by combining two oppositely charged D mesons, which are in turn reconstructed from their decays into three charged kaons and pions. Finding such a candidate is a challenging task because in one event, around 200 and sometimes even up to 1000 tracks are measured, and the majority belong to charged kaons and pions. This leads to the reconstruction of many background candidates as unrelated track combinations frequently pass the selection requirements. This is referred to as combinatorial background, and it typically represents the largest source of background when using fully hadronic final states.

[1] If not stated otherwise *CP* conjugated decays are always implied

Additional background contributions arise due to decays of other particles reconstructed as signal candidates. Although their contribution is much smaller, these candidates have similar kinematic properties to the signal candidates, which makes the selection more challenging. In the presented analyses, the dominant contributions are caused by incorrectly identified final-state particles. Due to the wrong particle hypothesis being assigned, background decays can be reconstructed as signal candidates. In the first part of the analysis, a selection is developed to reduce these background sources.

The two signal decays are filtered through the same stripping line. Analysis-specific criteria on the reconstructed D-meson masses are applied to reduce the combinatorial background. The boundaries are chosen so that $D^{\pm}$ and $D_s^{\pm}$ mesons are separated, and thus, the two decay channels can be distinguished. Requirements on the D-meson flight distances suppress backgrounds from single-charm decays of the form $B \to Dhhh$. Various decays with misidentified final-state particles have to be considered. Most of them are suppressed using simultaneous requirements on invariant masses and PID variables. Decays that cannot be efficiently suppressed by these requirements are removed by a BDT. A second BDT is trained to suppress the remaining combinatorial background. In all selection steps, a compromise has to be found between signal efficiency and background suppression. Throughout the analysis, the signal efficiency is monitored with simulated signal decays. The combinatorial background suppression is validated using the upper-mass sideband of the recorded data. If necessary, the suppression of background decays is computed using simulated background decays.

The selected data set mainly contains signal decays. Still, a small contribution from the combinatorial background remains. The invariant mass of the B candidates is modelled to compute the signal weights using the *sPlot* technique described in Sec. 4.3. These weights are used to statistically subtract the remaining background and obtain the decay-time distribution of signal candidates. Mass fits to simulated data are used to determine the shape of the signal model. The remaining combinatorial background is described by an exponential function.

5.2 Measurement of the *CP* observables

The background-subtracted decay-time distribution enables the extraction of the *CP* observables by performing a maximum likelihood fit. The theoretical time-dependent PDFs are proportional to the decay rates in Eq. (2.30) for initially produced B ($d' = 1$) and $\overline{B}$ ($d' = -1$) mesons and are given by

$$\mathcal{B}_{\text{theo}}(t, d') \propto e^{-\Gamma t} \left[\cosh \frac{\Delta\Gamma t}{2} + D \sinh \frac{\Delta\Gamma t}{2} + d'\, C \cos \Delta m t - d'\, S \sin \Delta m t \right] , \tag{5.1}$$

where the overall normalisation is omitted and only the parts relevant for the following discussion are shown. In the following, modifications to the theoretical PDFs are described to account for experimental effects. The true flavour d' of the reconstructed candidates is not known and has to be incorporated into the PDF using the FT introduced in Sec. 3.4. The individual PDFs for the two possible production flavours are multiplied by the probabilities,

$$P(\vec{d}\,|\,d') = \prod_i P(d^i\,|\,d') = P(d^{\mathrm{SS}}\,|\,d')\,P(d^{\mathrm{OS}}\,|\,d')\,, \tag{5.2}$$

of observing the tags $\vec{d}$ given the true flavour d'. Here, the OS and SS combinations are already performed as explained in Sec. 3.4.2. The probabilities of observing the individual tags are defined as

$$P(d^i\,|\,d') = \begin{cases} \epsilon^i_{d'}(1-\omega^i_{d'}) & ,\text{if } d^i = d' \\ \epsilon^i_{d'}\omega^i_{d'} & ,\text{if } d^i = -d' \\ (1-\epsilon^i_{d'}) & ,\text{if } d^i = 0 \end{cases}, \tag{5.3}$$

which can be rewritten as

$$P(d^i\,|\,d') = \begin{cases} \frac{1}{2}\epsilon^i_{d'}\left[1 + d'd^i(1-2\omega^i_{d'})\right] & ,\text{if } d^i = \pm 1 \\ (1-\epsilon^i_{d'}) & ,\text{if } d^i = 0 \end{cases}. \tag{5.4}$$

This can be used to write down the total PDF as

$$\mathcal{B}(t,\vec{d}) = P(\vec{d}\,|\,B)\mathcal{B}_{\mathrm{theo}}(t,1) + P(\vec{d}\,|\,\overline{B})\mathcal{B}_{\mathrm{theo}}(t,-1)\,. \tag{5.5}$$

To account for differences in the production of B and $\overline{B}$ mesons, the production asymmetry A_{prod} is introduced according to

$$\begin{aligned} \mathcal{B}(t,\vec{d},\vec{\omega}) =& (1-A_{\mathrm{prod}})\,P(\vec{d}\,|\,B)\,\mathcal{B}_{\mathrm{theo}}(t,1) \\ &+(1+A_{\mathrm{prod}})\,P(\vec{d}\,|\,\overline{B})\,\mathcal{B}_{\mathrm{theo}}(t,-1)\,. \end{aligned} \tag{5.6}$$

Substituting $\mathcal{B}_{\mathrm{theo}}(t,d')$ with Eq. (5.1) yields the PDF

$$\begin{aligned} \mathcal{B}(t,\vec{d},\vec{\omega}) = e^{-\Gamma t}\Bigg[&(P(\vec{d}\,|\,B)(1-A_{\mathrm{prod}}) + P(\vec{d}\,|\,\overline{B})(1+A_{\mathrm{prod}}))\,\cosh\frac{\Delta\Gamma t}{2} \\ &+(P(\vec{d}\,|\,B)(1-A_{\mathrm{prod}}) + P(\vec{d}\,|\,\overline{B})(1+A_{\mathrm{prod}}))\,D\,\sinh\frac{\Delta\Gamma t}{2} \\ &+(P(\vec{d}\,|\,B)(1-A_{\mathrm{prod}}) - P(\vec{d}\,|\,\overline{B})(1+A_{\mathrm{prod}}))\,C\,\cos\Delta m t \\ &-(P(\vec{d}\,|\,B)(1-A_{\mathrm{prod}}) - P(\vec{d}\,|\,\overline{B})(1+A_{\mathrm{prod}}))\,S\,\sin\Delta m t\Bigg] \end{aligned}. \tag{5.7}$$

This can be simplified to

$$\begin{aligned} \mathcal{B}(t,\vec{d},\vec{\omega}) = e^{-\Gamma t}\Bigg[&(\Delta^+ - A_{\mathrm{prod}}\Delta^-)\,\cosh\frac{\Delta\Gamma t}{2} \\ &+(\Delta^+ - A_{\mathrm{prod}}\Delta^-)\,D\,\sinh\frac{\Delta\Gamma t}{2} \\ &+(\Delta^- - A_{\mathrm{prod}}\Delta^+)\,C\,\cos\Delta m t \\ &-(\Delta^- - A_{\mathrm{prod}}\Delta^+)\,S\,\sin\Delta m t\Bigg] \end{aligned} \tag{5.8}$$

by absorbing all tagging information into the functions

$$\Delta^{\pm} = P(\vec{d}\,|\,B) \pm P(\vec{d}\,|\,\overline{B})\,. \tag{5.9}$$

Using Eq. (5.4), these functions can be explicitly written for the four different cases as follows:

$$\Delta^{\pm} = \begin{cases} \frac{1}{4}\epsilon_{d'}^{\mathrm{OS}}\left[1 + d_i^{\mathrm{OS}}(1-2\omega_{d'}^{\mathrm{OS}})\right]\epsilon_{d'}^{\mathrm{SS}}\left[1 + d_i^{\mathrm{SS}}(1-2\omega_{d'}^{\mathrm{SS}})\right] & \\ \pm\frac{1}{4}\epsilon_{d'}^{\mathrm{OS}}\left[1 - d_i^{\mathrm{OS}}(1-2\omega_{d'}^{\mathrm{OS}})\right]\epsilon_{d'}^{\mathrm{SS}}\left[1 - d_i^{\mathrm{SS}}(1-2\omega_{d'}^{\mathrm{SS}})\right] & \text{, if both tagged} \\ \frac{1}{2}\epsilon_{d'}^{\mathrm{OS}}\left[1 + d_i^{\mathrm{OS}}(1-2\omega_{d'}^{\mathrm{OS}})\right](1-\epsilon_{d'}^{\mathrm{SS}}) & \\ \pm\frac{1}{2}\epsilon_{d'}^{\mathrm{OS}}\left[1 - d_i^{\mathrm{OS}}(1-2\omega_{d'}^{\mathrm{OS}})\right](1-\epsilon_{d'}^{\mathrm{SS}}) & \text{, if OS tagged} \\ \frac{1}{2}\epsilon_{d'}^{\mathrm{SS}}\left[1 + d_i^{\mathrm{SS}}(1-2\omega_{d'}^{\mathrm{SS}})\right](1-\epsilon_{d'}^{\mathrm{OS}}) & \\ \pm\frac{1}{2}\epsilon_{d'}^{\mathrm{SS}}\left[1 - d_i^{\mathrm{SS}}(1-2\omega_{d'}^{\mathrm{SS}})\right](1-\epsilon_{d'}^{\mathrm{OS}}) & \text{, if SS tagged} \\ (1-\epsilon_{d'}^{\mathrm{OS}})(1-\epsilon_{d'}^{\mathrm{SS}}) \pm (1-\epsilon_{d'}^{\mathrm{OS}})(1-\epsilon_{d'}^{\mathrm{SS}}) & \text{, if untagged} \end{cases}. \tag{5.10}$$

The mistag probabilities, $\omega_{d'}^{i}$, are obtained using the calibration approach described in Sec. 3.4.2. Since the uncertainties of the calibration parameters are taken into account by using Gaussian constraints in the decay-time fit, the final PDF depends on the calibration parameters, and the predicted mistags, η^i.

The decay time is determined by measuring the distance between the PV and the decay vertex of the B meson, as well as its momentum. The spatial and momentum resolution of the detector leads to a smearing of the measured decay time. These resolution effects are taken into account in the decay-time fit by convolving the PDF with a resolution function, $\mathcal{R}(t-t')$, with the measured and true decay-time t and t'. The resolution function is determined either using simulated data, where the resolution is known or candidates originating from the PV, where the decay time is zero per definition, and only resolution and bias effects are present.

Finally, an acceptance function, $\epsilon(t)$, is introduced to account for decay-time-dependent efficiency effects. As shown in Ref. [104], this dependence is caused by the reconstruction of tracks in the VELO. Tracks are assumed to originate approximately from the PV, which does not apply to particles from decays of long-lived B mesons. This leads to a reduction of the reconstruction efficiency at large decay times. Displacement requirements of the trigger and the offline selection cause additional inefficiencies for short decay times. The decay-time-dependent efficiency is parameterised by a sum of piecewise polynomials. The cubic B-splines [105] are

defined by k spline positions, the coefficients c_i and the basis functions $q_i(t)$ and are given by

$$\epsilon(t) = \sum_{i=1}^{k} c_i q_i(t) \,. \tag{5.11}$$

The spline positions are found using simulated signal decays. The coefficients in the final decay-time fit are free to vary.

The final PDF as a function of the measured decay time, the tagging decisions and the predicted mistags is given by

$$\mathcal{P}(t, \vec{d}, \vec{\eta}) = \epsilon(t) \cdot \left[\mathcal{B}(t', \vec{d}, \vec{\eta}) \otimes \mathcal{R}(t - t') \right] \,. \tag{5.12}$$

In the final step, the uncertainties of the measurement are studied. Uncertainties are usually divided into two categories: statistical and systematic uncertainties. The statistical uncertainty stems from the finite size of the data sample and is determined in the maximum likelihood fit by numerically computing the covariance matrix for all fit parameters. This statistical uncertainty includes contributions arising from external parameters, which are taken into account by Gaussian constraints. Systematic uncertainties, on the other hand, are caused by methods used and assumptions made in the measurement. Measurements of *CP* violation are very complex and involve many analysis steps that can cause biases in the measured values of the *CP* observables. Studies are performed to estimate the impact of the different sources and, if necessary, assign a systematic uncertainty. This is usually done by generating pseudoexperiments. The distributions relevant to the measurement are generated using the corresponding mass and decay-time PDFs. The parameters are taken from the nominal mass and decay-time fits to the recorded data. Additional distributions, such as the estimated mistags, are generated with weighted histograms from recorded data using the weights obtained from the *sPlot* technique. This approach allows for the generation of many samples, and different assumptions can be tested by simply adjusting the PDFs. Similar to the bootstrap method explained in Sec. 4.4, the nominal fit procedure is applied to each pseudoexperiment. Mass fits are performed to obtain the background subtracted decay-time distribution, and the *CP* observables are measured by performing the decay-time fit. The results are compared to the nominal result. If the mean of the residual distribution is not compatible with zero, it is assigned as a systematic uncertainty. To save computational resources, a systematic that is expected to be small can be estimated by performing a second fit with an alternative model. The difference between the nominal and the alternative fit is assigned as a systematic uncertainty. However, if a large value is observed, pseudoexperiments are preferred to obtain a more accurate estimate.

6 Measurement of *CP* violation in $B^0 \to D^+D^-$ decays

This chapter presents the measurement of the *CP* observables $S_{D^+D^-}$ and $C_{D^+D^-}$ using a sample of $B^0 \to D^+D^-$ decays collected in Run 2 by the LHCb experiment. A previous analysis has been conducted by LHCb with the Run 1 data set [106]. Additional measurements of this decay channel have been carried out by the BaBar [107] and Belle [108] collaborations.

The selection is described in Sec. 6.1. In addition to $B^0 \to D^+D^-$ decays, a sample of $B^0 \to D_s^+D^-$ decays is selected, which is used as a control channel to calibrate the FT response. The time-independent part of the analysis is concluded by the mass fits presented in Sec. 6.2. The decay-time fit procedure, used to extract the *CP* observables, is described in Sec. 6.3. Validation studies of the fit strategy are presented in Sec. 6.4. The systematic uncertainties are discussed in Sec. 6.5. A combination of the results with the Run 1 measurement is conducted, and the individual and combined results are presented in Sec. 6.6.

6.1 Selection

The measurement is conducted using Run 2 proton-proton collision data recorded at a centre-of-mass energy of 13 TeV. The data set corresponds to an integrated luminosity of $6\,\text{fb}^{-1}$ and was collected during the years 2015–2018. The $D^\pm$ candidates are reconstructed using the two decays $D^+ \to K^-\pi^+\pi^+$ and $D^+ \to K^-K^+\pi^+$. The $D^+ \to K^-\pi^+\pi^+$ decay has an approximately ten times higher branching fraction than the $D^+ \to K^-K^+\pi^+$ decay. Candidates whose $D^\pm$ mesons both decay via the $D^+ \to K^-K^+\pi^+$ mode are not considered as the increase in statistical power of the data sample is negligible. Reconstructing one of the $D^\pm$ mesons as $D^+ \to K^-K^+\pi^+$ decay increases the number of signal candidates by about 20%. This leaves the final-state combinations summarised in Tab. 6.1.

In parallel, $B^0 \to D_s^+D^-$decays are selected and used for control studies. The $D^\pm$ mesons are reconstructed using the same decays as for the signal channel. The $D_s^\pm$ mesons are reconstructed via the decays $D_s^+ \to K^-K^+\pi^+$, $D_s^+ \to \pi^-K^+\pi^-$ and $D_s^+ \to \pi^-\pi^+\pi^+$, from which the first decay has the highest branching fraction. One of the D mesons is required to be reconstructed from its decay with the highest branching fraction. The final-state combinations are summarised in Tab. 6.1. The

Table 6.1: Final-state combinations used in the selection of $B^0 \to D^+ D^-$ and $B^0 \to D_s^+ D^-$ decays.

Decay	Final-state decays	
$B^0 \to D^+ D^-$	$D^+ \to K^- \pi^+ \pi^+$	$D^- \to K^+ \pi^- \pi^-$
	$D^\pm \to K^\mp K^\pm \pi^\pm$	$D^\mp \to K^\pm \pi^\mp \pi^\mp$
$B^0 \to D_s^+ D^-$	$D_s^+ \to K^- K^+ \pi^+$	$D^- \to K^+ \pi^- \pi^-$
	$D_s^+ \to K^- K^+ \pi^+$	$D^- \to K^+ K^- \pi^-$
	$D_s^+ \to \pi^- K^+ \pi^-$	$D^- \to K^+ \pi^- \pi^-$
	$D_s^+ \to \pi^- \pi^+ \pi^+$	$D^- \to K^+ \pi^- \pi^-$

additional $D_s^\pm$ decay modes are mainly relevant to the second measurement of $B_s^0 \to D_s^+ D_s^-$ decays described in Chap. 7.

Simulated samples of both channels with the same final states are selected in parallel. They are used for validation studies, calculating the selection efficiencies and parameterising signal distributions.

6.1.1 Preselection

The first stage of the preselection is the centralised preselection introduced in Sec. 3.3.3. It aims to reduce the data by preselecting candidates with a similar topology. The output of the stripping line used in this analysis contains neutral beauty-meson candidates reconstructed from two charged charm mesons, which subsequently decay into any combination of three charged kaons or pions. Due to the loose restrictions on the invariant masses, the preselection does not differentiate between B^0 and B_s^0 mesons or D^+ and D_s^+ mesons. Therefore, the output contains signal candidates and candidates from the control channel. Although these requirements are not developed within this analysis, they are briefly summarised below.

Candidates are required to be selected either by a topological trigger, which searches for secondary vertices with two, three or four tracks, or the inclusive ϕ trigger, which selects ϕ candidates that are likely to originate from a B decay. The candidates must have less than 500 tracks in the event because the high occupancy of the detector leads to worse track reconstruction.

The final-state particles are required to have a good track quality. The χ^2_{IP} of a track is the difference between the χ^2 of some vertex fit, usually the PV, with and without taking the track into account. It is usually small for tracks originating from the PV. Thus, a large χ^2_{IP} with respect to the PV is required for the final-state particles. The tracks must have a low ghost probability [109] to suppress tracks reconstructed from unrelated detector hits. PID information is used to ensure a high likelihood of the final-state particles being either a kaon or a pion. To guarantee that the

final-state particles originate from decays of heavy mesons, they must have high transverse and total momentum.

The D mesons are required to have a good-quality vertex displaced from the PV. The direction angle (DIRA), which is the cosine of the angle between the momentum and the vector pointing from the PV to the D vertex, is required to be greater than zero to ensure that the D mesons fly in the forward direction. The reconstructed D mass is restricted to lie within a window from $100\,\mathrm{MeV}/c^2$ below the known D^+ mass to $100\,\mathrm{MeV}/c^2$ above the known D_s^+ mass taken from the Particle Data Group (PDG) [27]. Pairs of tracks forming a D candidate are required to have a distance of closest approach, which is the smallest distance between two tracks, of less than 0.5 mm to ensure that the tracks originate from the same vertex.

The reconstructed B-mass window is 4900–$6000\,\mathrm{MeV}/c^2$ to select both B^0 and B_s^0 mesons. Candidates above the B_s^0 mass are typically used for studies of combinatorial background, and the upper boundary is chosen to retain enough of these candidates. A good-quality B vertex is required. Requirements on the difference between the z positions of the B vertex and the D vertices are used to ensure that the D mesons decay downstream of the B meson. To guarantee that the B meson originates from the PV, its DIRA is required to be greater than 0.999, and the χ^2_{IP} of the B^0 meson with respect to the PV has to be small. Backgrounds from the PV are suppressed by requiring a minimum reconstructed B decay time of 0.2 ps.

Analysis-specific requirements are applied in addition to the centralised preselection. The mass windows of the reconstructed D masses are tightened to $\pm 45\,\mathrm{MeV}/c^2$ around their known value corresponding to approximately ± 4 times the mass resolution. These values are chosen to separate the D^+ and D_s^+ mass regions, which makes it possible to distinguish between $B^0 \to D^+D^-$ and $B^0 \to D_s^+D^-$decays and efficiently reduce the combinatorial background. A requirement on the flight distance of all charm mesons is applied to reduce single-charm decays.

The additional requirements reduce the combinatorial background by about 88%, calculated using candidates from the upper mass sideband of recorded data defined by $m_{D^+D^-} > 5600\,\mathrm{MeV}/c^2$. A signal efficiency of about 77% is achieved, and the efficiency of $B^0 \to D_s^+D^-$decays is about 68%. The requirement on the D lifetime causes the low efficiency. However, it is necessary to suppress the single-charm background, which is a dominant source of systematic uncertainty in the Run 1 analysis. The reason for the lower efficiency of the control channel is the shorter D_s^+ lifetime. Figure 6.1 shows the effect of the analysis-specific requirements on the reconstructed B^0 mass of $B^0 \to D^+D^-$ candidates. A large amount of the combinatorial background is suppressed, and a more pronounced peak at the known B^0 mass is visible after the preselection.

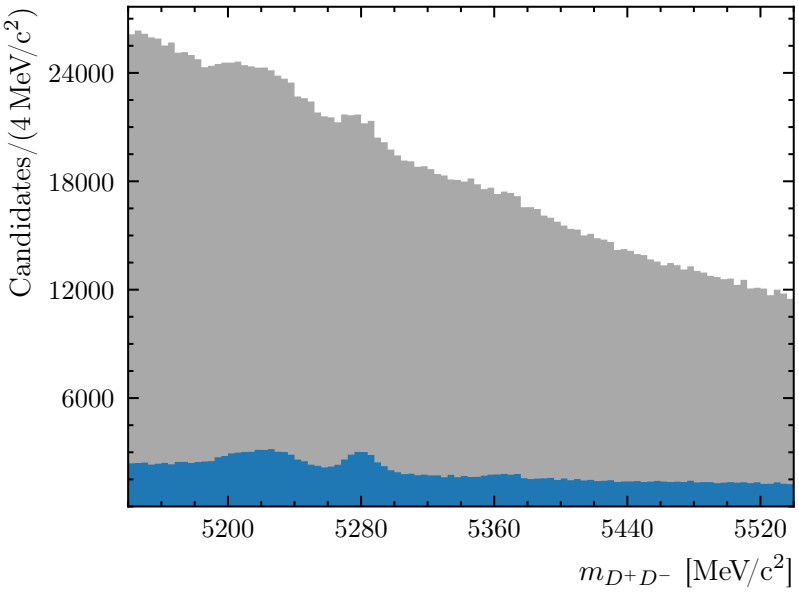

Figure 6.1: Reconstructed B^0-mass distribution of $B^0 \to D^+D^-$ candidates. The blue histogram shows the distribution of the candidates retained after the preselection. The grey area represents the candidates rejected by the analysis-specific preselection requirements.

6.1.2 Vetoes

Significant contributions from background decays are visible in the reconstructed B^0-mass distribution of the preselected candidates. They are caused by the incorrect identification of final-state kaons and pions. Since the wrong mass is assigned to the final-state particles, distorted peaks are visible in the B^0- and $D^\pm$-mass distributions. This effect can be seen in Fig. 6.1, where a broad peak is visible in the range of 5200–5260 MeV/c^2 due to wrongly reconstructed $B^0 \to D_s^+D^-$ decays. These backgrounds are identified by recalculating invariant masses with alternative particle hypotheses. The kaon, pion and proton masses are assigned to the final-state particles, and the alternative invariant mass is calculated for all possible combinations. If background decays are present, they can be identified in these distributions. For the three-body combinations, backgrounds from D_s^+ and Λ_c^+ decays are considered. Two-body combinations are calculated to identify backgrounds from neutral ϕ and D^0 decays. Finally, if D^0 decays are present in the two-body masses without any misidentification, they are still rejected because decays of the form $D^+ \to D^0h^+$ are impossible.

The background decays can be suppressed by simultaneous requirements on PID variables and the alternative invariant masses. This is called a veto. The PID variables used in this analysis are referred to as ProbNN variables. They provide probability estimates of particle hypotheses and are computed by a neural network based

on information from the PID detectors components. In the following, background decays are individually identified, and for each final-state particle, an explicit distinction is made between the two hypotheses. In this case, the separation power can be increased by using the ratio

$$\text{ProbNN}_{p_1 p_2} = \frac{\text{ProbNN}_{p_1}}{\text{ProbNN}_{p_1} + \text{ProbNN}_{p_2}} \tag{6.1}$$

to distinguish between the two particle hypotheses p_1 and p_2. If a background decay is identified, candidates whose alternative mass lies within the region of the background hadron are only retained if the potentially misidentified particles fulfil certain requirements on the ProbNN variable. The requirement on the ProbNN variable is tightened until the background contribution vanishes. In cases where the background decay has two possibilities to mimic the signal decay due to two final-state particles being the same, the veto is developed for the high and low p_T particles separately. This exploits the fact that the performance of the PID detectors depends on the momentum of the particles and enables a more efficient suppression. The vetoes are developed individually for the different $D^\pm$ final states. In the following, the rejected background decays are briefly described. More information about the requirements can be found in Ref. [102].

Vetoes in $\boldsymbol{D^+ \to K^-\pi^+\pi^+}$ decays: Contributions from $\phi \to K^+K^-$ decays arise if a kaon is misidentified as one of the final-state pions. The same misidentification causes contributions from $D^0 \to K^+K^-$ decays. In this case, only the pion with the higher p_T shows a significant contribution. Assigning the proton mass to the pion with the higher p_T shows contributions from $\Lambda_c^+ \to K^- p \pi^+$ decays. Finally, a background from misidentified single-charm decays, *i.e.* $B^0 \to \pi^-\pi^+\pi^+ D^-$ decays, is present. They are rejected using ProbNN requirements without restricting the invariant mass.

Vetoes in $\boldsymbol{D^+ \to K^-K^+\pi^+}$ decays: Contributions from $\phi \to K^+K^-$ decays occur if a kaon is misidentified as the pion in the $D^+ \to K^-K^+\pi^+$ decay. The decay $D_s^+ \to K^-\pi^+K^+$ causes a significant contribution due to the pion and kaon with the same charge being misidentified as each other. Background arises from $\Lambda_c^+ \to K^- p \pi$ decays if the proton is misidentified as a kaon. The same decay contributes if the proton is misidentified as a pion and the pion is misidentified as a kaon. Finally, $D^0 \to K^+K^-$ decays without any misidentification are rejected by a requirement on the two-body mass of the kaons.

Efficiencies: These vetoes are also applied to the $D^\pm$ mesons of the $B^0 \to D_s^+ D^-$ sample. Additional background contributions must be considered for the $D_s^\pm$ mesons. They are discussed in Sec. 7.1.2 as the same requirements are used in the analysis of $B_s^0 \to D_s^+ D_s^-$ decays. The efficiency is approximately 96% for $B^0 \to D^+ D^-$ decays and 94% for $B^0 \to D_s^+ D^-$ decays.

Multivariate classification of $D^+ \to K^-\pi^+\pi^+$ and $D_s^+ \to K^-K^+\pi^+$ decays

A particularly challenging background originates from the decay $D_s^+ \to K^-K^+\pi^+$, in which the K^+ is misidentified as a π^+. Due to the lower mass assigned to the kaon, the reconstructed three-body mass is shifted from the D_s^+ region into the D^+ region. This causes a significant background contribution, in particular, due to $B^0 \to D_s^+ D^-$ decays, which have a much higher branching fraction than the signal decay. It is one of the main background sources in this measurement and has to be efficiently suppressed. The shift from the D_s^+ region to the D^+ region makes a veto based on only the ProbNN variable and the invariant mass inefficient. Hence, a BDT is trained to distinguish between the two decays. This approach also enables the classification of background from $D^+ \to K^-\pi^+\pi^+$ decays in $D_s^+ \to K^-K^+\pi^+$ decays with the same BDT. This background is present in the $B^0 \to D_s^+ D^-$ control channel and suffers from the same inefficiencies that require using a BDT.

Simulated $B^0 \to D^+ D^-$, $B^0 \to D_s^+ D^-$ and $B_s^0 \to D_s^+ D_s^-$ samples with the relevant final states are used to train a BDT separately for positively and negatively charged D mesons. The candidates are labelled according to their D decay channel, one label representing $D^+ \to K^-\pi^+\pi^+$ decays and the other $D_s^+ \to K^-K^+\pi^+$ decays. The same is done for the negatively charged D mesons, and the procedure explained in the following is applied to both. A k-fold cross-validation is used, where the training data is split into five equal parts, four of which are used to train the BDT that is applied to the remaining part. The procedure is repeated until the BDT is applied to all candidates. This approach allows to keep all data for the following analysis and reduces the risk of overtraining. The hyperparameters were developed for the BDT presented in Sec. 6.1.3, which is used to suppress combinatorial background. They are not adjusted because no performance improvement was observed when changing them. The performance is measured using the area under the receiver operating characteristic (ROC) curve, in the following referred to as ROC score. The ROC curve plots the true positive rate against the false positive rate. Up to 1000 trees with a maximum depth of three are used. The learning rate is set to 0.5. To avoid overtraining, the training is stopped if the ROC score on the validation sample does not improve for ten iterations. The BDT is trained using gradient boosting with the XGBoost package [93].

In Tab. 6.2, the training features are listed. The intuitive choice of training features are the variables used for the vetoes, *i.e.* the ProbNN variables of the potentially misidentified particles and the invariant three-body masses with the alternative particle hypotheses. Both the pion and kaon ProbNN variables are used. Decays with intermediate resonances such as $D_s^+ \to \phi\pi^+$ decays where ϕ decays into a pair of charged kaons or several $\overline{K}^{*0} \to K^-\pi^+$ resonances from $D^+ \to \overline{K}^{*0}\pi^+$ decays are exploited by adding the invariant two-body masses with the alternative particle hypotheses to the training features. The flight distance, FD, is used because of the different average lifetimes of D^+ and D_s^+ mesons.

Table 6.2: Training features of the BDT to distinguish between $D^+ \to K^-\pi^+\pi^+$ and $D_s^+ \to K^-K^+\pi^+$ decays. They are sorted by their importance in the training. The final-state particles with the same charge as the mother D meson are referred to as h_1 and h_2.

Training feature
$m_{K^-\pi^+\pi^+}$
$\text{ProbNN}_K(h_1/h_2)$
$m_{K^-K^+\pi^+}$
$m_{K^-\pi^+K^+}$
$\text{ProbNN}_\pi(h_1/h_2)$
$m_{K^-\pi^+_{1,2}}$
$m_{K^-K^+_{1,2}}$
$\text{FD}(D)$

The BDT is applied to the collected data, assigning each candidate a value between 0 and 1. Candidates with values closer to 1 are more likely to be $D_s^+ \to K^-K^+\pi^+$ decays, while candidates with smaller values are probably $D^+ \to K^-\pi^+\pi^+$ decays. The left plot in Fig. 6.2 shows the distribution of the BDT response for the training and test samples of positively charged D mesons. The distributions are in agreement and show no sign of overtraining. The ROC curve is shown in the right plot of Fig. 6.2 and a ROC score of 0.9993 is achieved. Similar results are obtained for negatively charged D mesons.

A value of the BDT response below 0.07 is required for $D^+ \to K^-\pi^+\pi^+$ candidates to be selected. In the case of $D_s^+ \to K^-K^+\pi^+$ decays, only candidates with values greater than 0.98 are retained. The requirements are chosen to reject more than 99% of the respective background decays in the simulated samples. As shown in the left plot of Fig. 6.3, this is sufficient to suppress the pollution of $B^0 \to D_s^+D^-$decays in recorded $B^0 \to D^+D^-$ data to negligible levels. The right plot in Fig. 6.3 shows the distribution of the invariant $K^\mp K^\pm\pi^\pm$ mass before and after applying the BDT requirements. The distribution of $D^\pm$ candidates with higher p_T is shown for better visualisation because the background contribution is more pronounced for these candidates. No sign of $D_s^+ \to K^-K^+\pi^+$ decays is visible in the distribution of the retained candidates, which confirms the observations from simulated data.

About 95% and 89% of $B^0 \to D^+D^-$ signal decays are retained depending on whether the BDT requirement has to be applied to one or both $D^\pm$ mesons. The signal efficiency of the $B^0 \to D_s^+D^-$ control channel ranges from 88% to 95% depending on the final state. The remaining contributions in the distribution of the reconstructed B^0 mass originate from $B^0 \to D^+D^-$ signal decays, $B_s^0 \to D^+D^-$ background decays and combinatorial background.

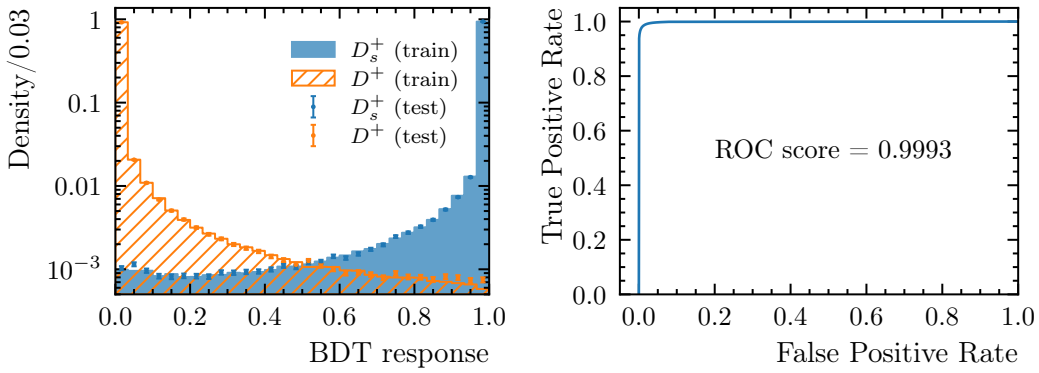

Figure 6.2: Performance plots of one BDT fold to distinguish between $D^+ \to K^-\pi^+\pi^+$ and $D_s^+ \to K^-K^+\pi^+$ decays. The distributions of the BDT response for the training and test samples are shown on the left. The ROC curve is shown on the right.

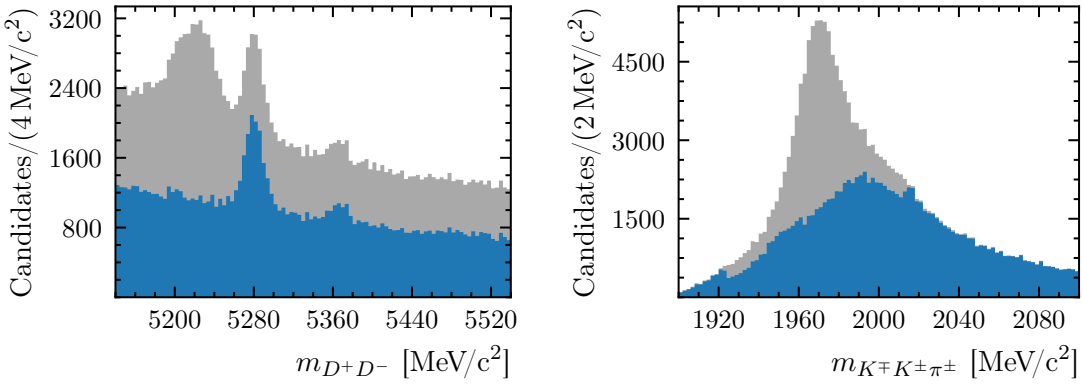

Figure 6.3: The (left) reconstructed B^0-mass distribution of $B^0 \to D^+D^-$ candidates. The blue histogram shows the distribution of the candidates retained after the veto selection. The grey area represents the candidates rejected by the veto requirements. The right plot shows the invariant $K^\mp K^\pm\pi^\pm$ mass of the $D^\pm$ candidates with the higher p_T. The grey area represents the $D_s^+ \to K^-K^+\pi^+$ contribution rejected by the BDT requirements.

Table 6.3: Training features of the BDT to suppress combinatorial background. They are sorted by their importance in the training.

Training feature
χ^2_{IP} (B)
$m(D) - m_{D^+_{(s)},\text{PDG}}$
χ^2_{IP} $(D^{\pm})$
χ^2_{DTF}
$p_{\text{T}}(K^{\pm}/\pi^{\pm})_D$
p_{T} (D)
$\cos\theta^*_{1,2,3}(D)$
$\text{FD}(D)$

6.1.3 Multivariate selection

A second BDT is used to suppress the remaining combinatorial background. The training is performed using $B^0 \to D^+D^-$, $B^0_s \to D^+_s D^-_s$ and $B^0 \to D^+_s D^-$ candidates. This approach has the advantage that the BDT can be applied to the signal and control channel in both this and the parallel $B^0_s \to D^+_s D^-_s$ measurement. The same BDT selection is applied to the control channel so that the kinematic distributions remain similar, which is essential for the FT calibration. A sample of simulated decays from all three decay channels is used as a signal proxy. The upper-mass sideband of recorded $B^0 \to D^+D^-$, $B^0_s \to D^+_s D^-_s$ and $B^0 \to D^+_s D^-$ data is used as a background proxy. A maximum number of 1000 trees is used, and the training is stopped if the ROC score on the validation sample does not improve for ten iterations. The trees have a maximum depth of three, and the learning rate is 0.5. A k-fold cross-validation with five folds is used. The BDT is trained using the XGBoost package [93].

Various features are tested and iteratively removed based on their importance in the training. As many features as possible are removed to reduce the complexity of the model and, thereby, the risk of overtraining. However, no more features are removed if the BDT performance starts to decrease. The performance is assessed using the ROC score. The final set of features is listed in Tab. 6.3. The restrictions on the reconstructed D masses in the preselection are loose. Consequently, the difference with respect to their known mass from the PDG [27] is used. The χ^2_{IP} indicates if a particle originates from the PV. The χ^2_{IP} of the B meson is used because it is, on average, smaller for the signal than the combinatorial background. The opposite applies to the χ^2_{IP} of the D mesons. Background candidates are expected to have a worse goodness of the DTF fit, χ^2_{DTF}, than signal candidates. Significant transverse momenta of intermediate and final-state particles indicate decays of heavy B mesons. The flight distance of the D mesons is, on average, higher than for the combinatorial background, which is dominantly caused by the combinations of

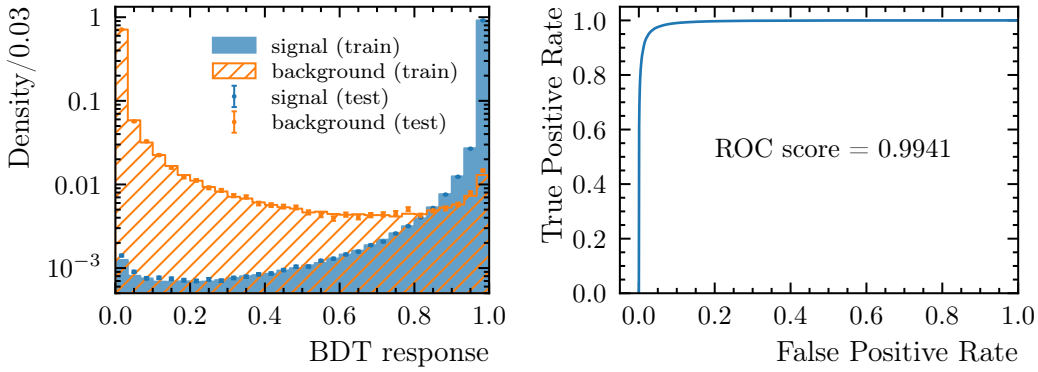

Figure 6.4: Performance plots of one BDT fold to distinguish between signal decays and combinatorial background. The distributions of the BDT response for the training and test samples are shown on the left. The ROC curve is shown on the right.

tracks from the PV leading to a small reconstructed flight distance. Finally, the cosine of the angles between the D mesons and their decay products, $\cos\theta^*_{1,2,3}(D)$, are used.

The output distribution of the BDT response is shown in the left plot of Fig. 6.4. The distributions of the training and test samples are in agreement and show no sign of overtraining. The right plot shows the ROC curve. A good separation power is achieved with a ROC score of 0.9941.

Optimisation of the BDT requirement

After the BDT response is calculated for all candidates, a requirement on the response has to be chosen to select the signal candidates. Choosing a suitable value is always a trade-off between high signal efficiency and high suppression of combinatorial background. Additionally, other factors have to be considered in flavour-tagged time-dependent analyses. The FT and decay-time resolution considerably impact the sensitivity of the measurement. If these effects are correlated with the BDT response, a suitable figure of merit (FOM) has to take this into account. The selected requirement should maximise the sensitivity of the measurement of the CP observables. This is achieved using the inverse of the variance of the parameter $\sin\phi_d^{\text{eff}}$, which depends on both $S_{D^+D^-}$ and $C_{D^+D^-}$. This approach was first used in Ref. [110] and extended in [111] and [112] to include the per-candidate signal weights, ${}_s\mathcal{P}_i$, from the *sPlot* method. The FOM is then given by

$$\text{FOM} = \frac{\left(\sum_i {}_s\mathcal{P}_i\right)^2}{\sum_i {}_s\mathcal{P}_i^2} D, \tag{6.2}$$

where D is defined as

$$D = \frac{1}{\sum_i {}_s\mathcal{P}_i} \sum_i (1-2\omega_i)^2 e^{-(\Delta m_d \delta_{t,i})^2} \cdot {}_s\mathcal{P}_i \cdot X_i, \tag{6.3}$$

with

$$X_i = \left[\frac{2d_i|\lambda|s}{1+|\lambda|^2+d_i(1-\omega_i)e^{-(\Delta m_d \delta_{t,i})^2/2}\left(-2|\lambda|s\sin\phi_d^{\text{eff}} - (1-|\lambda|^2)c\right)} \right]^2 . \tag{6.4}$$

The trigonometric terms are abbreviated with $s = \sin(\Delta m_d t_i)$ and $c = \cos(\Delta m_d t_i)$. The FOM can be broken down into several components to assess the individual contributions. The most dominant term is the effective signal size

$$\frac{\left(\sum_i {}_s\mathcal{P}_i\right)^2}{\sum_i {}_s\mathcal{P}_i^2}. \tag{6.5}$$

The signal weights ${}_s\mathcal{P}_i$ are calculated using a maximum likelihood fit to the reconstructed B^0-mass distributions. New mass fits are performed for each cut value on the BDT response. More information on the mass fits is presented in Sec. 6.2. Effects from the limited knowledge of the decay time are represented by the term

$$\text{FOM}_\sigma = \frac{1}{\sum_i {}_s\mathcal{P}_i} \sum_i {}_s\mathcal{P}_i e^{-(\Delta m_d \delta_{t,i})^2}, \tag{6.6}$$

which favours candidates with small decay-time uncertainty $\delta_{t,i}$. Since the knowledge of the initial flavour is essential for the measurement, the dilution of the data set due to the FT is expressed by the term

$$\text{FOM}_D = \frac{1}{\sum_i {}_s\mathcal{P}_i} \sum_i {}_s\mathcal{P}_i (1-2\omega_i)^2, \tag{6.7}$$

which assigns higher values to candidates with a small mistag probability. As described in Sec. 3.4.2, a calibration has to be developed to obtain the mistag probabilities. Since a fully selected sample is needed to determine this calibration, the first iteration of the analysis uses the mistag estimates, η_i, to calculate the FOM. The calibration is performed as described in Sec. 6.3.1 and applied to the data used to calculate the FOM. The following results are obtained using the calibrated mistag. The FOM depends on the value of $\sin\phi_d^{\text{eff}}$ and other external parameters, which are included in

$$\text{FOM}_{\sin\phi_d^{\text{eff}}} = \frac{1}{\sum_i {}_s\mathcal{P}_i} \sum_i {}_s\mathcal{P}_i \cdot X_i . \tag{6.8}$$

The parameter $|\lambda|$ is assumed to be 1, and the values for Δm_d and $\sin\phi_d^{\text{eff}}$ are taken from the PDG [27]. Instead of the Run 1 result of $\sin\phi_{d,D^+D^-}^{\text{eff}}$, the more precise average over multiple channels is used.

A scan of the BDT response is performed, and the FOM is calculated individually for each final state. The total distribution and the individual contributions

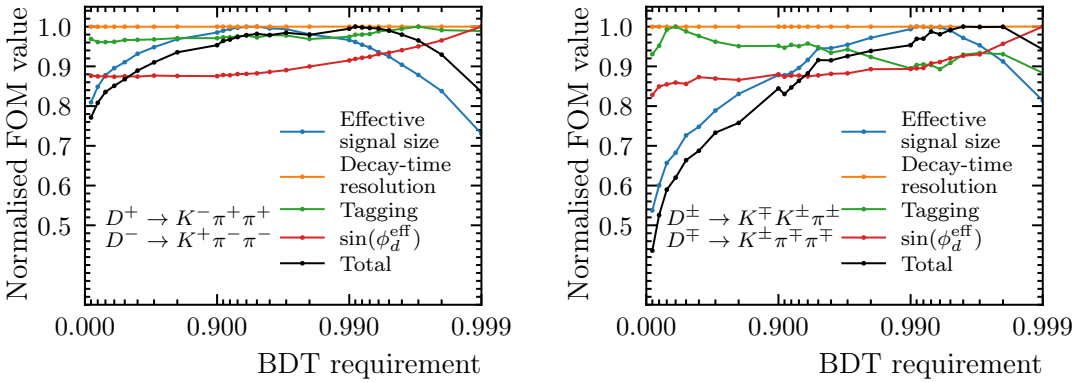

Figure 6.5: Scan of the BDT response using $B^0 \to D^+D^-$ data for the two different final states. The total FOM is calculated by Eq. (6.2) and shown in black. The individual components are explained in the text. All components are normalised to their maximum value.

are shown in Fig. 6.5. For better visualisation, the individual components are normalised to their maximum value. The effective signal size has the largest effect on the total distribution. As expected, the decay-time resolution has a small impact as it is small compared to the oscillation period of B^0 mesons. Minor contributions of the FT dilution and the external parameters are observed. The right plot in Fig. 6.5 shows larger fluctuations because of the fewer number of the $D^+ \to K^-K^+\pi^+$ decays in this final state. However, the flat distribution of the FOM in the left plot indicates a high sensitivity of the measurement over a large range of BDT requirements. This enables the application of the same requirement for both final states, which simplifies the analysis since no distinctions have to be made between the final states in the time-dependent studies. Candidates with a BDT response greater than 0.99 are retained. This requirement has a signal efficiency of about 87% for $B^0 \to D^+D^-$ and 85% for $B^0 \to D_s^+D^-$ decays while 99% of the combinatorial background is rejected. Figure 6.6 shows the effect of the BDT selection on the distribution of the reconstructed B^0 mass of $B^0 \to D^+D^-$ candidates.

6.1.4 Final selection

In the final selection step, the data is prepared for the mass and decay-time fits. The reconstructed B^0 mass is required to be in the range of 5240–5540 MeV/c^2. The upper boundary retains a sufficient amount of combinatorial background candidates to model this contribution in the mass fits. The lower boundary removes backgrounds from decays involving partially reconstructed $D^{*\pm}$ mesons. This is validated using a phase-space-only simulation sample of $B_s^0 \to D^{*\pm}(\to D^\pm\pi^0)D^\mp$ decays generated with RapidSim [113]. The invariant mass of the D^+D^- system is computed neglecting the π^0 meson. The distribution is shown in Fig. 6.7. Tak-

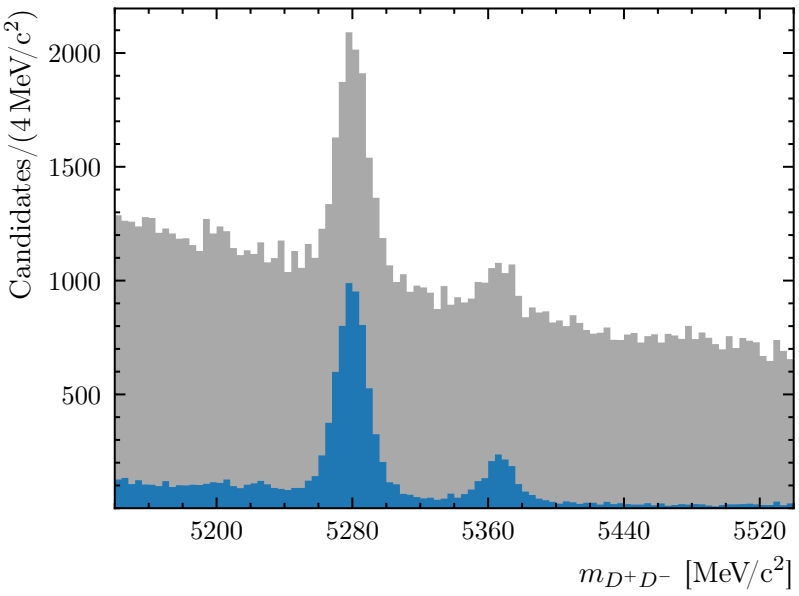

Figure 6.6: Reconstructed B^0-mass distribution of $B^0 \to D^+D^-$ candidates. The blue histogram shows the distribution of the candidates retained after the BDT selection. The grey area represents the candidates rejected by the BDT selection.

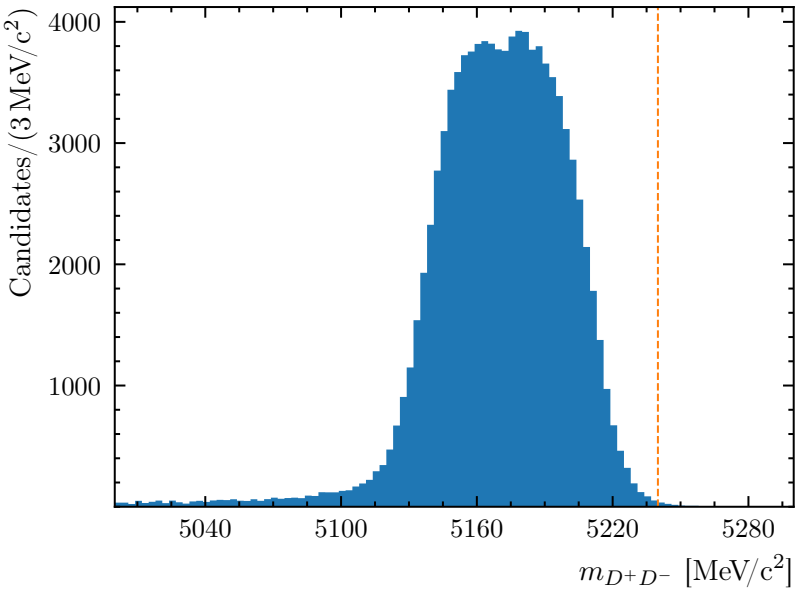

Figure 6.7: Mass distribution of simulated partially reconstructed $B_s^0 \to D^{*\pm}(\to D^{\pm}\pi^0)D^{\mp}$ decays. The invariant mass is calculated neglecting the π^0 meson. The dashed orange line shows the lower boundary of the $B^0 \to D^+D^-$ mass region.

ing the relative branching fractions of $B^0 \to D^+D^-$ and $B_s^0 \to D^{*\pm}D^{\mp}$ into account and assuming the same efficiencies, the background contribution within the reconstructed B^0-mass range is estimated to be below 0.1%. Contributions from other partially reconstructed decays can safely be neglected because they lie below the $B_s^0 \to D^{*\pm}D^{\mp}$ contribution in the D^+D^--mass spectrum. In the Stripping selection described in Sec. 6.1.1, a requirement on the decay time of the B^0 mesons is applied. As explained in Sec. 3.3.3, the decay time used in the central selection steps is not calculated by the DTF. To avoid any effect of this requirement at the lower boundary of the decay-time fit, it is increased, resulting in a decay-time range of 0.3–10.3 ps is required. Above 10.3 ps, almost no signal candidates are present. The selection efficiency of these final requirements is about 96%. For the $B^0 \to D_s^+D^-$ control channel, a different mass range of 5220–5540 MeV/c^2 is chosen. The decay-time range is the same, and the efficiency is about 99%.

Finally, after the entire selection has been applied to the data samples, some events contain more than one candidate. However, the chance that more than one of these candidates is a real signal decay is practically zero. In events with high multiplicity, a candidate can be reconstructed multiple times with just one track being different. Additionally, this can be caused by candidates being reconstructed using the same tracks but assigning a different particle hypothesis to one track. In $B^0 \to D^+D^-$ data, the number of events with multiple candidates ranges from 0.8–1.4%. Since the candidates are usually equally likely to be the signal decay and share the majority of the tracks, only one of the candidates is arbitrarily retained. In $B^0 \to D_s^+D^-$ data, approximately 0.6–1.8% of the events contain multiple candidates, one of which is arbitrarily selected.

6.2 Mass fits

Three sources of candidates remain in the selected data set: $B^0 \to D^+D^-$ signal decays, $B_s^0 \to D^+D^-$ background decays and combinatorial background. To reduce the combinatorial background contribution to negligible levels, a selection as previously described would reduce the signal efficiency too drastically. Therefore, the remaining background candidates are statistically subtracted from the recorded data using the *sPlot* technique. Details on the procedure are given in Sec. 4.3. The basic idea is to calculate a signal weight for each candidate using a discriminating variable. These can be applied to the data set so that the weighted distribution of a target variable only represents the signal candidates. Here, the reconstructed B^0 mass is used as the discriminating variable, and to calculate the signal weights, an extended maximum likelihood fit is performed.

The signal model is determined using simulated $B^0 \to D^+D^-$ decays. A double-sided Hypatia function [114] is used to parameterise the signal distribution. It is a

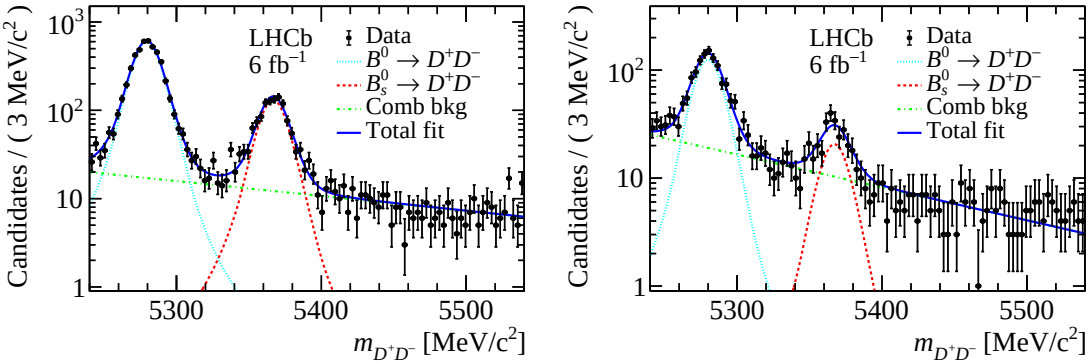

Figure 6.8: Distribution of the reconstructed B^0 mass of $B^0 \to D^+D^-$ candidates and the PDF projections of the fit for the final states, where (left) both $D^\pm$ mesons are reconstructed via $D^+ \to K^-\pi^+\pi^+$ and (right) only one $D^\pm$ meson is reconstructed via $D^+ \to K^-\pi^+\pi^+$ and the other via $D^+ \to K^-K^+\pi^+$ [24].

generalisation of the Crystal Ball (CB) function [115] with CB-like tails and a generalised hyperbolic core. This model can describe resolution effects and non-Gaussian tails originating from photon radiation and mass constraints of intermediate particles. A maximum likelihood fit to the reconstructed B^0-mass distribution of the simulated $B^0 \to D^+D^-$ candidates is conducted to determine the shape parameters of the Hypatia function. The fit is performed separately for each final state to account for possible kinematic differences in the signal shape. More details are provided in Ref. [102].

Three components are considered in the mass fit to the recorded data. The previously discussed Hypatia function describes the $B^0 \to D^+D^-$ signal component. A second Hypatia function is used to model the background decay $B_s^0 \to D^+D^-$, and the combinatorial background is parameterised by an exponential function. Since both the $B^0 \to D^+D^-$ and $B_s^0 \to D^+D^-$ decays have the same final states, the resolution of the reconstructed B mass is expected to be similar. Thus, the parameters of both models are fixed to the values determined using the $B^0 \to D^+D^-$ simulation sample. To account for possible differences between data and simulation, the width and mean of the Hypatia functions are allowed to vary in the fit to recorded data. The fit of the $B_s^0 \to D^+D^-$ component is unstable because of the small number of candidates. Thus, the difference between the mean of the B^0 and B_s^0 components is fixed to the known value taken from the PDG [27]. Additionally, the same width is used for both components to reduce the number of free parameters and stabilise the fit. The exponential slope of the combinatorial background component is free to vary in the fit. Independent mass fits are performed for the two final states and the results are shown in Fig. 6.8. The extended maximum likelihood fits to the recorded data yield 5695 ± 100 $B^0 \to D^+D^-$ candidates. This is about 3.5 times the amount observed in the Run 1 analysis [106] and is consistent with expectations based on

the increase in data and centre-of-mass energy. The PDFs with the parameters determined by the fits are used to calculate the weights with the *sPlot* technique to obtain the background-subtracted decay-time distribution.

The mass fits to the $B^0 \to D_s^+ D^-$ sample are carried out using the same strategy. They are presented in Ref. [102] and not discussed in this thesis.

6.3 Decay-time fit

In the following, the measurement of $S_{D^+D^-}$ and $C_{D^+D^-}$ with the background-subtracted decay-time distribution of $B^0 \to D^+D^-$ candidates is described. The decay-time-dependent studies are performed simultaneously with candidates of all analysed final states. The PDF describing the measured decay-time distribution is of the general form given in Eq. (5.12). This model depends on the observed tagging decisions $\vec{d} = (d^{\mathrm{OS}}, d^{\mathrm{SS}})$, estimated mistags $\vec{\eta} = (\eta^{\mathrm{OS}}, \eta^{\mathrm{SS}})$ and two functions for the FT response. The FT calibration procedure is presented in Sec. 6.3.1. The smearing of the decay time due to detector-resolution effects is parameterised by a resolution function, which is determined as described in Sec. 6.3.2. Decay-time-dependent efficiency effects are taken into account by the acceptance function explained in Sec. 6.3.3. Finally, the extraction of $S_{D^+D^-}$ and $C_{D^+D^-}$ with the decay-time fit is presented in Sec. 6.3.4.

6.3.1 Flavour-tagging calibration

The $B^0 \to D_s^+ D^-$control channel is used to calibrate the mistag estimates, η^i, provided by the taggers to represent the mistag probability, ω^i, in the signal channel. Its flavour-specific final state enables the calibration of the FT response. This channel is chosen due to its kinematic properties, which closely resemble those of the signal channel. This allows the calibration to be applied to the signal data without any corrections. The high branching fraction provides a large calibration sample, which reduces the statistical uncertainty of the calibration.

All available B^0 taggers described in Sec. 3.4 are used in the analysis. The following calibration and combination steps are carried out with the EPM tool [88]. In the first step, the individual taggers are calibrated. The calibrated outputs are combined to provide an OS and SS tag and mistag estimate. The combinations are calibrated to obtain one OS and one SS calibration function. The results of the calibration parameters are summarised in Tab. 6.4. The calibration of the single taggers is applied to the $B^0 \to D^+D^-$ data, and the combinations are computed. Finally, the OS and SS calibration functions are applied to the $B^0 \to D^+D^-$ sample to measure the performance parameters presented in Tab. 6.5. A tagging power of (5.60±0.07)% is achieved.

Table 6.4: Results of the FT calibration obtained using the $B^0 \to D_s^+ D^-$data sample.

	OS Comb.	SS Comb.
p_0	0.016 ± 0.004	-0.0015 ± 0.0022
p_1	0.862 ± 0.034	0.932 ± 0.033
Δp_0	0.003 ± 0.005	0.0014 ± 0.0031
Δp_1	0.01 ± 0.05	-0.04 ± 0.05

Table 6.5: Performance parameters of the FT calibration. The calibration is obtained using $B^0 \to D_s^+ D^-$data and applied to the $B^0 \to D^+ D^-$ sample.

	$\langle \eta \rangle$	ε_{tag} [%]	ε_{eff} [%]
OS Comb.	0.3461	33.2 ± 0.5	3.41 ± 0.09
SS Comb.	0.4255	88.27 ± 0.34	3.15 ± 0.06
OS+SS		91.37 ± 0.29	6.28 ± 0.11

6.3.2 Decay-time resolution

The decay-time resolution is parameterised by

$$\mathcal{R}(t - t') = \sum_{i=1}^{3} f_i \frac{1}{\sqrt{2\pi}\sigma_i} e^{-(t-t'-\mu)^2/2\sigma_i^2}\,, \tag{6.9}$$

where the three Gaussian components have individual widths σ_i and a common mean parameter μ. Only two fractions, f_1 and f_2, are free parameters, while the third fraction is defined by $f_3 = 1 - f_1 - f_2$. The three components account for different sources of resolution effects, *e.g.* candidates that are assigned the wrong PV. The finite decay-time resolution causes a dilution of the *CP* asymmetry by the factor

$$\mathcal{D} = \sum_{i=1}^{3} f_i e^{-\Delta m_d^2 \sigma_i^2/2}\,. \tag{6.10}$$

The decay-time resolution is quantified in terms of an effective resolution

$$\sigma_{\text{eff}} = \sqrt{-\frac{2}{\Delta m_d^2} \ln \mathcal{D}}\,, \tag{6.11}$$

which represents the width of a single Gaussian function with the same dilution factor as the decay-time resolution model. More information on the dilution factor is given in Ref. [116].

The parameters of the model are determined by a fit to the difference between the true and measured decay time of simulated $B^0 \to D^+ D^-$ decays. The distribution

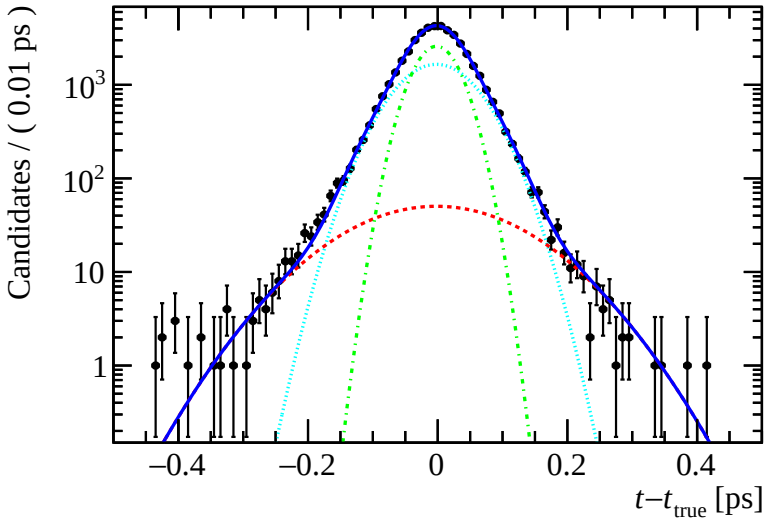

Figure 6.9: Resolution of simulated $B^0 \to D^+D^-$ decays. The difference between the true and measured decay time is shown as points, and the PDF from the fit is overlaid as a solid blue line. The individual Gaussian components are shown as dashed, dotted and dash-dotted lines in different colours.

Table 6.6: Results of the decay-time-resolution fit on the simulated $B^0 \to D^+D^-$ sample.

Parameter	Value
f_1	0.51 ± 0.06
f_2	0.034 ± 0.008
μ[ps]	-0.00197 ± 0.00022
σ_1[ps]	0.0574 ± 0.0024
σ_2[ps]	0.124 ± 0.007
σ_3[ps]	0.0327 ± 0.0014
$\mathcal{D}$	0.9997

and the PDF projection are shown in Fig. 6.9. The fit results of the parameters are given in Tab. 6.6. The final decay-time resolution model has an effective resolution of approximately 52 fs. This is small compared to the oscillation period of B^0 mesons, leading to a dilution factor close to unity.

6.3.3 Decay-time acceptance

The decay-time-dependent efficiency is parameterised by the acceptance function $\epsilon(t)$ in Eq. (5.12). The acceptance function is described by the B-spline model introduced in Sec. 5.2. The spline positions are determined on a simulated $B^0 \to D^+D^-$ sample. A fit to their decay-time distribution is performed with a simplified model. Instead of the entire theoretical model from Eq. (5.1), only a single exponential function with the decay time fixed to the average B^0 lifetime [27] is used. This model is convolved with a decay-time-resolution function and multiplied with the acceptance function according to Eq. (5.12). The parameters of the resolution function and the spline positions are fixed. The only free parameters are the spline coefficients. The splines placed at $0.3, 0.5, 2.7, 6.3$ and 10.3 ps are found to describe the acceptance effects adequately. More splines are placed at low decay times, where the efficiency changes drastically. Figure 6.10 shows the decay-time distribution of simulated $B^0 \to D^+D^-$ candidates, where the effect of the exponential decay is removed. The PDF projections from the fit are overlaid. In the final decay-time fit to the recorded data, the same spline positions are used. The spline coefficients are free to vary to account for potential differences between data and simulation.

6.3.4 Extraction of the *CP* observables

To extract the *CP* observables $S_{D^+D^-}$ and $C_{D^+D^-}$, an unbinned maximum likelihood fit to the background-subtracted decay-time distribution of the $B^0 \to D^+D^-$ candidates is performed using the PDF from Eq. (5.12). However, the theoretical model in Eq. (5.1) can be simplified for B^0 decays. The world-average value of the decay-width difference, $\Delta\Gamma_d$, reported by the PDG [27], is compatible with zero and fixed to zero in the fit. This simplifies the theoretical model to

$$\mathcal{B}_{\text{theo}}(t, d') \propto e^{-\Gamma t} \left[1 + d'\, C \cos \Delta m t - d'\, S \sin \Delta m t\right] . \tag{6.12}$$

Consequently, the measurement is not sensitive to the parameter $D_{D^+D^-}$. In Sec. 6.5, a study is performed to evaluate the effect of this assumption.

In the decay-time fit, uncertainties of input parameters are taken into account by Gaussian constraints. The values and uncertainties of the external parameters Δm_d and τ_{B^0} are taken from the PDG [27]. No official Run 2 measurement of the B^0-$\overline{B}^0$ production asymmetry is available. However, in a similar *CP*-violation measurement of $B^0 \to D^{*\pm}D^{\mp}$ decays [112], the production asymmetry was determined. Since the kinematics of this channel are very similar to the $B^0 \to D^+D^-$ channel, the value

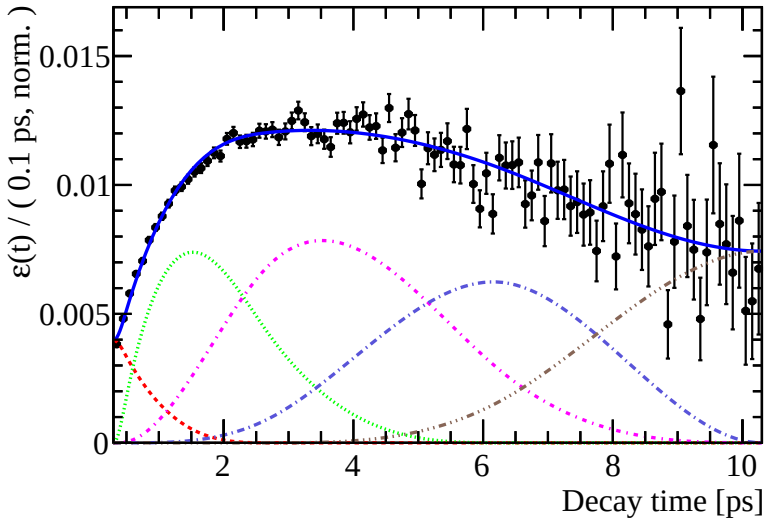

Figure 6.10: Decay-time acceptance of simulated $B^0 \to D^+D^-$ decays. The decay-time distribution, where the effect of the exponential decay is removed, is shown as points, and the PDF projection obtained by the fit is overlaid. The individual B-splines are shown in different colours.

and uncertainty of the production asymmetry are taken from this measurement and no correction is needed. The FT-calibration parameters from Tab. 6.4 are also included via Gaussian constraints. The parameters of the decay-time resolution model are fixed to the values obtained in Sec. 6.3.2. The spline positions of the acceptance model determined in Sec. 6.3.3 are fixed, while the spline coefficients are free to vary. The fit is performed in the decay-time range $0.3 < t < 10.3\,\text{ps}$ and yields the results

$$\begin{aligned} S_{D^+D^-} &= -0.552 \pm 0.100\,, \\ C_{D^+D^-} &= 0.128 \pm 0.103\,, \end{aligned}$$

with the statistical correlation coefficient between the two parameters of 0.472. Otherwise, no significant correlations are observed. The decay-time distribution of background-subtracted $B^0 \to D^+D^-$ data is shown in Fig. 6.11 along with the projection of the PDF. Figure 6.12 shows the decay-time-dependent CP asymmetry. In each decay-time bin, the CP asymmetry is calculated via

$$A^{CP} = -\frac{(\sum_j {}_s\mathcal{P}_j d_j D_j)}{(\sum_j {}_s\mathcal{P}_j D_j^2)}\,, \tag{6.13}$$

with the tagging decision d_j, the tagging dilution D_j and the signal candidate weight ${}_s\mathcal{P}_j$ obtained by the *sPlot* method. The formula is derived in Ref. [55].

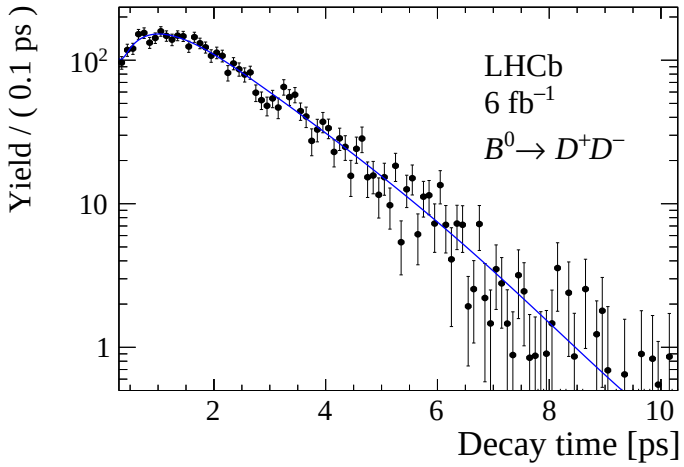

Figure 6.11: Fit to the decay-time distribution of recorded $B^0 \to D^+D^-$ data [24]. The background-subtracted data is shown as points, and the PDF projection is shown as a solid blue line.

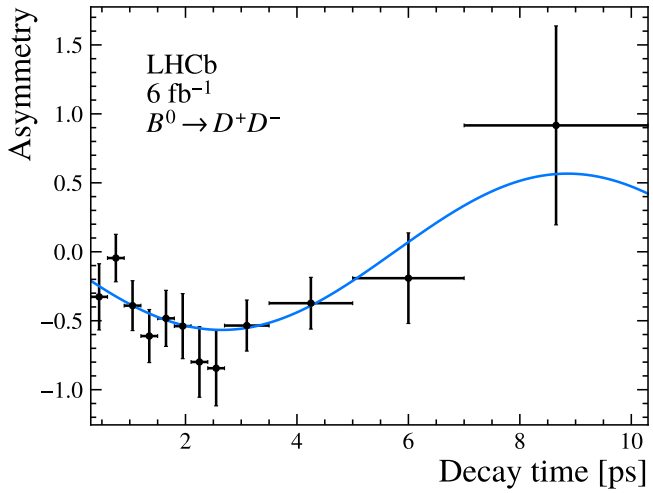

Figure 6.12: Decay-time-dependent *CP* asymmetry of $B^0 \to D^+D^-$ candidates [24]. The asymmetry in data is calculated with Eq. (6.13) and shown as points. The projection of the PDF is overlaid.

6.4 Validation of the fit strategy

Several validation studies are carried out to test the fit strategy and ensure the robustness of the results. In order to avoid experimenter's bias, the following studies have been developed before the values of $S_{D^+D^-}$ and $C_{D^+D^-}$ were examined. Studies that require the values of $S_{D^+D^-}$ and $C_{D^+D^-}$ used the results of the Run 1 analysis in the first iteration. The final results are examined after the cross-checks and systematic studies have been finalised. The procedure is repeated with the measured central values and uncertainties of $S_{D^+D^-}$ and $C_{D^+D^-}$ to obtain the results presented in the following.

The simulation sample is generated taking *CP* violation into account. The generation values of the *CP* observables are known to be

$$\begin{aligned} S_{D^+D^-}^{\text{MC, gen}} &= -0.84\,, \\ C_{D^+D^-}^{\text{MC, gen}} &= \quad 0.00\,. \end{aligned}$$

To validate the fit strategy, the decay-time fit is performed on the simulated sample of $B^0 \to D^+D^-$ decays with the same model as for the recorded data. However, a few adjustments have to be made, such as setting the production asymmetry to zero. Additionally, the FT calibration might differ in simulation and data, the taggers in the simulation sample are calibrated separately. In this case, no control channel is needed. The true mistag is known and can be used to calibrate the estimated mistag. Otherwise, the procedure is the same as for recorded data. The decay-time fit yields the values

$$\begin{aligned} S_{D^+D^-}^{\text{MC,fit}} &= -0.80 \pm 0.11\,, \\ C_{D^+D^-}^{\text{MC,fit}} &= -0.04 \pm 0.11. \end{aligned}$$

The results are consistent with the generation values within one standard deviation.

The FT has a large influence on the fit results, which causes increased uncertainties of the *CP* observables. A second fit is performed where the tags are set to the true tags, removing the effect introduced by the FT. The model behaves as expected, yielding the results

$$\begin{aligned} S_{D^+D^-}^{\text{MC,fit}} &= -0.841 \pm 0.018\,, \\ C_{D^+D^-}^{\text{MC,fit}} &= -0.011 \pm 0.023\,, \end{aligned}$$

which agree with the generation values within the smaller uncertainties.

The stability of the procedure is validated by performing fits to independent subsamples of the recorded data. The data sample is split according to the polarity of the magnet during data taking, the period of data taking and the final state. On each subsample, the mass and decay-time fits are conducted using the nominal models. Additionally, the decay-time fit is performed on the full data sample using only the OS or SS taggers. The results of the *CP* observables are compared with the

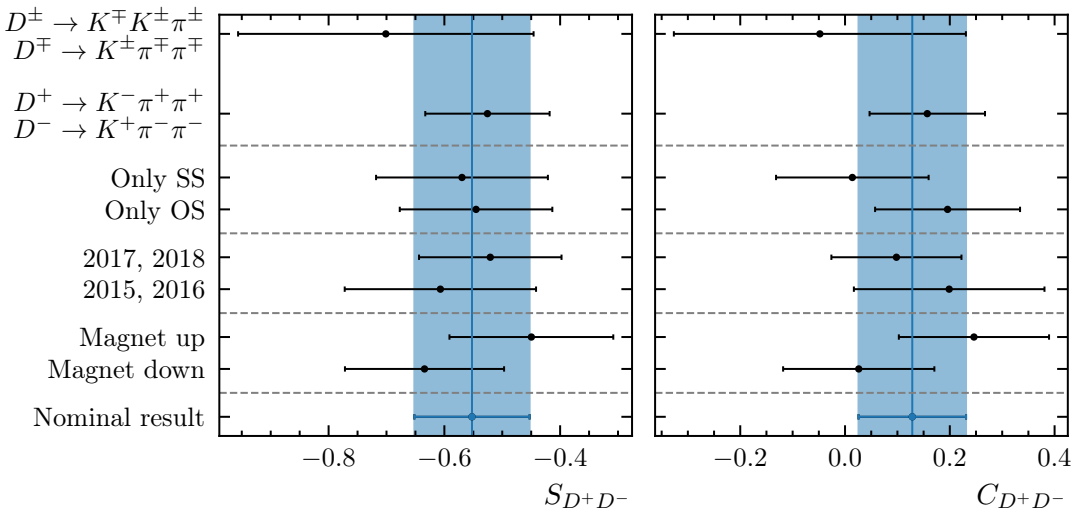

Figure 6.13: Results of the decay-time fit to subsamples of the recorded $B^0 \to D^+D^-$ data for (left) $S_{D^+D^-}$ and (right) $C_{D^+D^-}$. The black points show the results obtained from the subsamples. The results from the entire data sample are shown as blue points, and their uncertainties as blue bands.

values obtained from the entire data sample. The comparison is shown in Fig. 6.13. In all cases, consistent values are found for $S_{D^+D^-}$ and $C_{D^+D^-}$.

The uncertainties of the parameters $S_{D^+D^-}$ and $C_{D^+D^-}$ provided by the decay-time fit are validated using the bootstrap method described in Sec. 4.4. Bootstrap samples are generated by drawing candidates with replacements from the recorded data sample. Mass fits are performed on each of the 1000 samples to determine the background-subtracted decay-time distributions. The decay-time fit is performed, and each value of $S_{D^+D^-}$ and $C_{D^+D^-}$ is stored to obtain the distribution of the residuals with respect to the nominal fit results. The nominal uncertainties provided by the fit are compatible with the standard deviation of the residual distributions and are considered to be accurate.

Finally, the effect of Gaussian constraints is evaluated. To assess the impact of a single parameter uncertainty, a decay-time fit is performed, fixing the parameter to the central value used for the Gaussian constraint. The statistical uncertainties of $S_{D^+D^-}$ and $C_{D^+D^-}$ provided by the fit are subtracted in quadrature from the nominal uncertainties. The external parameters Δm_d, τ_{B^0} and A_{prod} are analysed separately. In contrast, the FT-calibration parameters are fixed simultaneously to obtain a single value to assess the impact of the FT. In Tab. 7.4, the results obtained for the different parameters are presented. The precise knowledge of the external parameters leads to negligible effects on the uncertainties of $S_{D^+D^-}$ and $C_{D^+D^-}$. Although still small compared to the uncertainty caused by the finite size of the data sample, more significant effects are observed for the FT-calibration parameters.

Table 6.7: Impact of the Gaussian constraints on the statistical uncertainty of the measurement of $S_{D^+D^-}$ and $C_{D^+D^-}$.

Gaussian constraint	$S_{D^+D^-}$	$C_{D^+D^-}$
FT calibration	0.015	0.007
A_{prod}	0.004	0.001
Δm_d	0.001	0.002
τ_{B^0}	< 0.001	< 0.001

6.5 Systematic uncertainties

Finally, the systematic uncertainties are evaluated following the strategy described in Sec. 5.2. Most of the systematic uncertainties are determined using pseudoexperiments. The three components, $B^0 \to D^+D^-$ signal, $B_s^0 \to D^+D^-$ background and combinatorial background, are generated separately. This allows for altering the decay-time model for each component individually. First, the mass distributions are generated using the mass PDFs and parameters obtained from the nominal fits described in Sec. 6.2. The number of generated candidates is drawn from a Poisson distribution whose expectation value corresponds to the respective yields of the mass fits. The estimated mistag distributions are generated using histograms of the OS and SS mistag estimates from recorded data. They are weighted by the corresponding component weights of each contribution acquired from the *sPlot* method. The decay-time distribution of the signal component is generated using the decay-time PDF and the parameters obtained from the nominal fit described in Sec. 6.3. The decay-time PDF has to be adjusted for the background components. No *CP* violation or oscillation is assumed for the combinatorial background. The lifetime is set to 0.5 ps, which is determined using the upper-mass sideband of recorded data. The FT-tagging calibration parameters are set to provide random tagging decisions. There is no measurement of time-dependent *CP* violation in $B_s^0 \to D^+D^-$ decays. Therefore, *CP* symmetry is assumed. The oscillation parameters are changed to the respective values of B_s^0 mesons taken from the PDG [27]. The SS-calibration parameters are assumed to provide random tagging decisions because the SS pion and proton taggers are developed for B^0 decays. The OS-calibration parameters are assumed to be the same as for the signal. This is the baseline setup for the following systematic studies. It is adjusted to examine the effects of certain modifications in the model.

Fit bias

At first, the decay-time fit itself is tested for potential biases. A study with 8000 pseudoexperiments is conducted. The number of pseudoexperiments is chosen to be large because a bias in the decay-time fit affects all other systematic studies. Therefore, the precise knowledge of the bias is essential and has to be taken into account if present. The pseudoexperiments are generated without any changes to

the previously described strategy. The nominal mass fits are performed to obtain the background-subtracted decay-time distribution. A decay-time fit is performed in each pseudoexperiment to obtain values for $S_{D^+D^-}$ and $C_{D^+D^-}$. The residual distributions are determined by subtracting the generation values of the parameters from the fit results. The observed standard deviations of the residual distributions are compatible with the statistical uncertainties. No significant bias is observed, and no corrections have to be applied in the following systematic studies.

Mass model

A double-sided Hypatia function is used to model the signal component in the nominal mass fits. To evaluate the impact of this choice a different model is tested. In total, 1000 pseudoexperiments are generated using the sum of two CB functions [115]. The parameters are determined by performing consecutive mass fits to the simulated $B^0 \to D^+D^-$ sample and the recorded data similar to the strategy described in Sec. 6.2. The study yields systematic uncertainties of 0.001 for $S_{D^+D^-}$ and 0.005 for $C_{D^+D^-}$.

Resolution model

The resolution model is determined using simulated $B^0 \to D^+D^-$ decays. No uncertainty is assumed, and the model is fixed in the fit to recorded data. Differences in the resolution between simulation and recorded data are neglected in this approach. This choice stems from the fact that the resolution has a small influence on the measurement of $S_{D^+D^-}$ and $C_{D^+D^-}$ as explained in Sec. 6.3.2. This assumption is tested by generating 1000 pseudoexperiments with an alternative resolution. The widths of the Gaussian components are increased by 10%. As later shown in Sec. 7.5, this is a reasonable assumption. This study yields systematic uncertainties of 0.002 for $S_{D^+D^-}$ and 0.007 for $C_{D^+D^-}$. The effect is in the order of a few per cent of the statistical uncertainties, which confirms the assumption that the impact of the resolution on the measurement is small. No further studies are considered, and these values are assigned as systematic uncertainties.

Decay-width difference

The current world-average value of the decay-width difference, $\Delta\Gamma_d$, is compatible with zero and thus assumed to be zero in the decay-time fit. This assumption removes any influence of the hyperbolic terms in the decay-time PDF from Eq. (5.1). The issue with investigating this effect is that the value of the parameter $D_{D^+D^-}$ is unknown. It cannot be measured due to $\Delta\Gamma_d$ being compatible with zero, but it has to be considered if $\Delta\Gamma_d$ is varied in the following studies. The only assumptions that can be made about the parameter $D_{D^+D^-}$ are given by the normalisation

condition

$$D_{D^+D^-} = \pm\sqrt{1 - S^2_{D^+D^-} - C^2_{D^+D^-}} \approx \pm 0.824\,. \tag{6.14}$$

Therefore, multiple studies have to be performed to test the impact of non-zero values of $\Delta\Gamma_d$ on the measurement of $S_{D^+D^-}$ and $C_{D^+D^-}$. The PDG [27] reports a world-average value of $\Delta\Gamma_d/\Gamma_d = 0.001 \pm 0.010$ and $\tau_{B^0} = 1.519 \pm 0.004\,\text{ps}$ resulting in the uncertainty $\sigma(\Delta\Gamma_d) = 0.007\,\text{ps}^{-1}$. In the generation of the pseudoexperiments the value of $\Delta\Gamma_d$ is shifted by $\pm 1\sigma(\Delta\Gamma_d)$. This yields four combinations with different signs of $\Delta\Gamma_d$ and $D_{D^+D^-}$, which are tested with 1000 pseudoexperiments each. As expected, the observed biases are changing sign depending on the signs of $\Delta\Gamma_d$ and $D_{D^+D^-}$. The largest observed biases of 0.01 for $S_{D^+D^-}$ and 0.005 for $C_{D^+D^-}$ are assigned as systematic uncertainties.

Acceptance model

The decay-time acceptance is free to vary in the decay-time fit. The observed correlations of the spline coefficients with $S_{D^+D^-}$ and $C_{D^+D^-}$ are below 1%. Hence, the effect of changes in the acceptance model is expected to be small. An alternative decay-time fit is performed using a different set of spline positions. As for the nominal model, the spline positions are validated using simulated $B^0 \to D^+D^-$ candidates. The splines at the boundaries of the decay-time range cannot be changed. The alternative set of spline positions is found to be $(0.3, 1.3, 2.2, 6.3, 10.3)\,\text{ps}$. Only small differences between the nominal and alternative decay-time fit results are observed. The differences are assigned as systematic uncertainties resulting in 0.001 for both $S_{D^+D^-}$ and $C_{D^+D^-}$.

Total systematic uncertainty

The systematic uncertainties are summarised in Tab. 6.8. The individual contributions are added in quadrature to obtain the total values. The dominant systematic uncertainty of $S_{D^+D^-}$ is caused by the assumption of $\Delta\Gamma_d$ being zero. This is due to the fact that non-zero values of $\Delta\Gamma_d$ cause contributions of the hyperbolic terms in the decay-time PDF. As the value of $D_{D^+D^-}$ is unknown, the effect has to be estimated conservatively by conducting multiple studies and assigning the largest deviation as the systematic uncertainty. Compared to this uncertainty, the other uncertainties for $S_{D^+D^-}$ are negligible. This is different for $C_{D^+D^-}$, where the contributions are of similar size. However, the total systematic uncertainties of the two parameters are the same. They are roughly 10% of the statistical uncertainties. Comparing the systematic uncertainties of this measurement with those of the previous LHCb measurement [106], a reduction is observed, in particular for $S_{D^+D^-}$. The dominant uncertainty in the previous measurement stems from neglecting components from partially reconstructed decays involving D^* mesons and single-charm B^0 decays in the mass fits. In the Run 2 measurement, the single-charm backgrounds are rejected by the requirements on the charm-meson flight

Table 6.8: Systematic uncertainties of $S_{D^+D^-}$ and $C_{D^+D^-}$. The total systematic uncertainty is the quadratic sum of the individual contributions.

Source	$S_{D^+D^-}$	$C_{D^+D^-}$
$\Delta\Gamma$	0.010	0.005
Decay-time resolution	0.002	0.007
Mass model	0.001	0.005
Acceptance function	0.001	0.001
Total	0.010	0.010

distance. Partially reconstructed decays are suppressed to negligible levels by the lower boundary of the reconstructed B^0-mass range. This is verified using a simulated sample of partially reconstructed $B_s^0 \to D^{*\pm}D^{\mp}$ decays. The second-largest uncertainty in the Run 1 measurement is due to $\Delta\Gamma_d$, which is of similar size as the uncertainty in the Run 2 measurement.

6.6 Results and combination

The fit to the decay-time distribution of recorded $B^0 \to D^+D^-$ signal candidates and the evaluation of the systematic uncertainties yield the final results

$$\begin{aligned} S_{D^+D^-}^{\text{Run 2}} &= -0.552 \pm 0.100\,(\text{stat}) \pm 0.010\,(\text{syst})\,, \\ C_{D^+D^-}^{\text{Run 2}} &= 0.128 \pm 0.103\,(\text{stat}) \pm 0.010\,(\text{syst})\,, \end{aligned}$$

with a statistical correlation coefficient of $\rho(S_{D^+D^-}^{\text{Run 2}}, C_{D^+D^-}^{\text{Run 2}}) = 0.472$. The significance of the measurement is calculated using Wilks' theorem as described in Sec. 4.5. The hypothesis of *CP* symmetry is tested by fixing $S_{D^+D^-}$ and $C_{D^+D^-}$ to zero. Under this assumption, a second decay-time fit is carried out to obtain the negative log-likelihood value of the null hypothesis. The two-dimensional χ^2 is computed by Eq. (4.8) and converted to a significance in terms of standard deviations. The presented measurement excludes *CP* symmetry in $B^0 \to D^+D^-$ decays by more than six standard deviations.

The results of this measurement are combined with the previous LHCb measurement of $S_{D^+D^-}$ and $C_{D^+D^-}$ [106]. An independent data set recorded in the years 2011 and 2012 was used, and the results are given by

$$\begin{aligned} S_{D^+D^-}^{\text{Run 1}} &= -0.54^{+0.17}_{-0.16}\,(\text{stat}) \pm 0.05\,(\text{syst})\,, \\ C_{D^+D^-}^{\text{Run 1}} &= 0.26^{+0.18}_{-0.17}\,(\text{stat}) \pm 0.02\,(\text{syst})\,, \end{aligned}$$

with a statistical correlation coefficient of $\rho(S_{D^+D^-}^{\text{Run 1}}, C_{D^+D^-}^{\text{Run 1}}) = 0.48$. Asymmetric uncertainties introduce complications in the combination procedure. To take this into account, the full likelihood is needed. However, the likelihood is not available for the Run1 measurement, and symmetric uncertainties are determined by taking

the average of the upper and lower uncertainty. This is a reasonable assumption since the asymmetry is small and the likelihoods in the Run 2 measurement do not show any significant asymmetry, while using the same measurement strategy. Another common problem in combinations of these measurements is the treatment of parameters using Gaussian constraints. When both measurements depend on the same parameter, the uncertainties arising from the constraints are correlated. Without full knowledge of the likelihood of both measurements, a combination is not possible. Additionally, updated values of external parameters, *e.g.* Δm_d, could increase the precision of the previous measurement. The effect of the external parameters on the statistical uncertainty is found to be small in the Run 2 measurement. In the Run 1 measurement, statistical and systematic uncertainties of external parameters were evaluated separately. From the systematic studies, the effect of the statistical uncertainties can be estimated. They are found to be negligible. Hence, the statistical uncertainties of the two measurements are assumed to be uncorrelated. The same applies to the systematic uncertainties. Two statistical and systematic correlation matrices are constructed. To perform the combination, they are summed up by the GammaCombo package [117]. A second combination is carried out using only statistical uncertainties to separate the statistical and systematic contributions by taking the difference of the combined and statistical uncertainties in quadrature. The central values are taken from the full combination. The results of the combination are given by

$$\begin{aligned} S^{\text{LHCb}}_{D^+D^-} &= -0.549 \pm 0.085\,(\text{stat}) \pm 0.015\,(\text{syst})\,, \\ C^{\text{LHCb}}_{D^+D^-} &= 0.162 \pm 0.088\,(\text{stat}) \pm 0.009\,(\text{syst}), \end{aligned}$$

with a correlation coefficient of $\rho(S^{\text{LHCb}}_{D^+D^-}, C^{\text{LHCb}}_{D^+D^-}) = 0.474$. Figure 6.14 shows the two-dimensional likelihood scan of the individual results and the combination.

In Fig. 6.15, the previous measurements of (left) $S_{D^+D^-}$ and (right) $C_{D^+D^-}$ by BaBar [107], Belle [108] and LHCb [106] as well as their combination are shown. Although they are in agreement, the Belle measurement is slightly outside the physically allowed region defined by the condition $S^2_{D^+D^-} + C^2_{D^+D^-} \leq 1$. The measurement presented in this thesis confirms the values previously obtained by LHCb and BaBar, shifting the world average further from the Belle measurement. Compared to the previous world average, the total uncertainty of $C_{D^+D^-}$ is about the same, while the uncertainty of $S_{D^+D^-}$ is even smaller. The results are in agreement with SM predictions from a global analysis of $B \to D\overline{D}$ modes [23]. For the first time, *CP* symmetry in $B^0 \to D^+D^-$ decays is excluded by a single measurement with a significance of more than six standard deviations.

The measured central value of $C_{D^+D^-}$ is small, indicating only a small amount of direct *CP* violation in $B^0 \to D^+D^-$ decays. Using Eq. (2.51) the effective phase is calculated to be

$$\sin \phi^{\text{eff}}_{d,D^+D^-} = 0.56 \pm 0.10\,.$$

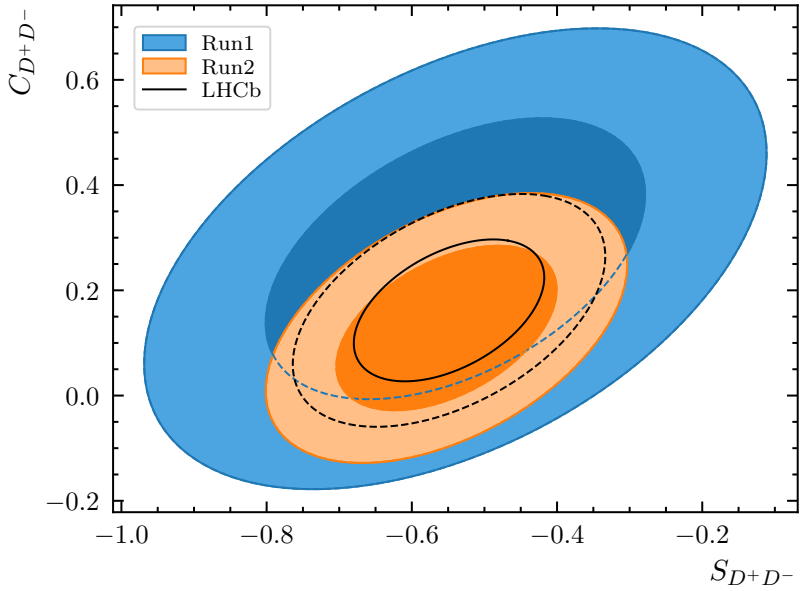

Figure 6.14: Two-dimensional likelihood scans of the *CP* observables $S_{D^+D^-}$ and $C_{D^+D^-}$ for the Run 1 and Run 2 measurements as well as their combination. The inner and outer contours correspond to the 68% and 95% confidence intervals, respectively.

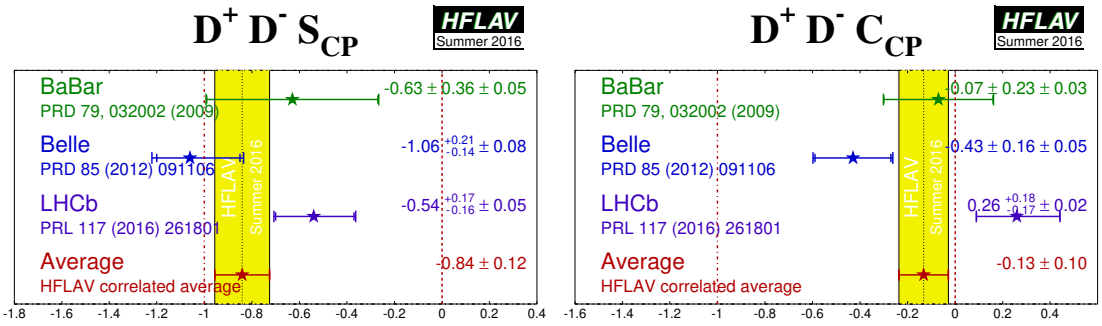

Figure 6.15: Previous measurements of the *CP* observables (left) $S_{D^+D^-}$ and (right) $C_{D^+D^-}$ [28]. The measurements from BaBar [107], Belle [108] and LHCb Run 1 [106] are shown as well as their combination.

The result is combined with the current world-average value of $\sin\phi_d = 0.724 \pm 0.014$ [28] measured in $B^0 \to \psi(nS)K^0_S$ decays to obtain the phase shift

$$\Delta\phi_{d,D^+D^-} = -0.22 \pm 0.12\,\text{rad}\,.$$

This value confirms that higher-order Standard Model contributions are small in $B^0 \to D^+D^-$ decays. The result can be used to constrain these contributions in a global analysis of $B \to D\overline{D}$ decays and separate Standard Model contributions from potential New Physics effects in $B^0_s \to D^+_s D^-_s$ decays.

7 Measurement of CP violation in $B_s^0 \to D_s^+ D_s^-$ decays

In this chapter, the measurement of CP violation in $B_s^0 \to D_s^+ D_s^-$ decays is presented. The analysis is carried out in parallel to the measurement described in Chap. 6 using the same Run 2 data set collected by the LHCb experiment. A concise description of the analysis is given with focus on the differences to the $B^0 \to D^+ D^-$ analysis and a discussion of the results. Previously, a measurement has been performed by the LHCb collaboration with the Run 1 data set [118].

The selection is discussed in Sec. 7.1. In addition to $B_s^0 \to D_s^+ D_s^-$ decays, samples of $B^0 \to D_s^+ D^-$ and $B_s^0 \to D_s^- \pi^+$ decays are selected, which are used for control studies. Sections 7.2 and 7.3 present the mass and decay-time fits, respectively. The fit procedure is validated as discussed in Sec. 7.4 and systematic uncertainties are evaluated in Sec. 7.5. A combination of the results with the previous LHCb measurement is conducted and the individual as well as the combined results are presented in Sec. 7.6.

7.1 Selection

The analysis uses the Run 2 data set of the LHCb experiment recorded at a centre-of-mass energy of 13 TeV and corresponding to an integrated luminosity of $6\,\text{fb}^{-1}$. The $D_s^\pm$ candidates are reconstructed using the three decays $D_s^+ \to K^- K^+ \pi^+$, $D_s^+ \to \pi^- K^+ \pi^+$ and $D_s^+ \to \pi^- \pi^+ \pi^+$. The $D_s^+ \to K^- K^+ \pi^+$ decay has a branching fraction about five times higher than the $D_s^+ \to \pi^- \pi^+ \pi^+$ decay and ten times the branching fraction of the $D_s^+ \to \pi^- K^+ \pi^+$ decay. Candidates in which none of the $D_s^\pm$ mesons decay via $D_s^+ \to K^- K^+ \pi^+$ are not considered because of their minor contribution to the statistical power of the data set. All final-state combinations used in the analysis are summarised in Tab. 7.1.

As for the $B^0 \to D^+ D^-$ analysis, $B^0 \to D_s^+ D^-$ decays are selected in parallel and used for control studies. Either the $D_s^\pm$ or the $D^\pm$ meson is required to decay into the final state with the highest branching fraction leading to the final-state combinations summarised in Tab. 7.1. The selection of this sample is already described in Sec. 6.1. Only a different BDT requirement has to be applied as explained in Sec. 7.1.3. Control studies that require a sample of B_s^0 decays are conducted using $B_s^0 \to D_s^- \pi^+$ decays, where the same $D_s^\pm$ decay modes as for the signal channel are

Table 7.1: Final-state combinations used in the selection of $B_s^0 \to D_s^+ D_s^-$, $B^0 \to D_s^+ D^-$ and $B_s^0 \to D_s^- \pi^+$ decays.

Decay	Final-state decays	
$B_s^0 \to D_s^+ D_s^-$	$D_s^+ \to K^- K^+ \pi^+$	$D_s^- \to K^+ K^- \pi^-$
	$D_s^+ \to K^- K^+ \pi^+$	$D_s^- \to \pi^+ K^- \pi^-$
	$D_s^+ \to K^- K^+ \pi^+$	$D_s^- \to \pi^+ \pi^- \pi^-$
$B^0 \to D_s^+ D^-$	$D_s^+ \to K^- K^+ \pi^+$	$D^- \to K^+ \pi^- \pi^-$
	$D_s^+ \to K^- K^+ \pi^+$	$D^- \to K^+ K^- \pi^-$
	$D_s^+ \to \pi^- K^+ \pi^-$	$D^- \to K^+ \pi^- \pi^-$
	$D_s^+ \to \pi^- \pi^+ \pi^+$	$D^- \to K^+ \pi^- \pi^-$
$B_s^0 \to D_s^- \pi^+$		$D_s^- \to K^+ K^- \pi^-$
		$D_s^- \to \pi^+ K^- \pi^-$
		$D_s^- \to \pi^+ \pi^- \pi^-$

used. To assess resolution and bias effects a sample of prompt $D_s^- \pi^+$ candidates is selected, in which D_s^- mesons and π^+ from the PV are combined. The selection of those candidates is similar to the selection of the $B_s^0 \to D_s^- \pi^+$ sample and is not discussed in detail.

7.1.1 Preselection

The same centralised requirements as described in Sec. 6.1.1 are applied to the $B_s^0 \to D_s^+ D_s^-$ and $B^0 \to D_s^+ D^-$ samples. Due to the different topology, a different stripping line is used for $B_s^0 \to D_s^- \pi^+$ decays. Nevertheless, the requirements are very similar and are not discussed here.

The offline requirements are the same as for the $B^0 \to D^+ D^-$ analysis, namely the D-mass windows are tightened to separate $D^\pm$ and $D_s^\pm$ candidates and a significant D-meson flight distance is required to suppress background from single-charm decays. Approximately 89% of the combinatorial background candidates are rejected by the offline requirements. Due to the flight-distance requirement and the two $D_s^\pm$ mesons in the decay, the signal efficiency of about 61% is lower than for $B^0 \to D^+ D^-$ and $B^0 \to D_s^+ D^-$ decays. Fig. 7.1 shows the effect of the offline requirements on the reconstructed B_s^0-mass distribution of $B_s^0 \to D_s^+ D_s^-$ candidates. The combinatorial background is significantly reduced and a more pronounced peak at the known B_s^0 mass [27] is visible. The same requirements are applied to the $D_s^\pm$ meson of the $B_s^0 \to D_s^- \pi^+$ sample. Additionally, the pion from the B_s^0 decay is required to have a pion ProbNN greater than 0.3 and candidates with associated hits in the muon chambers are rejected. This results in a signal efficiency of about 69%.

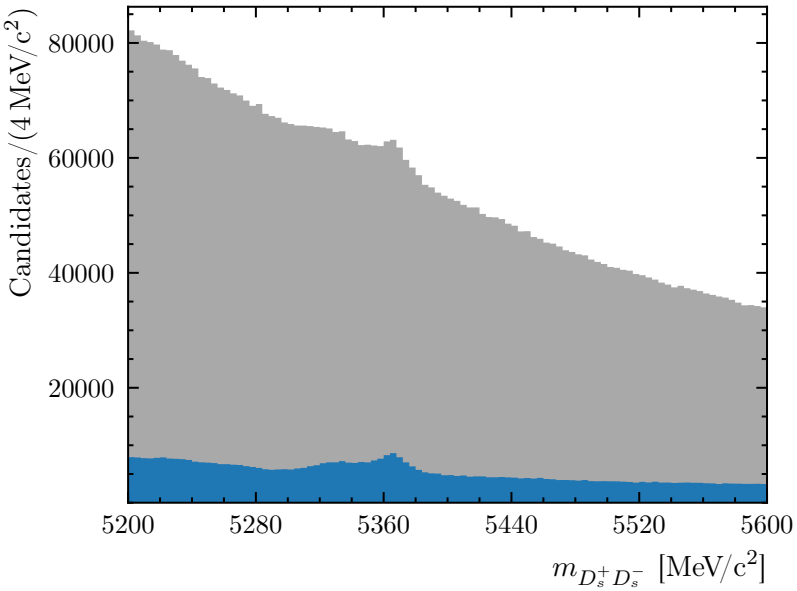

Figure 7.1: Reconstructed B_s^0-mass distribution of $B_s^0 \to D_s^+ D_s^-$ candidates. The blue histogram shows the distribution of the candidates retained after the preselection. The grey area represents the candidates rejected by the offline preselection requirements.

7.1.2 Vetoes

Vetoes are applied to suppress background contributions from decays with misidentified final-state particles. The strategy is the same as described in Sec. 6.1.2. Invariant masses are calculated under consideration of different final-state-particle hypotheses. Requirements on the ProbNN variables defined in Eq. (6.1) are applied within the mass region of the background particles, if present. Due to the different final states of the $D_s^\pm$ and $D^\pm$ mesons, independent vetoes have to be developed for this analysis. The rejected background decays are briefly described in the following. More details about the requirements are provided in Ref. [103].

Vetoes in $D_s^+ \to K^- K^+ \pi^+$ decays: Intermediate $\phi \to K^+ K^-$ decays cause background contributions if a kaon is misidentified as a pion. The $D_s^+ \to K^- \pi^+ K^+$ decays can be identified as signal if the pion and kaon with the same charge are misidentified as each other. Although this is still the same decay, it has to be suppressed because of the wrong reconstruction. Background from $\Lambda_c^+ \to K^- p \pi$ decays can contribute through the misidentification of the proton as a kaon or a double misidentification of the proton as a pion and the pion as a kaon. Finally, $D^0 \to K^+ K^-$ decays without misidentification are rejected by a requirement on the two-body mass of the kaons as the decay $D_s^+ \to D^0 \pi^+$ is impossible.

Vetoes in $D_s^+ \to \pi^- K^+ \pi^+$ decays: Contributions from $\phi \to K^- K^+$ decays arise if either one or both kaons are identified as pions. Backgrounds from D^0 mesons contribute through $D^0 \to \pi^- K^+$, $D^0 \to K^- K^+$ and $D^0 \to K^- \pi^+$ decays, where none, one or both final-state particles are misidentified, respectively. Single and double misidentification causes background contributions from $D^+ \to \pi^+ \pi^- \pi^-$ and $D^+ \to K^- \pi^+ \pi^+$ decays, respectively. Additionally, decays of $D_s^\pm$ mesons from $D_s^+ \to \pi^- \pi^+ K^+$ and $D_s^+ \to K^- \pi^+ K^+$ with double and triple misidentifications are present. Finally, the identification of a proton as a kaon leads to background from $\Lambda_c^+ \to \pi^- p \pi^+$ decays.

Vetoes in $D_s^+ \to \pi^- \pi^+ \pi^+$ decays: In this final state, most of the background contributions stem from D^0 decays. Background from $D^0 \to K^- \pi^+$ decays occurs due to the kaon being identified as a pion. The combination with both pions is considered to develop the veto. A contribution from $D^0 \to \pi^- K^+$ decays, where the kaon is identified as the pion with the higher p_T, is found. Finally, the decay $\Lambda_c^+ \to \pi^- p \pi^+$ can contribute if the proton is misidentified as a pion. Similar to the other final states, $D^0 \to \pi^- \pi^+$ decays without misidentification are removed.

Efficiencies: Approximately 94% of the $B_s^0 \to D_s^+ D_s^-$ signal candidates are retained by the vetoes. For the $B_s^0 \to D_s^- \pi^+$ sample, independent vetoes are developed due to differences in the kinematic distributions. However, only minor changes are necessary leading to similar requirements with an efficiency of about 96%.

Multivariate classification of $D^+ \to K^- \pi^+ \pi^+$ and $D_s^+ \to K^- K^+ \pi^+$ decays

The challenging discrimination between $D_s^+ \to K^- K^+ \pi^+$ and $D^+ \to K^- \pi^+ \pi^+$ decays caused by the kaon-pion misidentification is already discussed in detail in Sec. 6.1.2. Here, the rejection of the background contribution from $D^+ \to K^- \pi^+ \pi^+$ decays in $D_s^+ \to K^- K^+ \pi^+$ decays suffers from the same inefficiency. As only the roles of signal and background are swapped, the previously trained BDT is used to also suppress this background. The requirement on the BDT response is inverted and tightened to reject more than 99% of $D^+ \to K^- \pi^+ \pi^+$ decays in the simulated samples. As shown in the left plot of Fig. 7.2, a large contribution of falsely reconstructed $B^0 \to D_s^+ D^-$ decays is present in the reconstructed B_s^0-mass distribution of $B_s^0 \to D_s^+ D_s^-$ candidates. However, a sufficient suppression, represented by the grey area, is accomplished by the BDT requirement. The right plot of Fig. 7.2 shows the distribution of the invariant $K^\mp \pi^\pm \pi^\pm$ mass before and after applying the BDT requirement. The distribution of the $D_s^\pm$ candidates with higher p_T is shown for better visualisation. About 93% and 87% of $B_s^0 \to D_s^+ D_s^-$ signal candidates are retained depending on whether the BDT requirement has to be applied to one or both $D_s^\pm$ mesons. The same selection is applied to the $D_s^\pm$ mesons of the $B_s^0 \to D_s^- \pi^+$ sample, resulting in an efficiency of about 93%.

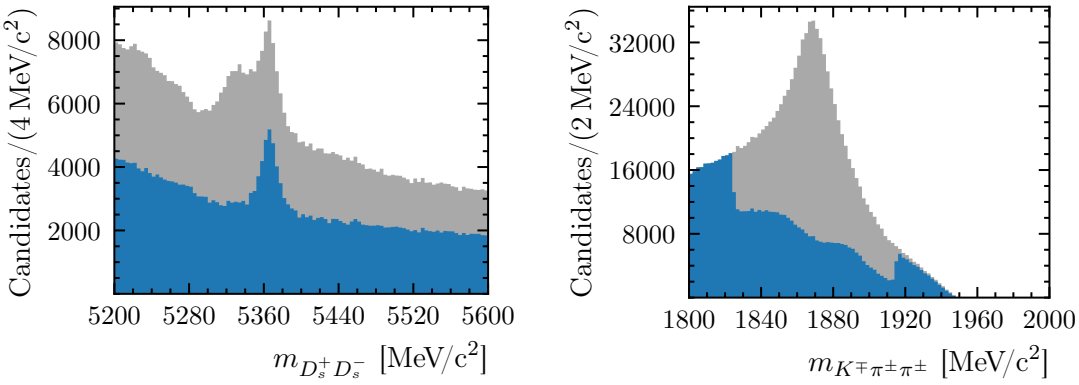

Figure 7.2: The (left) reconstructed B_s^0-mass distribution of $B_s^0 \to D_s^+ D_s^-$ candidates. The blue histogram shows the distribution of the candidates retained after the veto selection. The grey area represents the candidates rejected by the veto requirements. The right plot shows the invariant $K^\mp\pi^\pm\pi^\pm$ mass of the $D_s^\pm$ candidates with the higher p_T. The grey area represents the $D^+ \to K^-\pi^+\pi^+$ contribution rejected by the BDT requirements.

7.1.3 Multivariate selection

The BDT presented in Sec. 6.1.3 is used to suppress the remaining combinatorial background. It can be used without modifications, as the $B_s^0 \to D_s^+ D_s^-$ decays are already included in the training sample. Nevertheless, the optimal requirement on the BDT response has to be determined separately for this analysis. The FOM defined in Eq. (6.2) is used, but the parameters Δm_d and $\sin\phi_d^\mathrm{eff}$, have to be replaced by their respective values for $B_s^0 \to D_s^+ D_s^-$ decays, namely Δm_s and $\sin\phi_{s,D_s^+D_s^-}^\mathrm{eff}$. The values are taken from the PDG [27] and $|\lambda|$ is also assumed to be one. A cut scan is performed for each final state and the results are shown in Fig. 7.3. In contrast to the results of the $B^0 \to D^+ D^-$ analysis, the decay-time resolution has a larger impact on the cut scan. This is expected due to the small oscillation period of the B_s^0 mesons, which is of the same order as the decay-time resolution. For all final states, candidates with a BDT output greater than 0.95 are selected. Approximately 94% of the signal candidates are retained by the BDT requirement, while about 99% of the combinatorial background is rejected. The effect of the BDT requirement on the reconstructed B_s^0-mass distribution of $B_s^0 \to D_s^+ D_s^-$ candidates is shown in Fig. 7.4. The same requirement is applied to the $B^0 \to D_s^+ D^-$ sample, which results in an efficiency of about 93%.

An independent BDT has to be trained for $B_s^0 \to D_s^- \pi^+$ control sample due to the different decay topology. Similar features and the same training procedure is used. To find the optimal requirement on the BDT response, a simplified cut scan is performed. In this scan, the FOM is given by the B_s^0 yield from the mass fits divided by its uncertainty. An efficiency of about 68% is achieved.

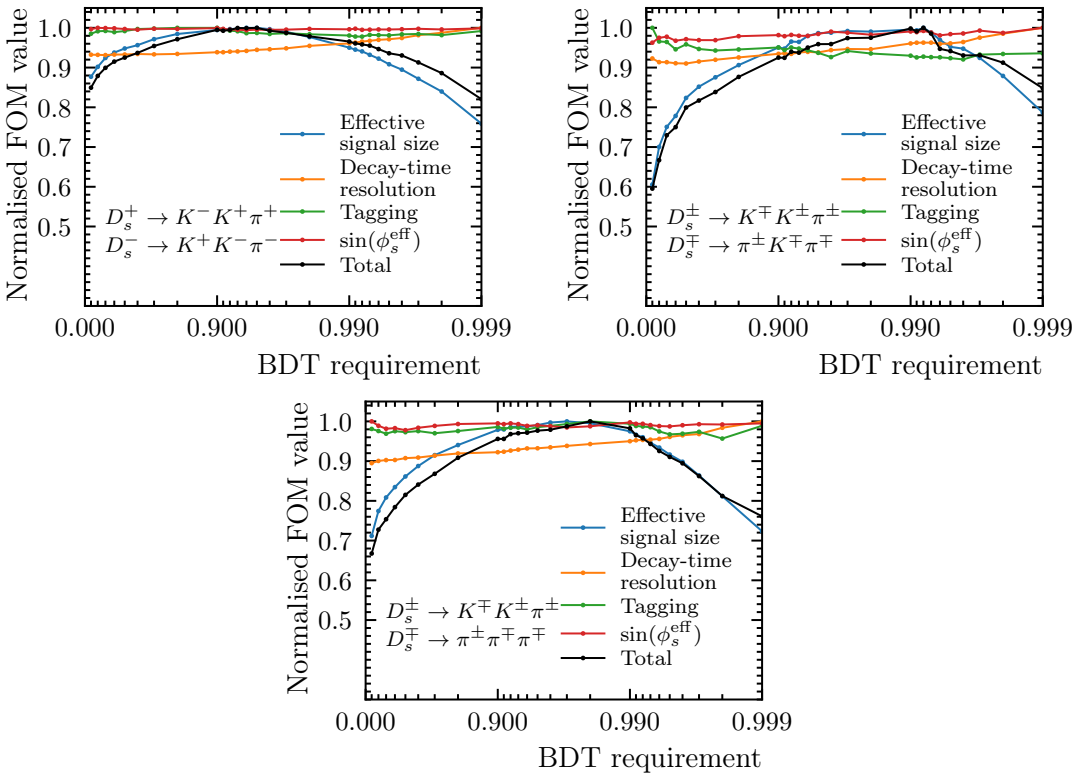

Figure 7.3: Scan of the BDT response using $B_s^0 \to D_s^+ D_s^-$ data for the three different final states. All components are normalised to their maximum value.

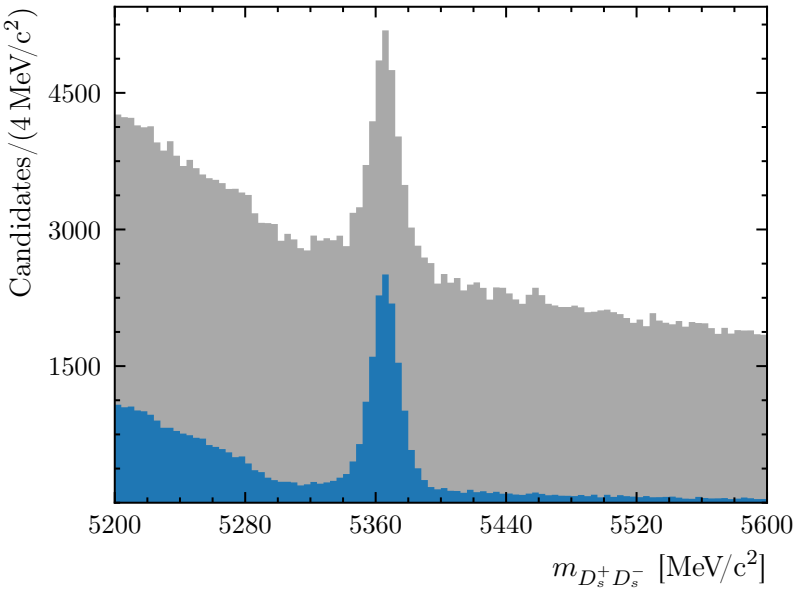

Figure 7.4: Reconstructed B_s^0-mass distribution of $B_s^0 \to D_s^+ D_s^-$ candidates. The blue histogram shows the distribution of the candidates retained after the BDT selection. The grey area represents the candidates rejected by the BDT selection.

7.1.4 Final selection

In preparation for the mass fits the reconstructed B_s^0 mass is restricted to the range 5300–5600 MeV/c^2. The lower boundary is chosen to remove any contributions from partially reconstructed background decays involving $D^{*\pm}$ and $D_s^{*\pm}$ mesons. The upper boundary retains a sufficient amount of combinatorial background candidates for the mass fits. The decay time is restricted to the range 0.3–10.3 ps to avoid any effects from the decay-time requirement of the central preselection. Overall, these requirements have a signal efficiency of about 99%. The same selection is applied to the $B_s^0 \to D_s^- \pi^+$ sample, yielding an efficiency of about 97%. About 1.3–1.7% of events in the $B_s^0 \to D_s^+ D_s^-$ sample and 0.2–1.9% of the events in the $B_s^0 \to D_s^- \pi^+$ sample contain multiple candidates. Only one of the candidates is arbitrarily retained.

7.2 Mass fits

Mass fits are performed to determine the decay-time distribution of signal candidates via the *sPlot* technique. Only two components are considered in the mass model, namely the $B_s^0 \to D_s^+ D_s^-$ signal and combinatorial background components. Partially reconstructed backgrounds are excluded by the lower boundary of the mass range. Another potential background can arise from $B^0 \to D_s^+ D_s^-$ decays.

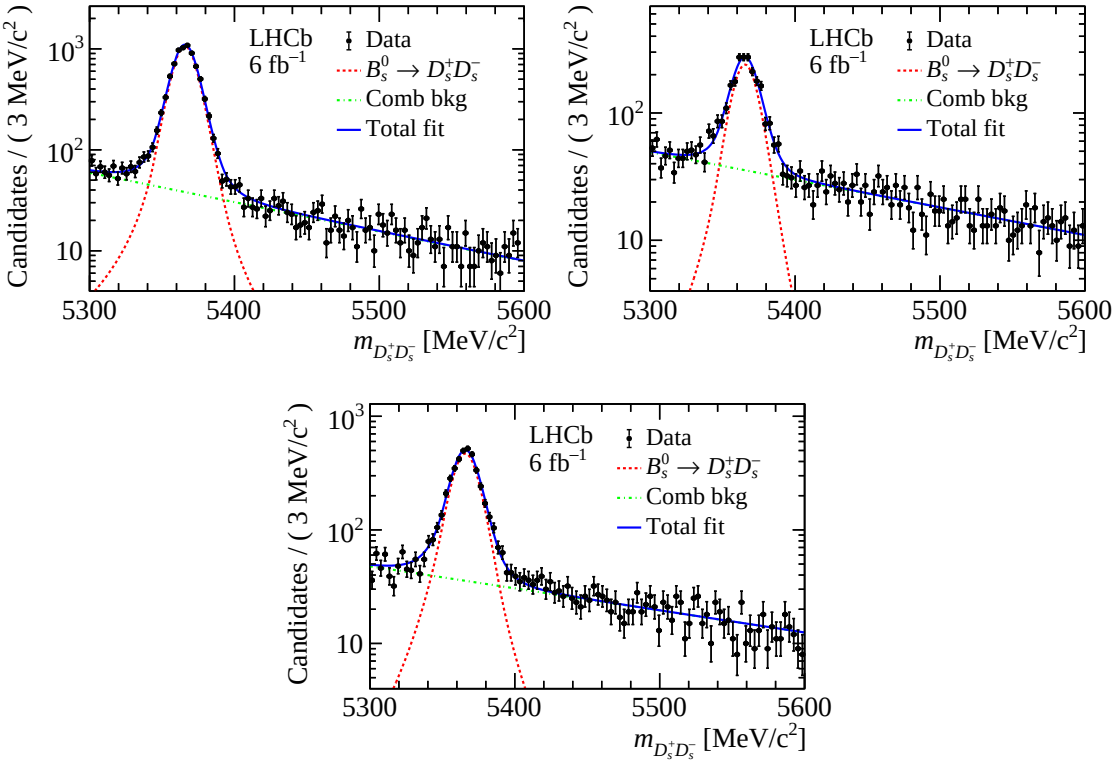

Figure 7.5: Distribution of the reconstructed B_s^0 mass of $B_s^0 \to D_s^+ D_s^-$ candidates and the PDF projections of the fit for the final states, where (left) both $D_s^\pm$ mesons reconstructed via $D_s^+ \to K^- K^+ \pi^+$, (right) only one $D_s^\pm$ meson reconstructed via $D_s^+ \to K^- K^+ \pi^+$ and the other via $D_s^+ \to \pi^- K^+ \pi^+$ and (bottom) one $D_s^\pm$ mesons reconstructed via $D_s^+ \to K^- K^+ \pi^+$ and the other via $D_s^+ \to \pi^- \pi^+ \pi^+$ [24].

However, taking current predictions and the upper limit of the branching fraction into account [23], the contribution in the selected mass range is negligible.

A double-sided Hypatia function is used to model the $B_s^0 \to D_s^+ D_s^-$ signal component. The shape parameters of the Hypatia function are determined by maximum likelihood fits to the reconstructed B_s^0-mass distribution of simulated $B_s^0 \to D_s^+ D_s^-$ candidates. The fits are performed separately for each final state to account for potential kinematic differences. In the fit to recorded data, the parameters of the signal model are fixed to the values obtained from simulation except for the width and mean parameters, which are free to vary. The combinatorial background is parameterised by an exponential function. The slope of this component is free to vary in the fit. As for the simulation fits, the mass fits to recorded data are performed separately for each final state.

The mass fits to the recorded data are presented in Fig. 7.5. Finally, the mass fits yield an overall number of 13313 ± 135 $B_s^0 \to D_s^+ D_s^-$ candidates. The PDFs from

the fits are used to calculate signal weights with the *sPlot* technique, which are used to obtain the background-subtracted decay-time distribution. Similar mass fits are performed for the two control channels. More information on the mass fits is provided in Ref. [103].

7.3 Decay-time fit

A fit to the decay-time distribution is performed to extract the *CP* observables. The fit strategy is similar to the procedure described in Sec. 6.3. In contrast to the $B^0 \to D^+D^-$ analysis, the non-negligible decay-width difference of B_s^0 mesons has to be considered in the analysis of $B_s^0 \to D_s^+D_s^-$ decays. Thus, the hyperbolic terms in Eq. (5.1) contribute to the model introducing an additional observable D. The *CP* observables are measured in terms of $\phi^{\text{eff}}_{s,D_s^+D_s^-}$ and $|\lambda_{D_s^+D_s^-}|$, which is more commonly used in B_s^0 measurements. They are related to the *CP* observables S, C and D according to Eq. (2.31). Applying these modifications to Eq. (5.1) yields

$$\begin{aligned}\mathcal{B}_{\text{theo}}(t, d') \propto e^{-\Gamma t}\Bigg[&\cosh\frac{\Delta\Gamma_s t}{2} - \frac{2|\lambda_{D_s^+D_s^-}|\cos\phi^{\text{eff}}_{s,D_s^+D_s^-}}{1+|\lambda_{D_s^+D_s^-}|^2}\sinh\frac{\Delta\Gamma_s t}{2} \\ &+d'\frac{1-|\lambda_{D_s^+D_s^-}|^2}{1+|\lambda_{D_s^+D_s^-}|^2}\cos\Delta m_s t + d'\frac{2|\lambda_{D_s^+D_s^-}|\sin\phi^{\text{eff}}_{s,D_s^+D_s^-}}{1+|\lambda_{D_s^+D_s^-}|^2}\sin\Delta m_s t\Bigg],\end{aligned} \tag{7.1}$$

where the relation $\phi^{\text{eff}}_{s,D_s^+D_s^-} = -\arg\lambda_{D_s^+D_s^-}$ is used.

The calibration of the FT response is presented in Sec. 7.3.1. The decay-time resolution and acceptance models are determined as described in Sec. 7.3.2 and Sec. 7.3.3, respectively. In Sec. 7.3.4 the extraction of $\phi^{\text{eff}}_{s,D_s^+D_s^-}$ and $|\lambda_{D_s^+D_s^-}|$ with the decay-time fit is discussed. All studies are performed on a merged sample of the analysed final states.

7.3.1 Flavour-tagging calibration

In B_s^0 decays, the SS kaon tagger is used instead of the SS proton and pion taggers due to the s quark in the hadronisation of B_s^0 mesons. The $B_s^0 \to D_s^-\pi^+$ channel is used to calibrate the FT response of the SS kaon tagger. Its high branching fraction provides a sufficiently large calibration sample. However, due to the different decay topology, the kinematic distributions are different from the signal channel. A reweighting is applied to the $B_s^0 \to D_s^-\pi^+$ sample to match the $B_s^0 \to D_s^+D_s^-$ sample in the transverse momentum of the B_s^0 meson, the pseudorapidity, the number of tracks and the number of PVs. A BDT based method is used to perform the reweighting [119]. The linear calibration is performed as described in Sec. 3.4.2. Since only one SS tagger is available, no combination is needed and the calibration of the SS kaon tagger is used in the decay-time fit.

Table 7.2: Results of the FT calibration. The OS calibration is obtained using the $B^0 \to D_s^+ D^-$ data sample and the SS kaon calibration is obtained with the $B_s^0 \to D_s^- \pi^+$ data sample.

	OS Comb.	SS Kaon
p_0	0.0185 ± 0.0034	0.028 ± 0.005
p_1	0.885 ± 0.032	0.88 ± 0.06
Δp_0	0.003 ± 0.005	-0.017 ± 0.006
Δp_1	0.01 ± 0.05	0.17 ± 0.07

Table 7.3: Performance parameters of the FT calibration. The OS calibration is obtained using $B^0 \to D_s^+ D^-$ data and the SS kaon calibration is obtained using $B_s^0 \to D_s^- \pi^+$ data. Both calibrations are applied to $B_s^0 \to D_s^+ D_s^-$ data to measure the performance.

	$\langle \eta \rangle$	ε_{tag} [%]	ε_{eff} [%]
OS Comb.	0.3433	34.81 ± 0.33	3.55 ± 0.06
SS Kaon	0.4124	56.87 ± 0.34	2.34 ± 0.04
OS+SS		70.99 ± 0.31	5.60 ± 0.07

The different hadronisation of the B_s^0 mesons does not affect the OS taggers. Thus, the $B^0 \to D_s^+ D^-$ channel is used to calibrate the FT response of the opposite side. No reweighting is needed in this case due to the similar kinematic distributions of the signal and calibration channel. All available OS taggers described in Sec. 3.4 are used. They are individually calibrated, combined and the combination is calibrated again.

The results of the OS and SS calibrations are presented in Tab. 7.2. The calibrations determined using $B^0 \to D_s^+ D^-$ and $B_s^0 \to D_s^- \pi^+$ decays is applied to the $B_s^0 \to D_s^+ D_s^-$ data. The performance of the calibrated FT is presented in Tab. 7.3. All calibration and combination steps are performed with the EPM tool [88]. A tagging power of $(5.60 \pm 0.07)\%$ is achieved.

7.3.2 Decay-time resolution

In the following, the calibration of the decay-time resolution is briefly discussed. More details are provided in Ref. [103]. The decay-time resolution has a large impact on the measurement of the *CP* observables in B_s^0 decays. The faster oscillation of B_s^0 mesons compared to B^0 mesons leads to a smaller dilution factor in Eq. (6.10). Thus, the knowledge of the decay-time resolution is much more important in B_s^0 measurements. The DTF provides a per-candidate uncertainty on the decay time, δ_t. This can be used in the decay-time fit to accurately model the resolution. However,

the absolute values of the decay-time uncertainty might not be accurate and have to be calibrated to represent the true resolution. A calibration function is determined on a sample of prompt $D_s^-\pi^+$ candidates. The prompt candidates are expected to have a decay time of zero. This can be exploited to measure the resolution because the sample only represents resolution and bias effects. Only the $D_s^+ \to K^-K^+\pi^+$ final state is considered, where the invariant K^-K^+ mass is required to be within $10\,\mathrm{MeV}/c^2$ of the known ϕ mass taken from the PDG [27]. A systematic study is performed to validate the assumption that the resolution from this sample is representative of the signal sample. Events with more than one PV are discarded in the calibration to avoid distortions caused by particles that are assigned to the wrong PV. To ensure a negligible amount of decays of B mesons or other long-lived particles, the positive tail of the decay-time distribution is removed.

The prompt sample is divided into bins of the decay-time uncertainty. In each bin, a fit to the reconstructed $D_s^\pm$ mass is performed to determine the signal weights with the *sPlot* method. A fit to the signal-weighted decay-time distribution is conducted using a model consisting of three Gaussian functions with a common mean parameter and different widths. An effective resolution is calculated with Eq. (6.11), where the mass difference, Δm_d, is replaced by the mass difference of the B_s^0 mesons, Δm_s, taken from the PDG [27]. A linear calibration function is determined according to

$$\sigma(\delta_t) = x_0 + x_1\,\delta_t \tag{7.2}$$

where σ and δ_t are the measured resolution and the average decay-time uncertainty in each bin, respectively, and x_0 and x_1 are the free calibration parameters. They are determined to be $x_0 = 0.0085 \pm 0.0008\,\mathrm{ps}$ and $x_1 = 1.065 \pm 0.025$.

To port the resolution function from the prompt sample to the $B_s^0 \to D_s^+D_s^-$ sample a scale factor is determined using simulated $B_s^0 \to D_s^-\pi^+$ and $B_s^0 \to D_s^+D_s^-$ decays. In simulated samples, the true decay time is known and can be subtracted from the reconstructed decay time to obtain a distribution that represents the resolution. A fit to this distribution in $B_s^0 \to D_s^-\pi^+$ data is performed using a sum of three Gaussian functions. The same model is used for a fit to the simulated $B_s^0 \to D_s^+D_s^-$ sample, where the parameters are fixed and each of the widths is scaled by a common factor that is free to vary. The scale factor is determined to be 1.222 ± 0.011. Accordingly, the final calibration function that is used in the decay-time fit results in

$$\sigma(\delta_t) = 1.222 \cdot (0.0085\,\mathrm{ps} + 1.065\,\delta_t). \tag{7.3}$$

Apart from resolution effects, the prompt sample can be used to check for a potential decay-time bias. In the study presented above, the bias in each bin of the decay-time uncertainty is given by the mean parameter of the resolution function. The largest bias is measured to be $-10.5\,\mathrm{fs}$. In the following decay-time fit, the decay time is assumed to be unbiased. A systematic study is performed to evaluate the impact of this decay-time bias on the measurement of the *CP* observables. This is discussed in Sec. 7.5.

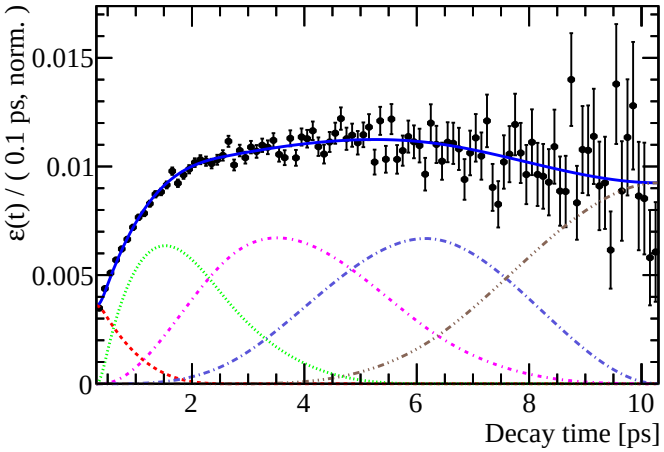

Figure 7.6: Decay-time acceptance of simulated $B_s^0 \to D_s^+ D_s^-$ decays. The decay-time distribution, where the effect of the exponential decay is removed, is shown as points, and the PDF projection obtained by the fit is overlaid. The individual B-splines are shown in different colours.

7.3.3 Decay-time acceptance

The Decay-time-dependent efficiency is taken into account by the acceptance function, which is parameterised using the B-spline model described in Sec. 5.2. The spline positions are found using the sample of simulated $B_s^0 \to D_s^+ D_s^-$ decays. A fit to the decay-time distribution is performed using a simplified model composed of an exponential function, a fixed decay-time resolution and the acceptance function. The exponential function decreases according to the B_s^0-meson lifetime, which is fixed in the fit. The spline positions of the acceptance function are also fixed, and only the spline coefficients are free to vary. It is found that the same spline positions can be used as for the $B^0 \to D^+ D^-$ channel.

Figure 7.6 shows the decay-time distribution of the simulated $B_s^0 \to D_s^+ D_s^-$ candidates, where the effect of the exponential decay is removed. The PDF projections obtained by the fit are overlaid. The acceptance in B_s^0 measurements is usually fixed, because it is correlated with the parameter D. However, it was found that this effect can be neglected when using the parameter formulation in terms of $\phi^{\text{eff}}_{s,D_s^+ D_s^-}$ and $|\lambda_{D_s^+ D_s^-}|$. No significant correlations are observed between these parameters and the spline coefficients in the following decay-time fit. Therefore, the spline positions at $(0.3, 0.5, 2.7, 6.3, 10.3)$ ps are fixed in the fit to the recorded data and the spline coefficients are free to vary to account for differences between the simulated and recorded data.

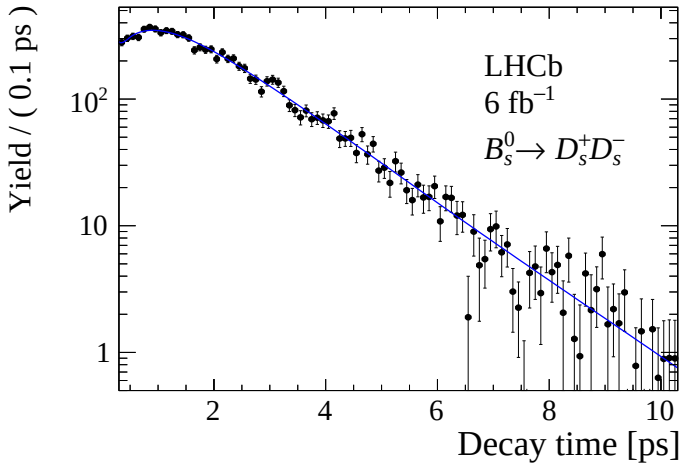

Figure 7.7: Fit to the decay-time distribution of recorded $B_s^0 \to D_s^+ D_s^-$ data [24]. The background-subtracted data is shown as points and the PDF projection obtained by the fit as a solid blue line.

7.3.4 Extraction of the *CP* observables

To extract the *CP* observables $\phi^{\text{eff}}_{s,D_s^+D_s^-}$ and $|\lambda_{D_s^+D_s^-}|$, an unbinned maximum likelihood fit to the background-subtracted decay-time distribution of $B_s^0 \to D_s^+ D_s^-$ candidates is performed. The decay-time distribution is parameterised with the PDF from Eq. (5.12). Uncertainties of input parameters are taken into account by Gaussian constraints. This applies to the external parameters, Δm_s, $\Delta\Gamma_s$ and $\tau_{B_s^0}$, which are taken from the PDG [27], the FT-calibration parameters from Tab. 7.2 and the production asymmetry. No official measurement of the B_s^0-$\overline{B}_s^0$ production asymmetry is available for Run 2 data. The value and uncertainty are taken from Ref. [120], where the production asymmetry is determined using $B_s^0 \to D_s^- \pi^+$ decays.

The decay-time uncertainty is used as an additional variable in the fit. A resolution is applied to each candidate according to the calibration function from Eq. (7.3). The acceptance model uses the spline positions determined in Sec. 6.3.3 and the spline coefficients are free to vary. The fit is performed in the decay-time range 0.3–10.3 ps and yields

$$\begin{aligned} \phi^{\text{eff}}_{s,D_s^+D_s^-} &= -0.086 \pm 0.106\,\text{rad}\,, \\ |\lambda_{D_s^+D_s^-}| &= \quad 1.145 \pm 0.126\,, \end{aligned}$$

with a statistical correlation coefficient of the two parameters of -0.007. Otherwise, no significant correlations are observed. The decay-time distribution of background-subtracted $B_s^0 \to D_s^+ D_s^-$ data is shown in Fig. 7.7 along with the projection of the PDF obtained by the fit. The decay-time-dependent *CP* asymmetry is calculated using Eq. (6.13) and shown in Fig. 7.8.

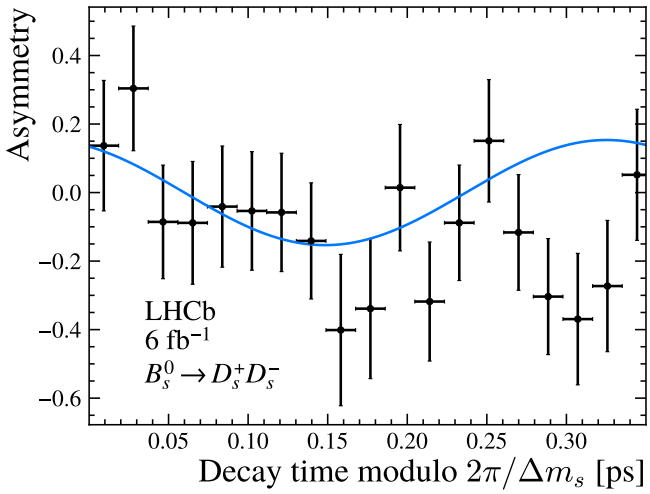

Figure 7.8: Decay-time-dependent CP asymmetry of the $B_s^0 \to D_s^+ D_s^-$ candidates [24]. The asymmetry in data is calculated with Eq. (6.13) and shown as points. The projection of the PDF is overlaid.

7.4 Validation of the fit strategy

The fit framework was developed for the $B^0 \to D^+ D^-$ measurement, and only minor modifications are necessary to adapt it to the $B_s^0 \to D_s^+ D_s^-$ measurement. Nevertheless, additional validation studies are performed with the modified fit procedure.

Decay-time fits to independent subsamples of the data are performed. The data set is split according to the polarity of the magnet during data taking, the period of data taking and the final state. The CP observables are measured in each subsample and the values are compared to the nominal results. Two decay-time fits to the full data set are performed using only the SS kaon tagger and only the OS taggers, respectively. The comparison between the categories is shown in Fig. 7.9. In all cases, consistent results are found within the uncertainties.

The uncertainties on the parameters $\phi^{\text{eff}}_{s,D_s^+ D_s^-}$ and $|\lambda_{D_s^+ D_s^-}|$ provided by the decay-time fit are validated using the bootstrap method described in Sec. 4.4. A total of 1000 bootstrap samples are generated by drawing candidates with replacements from the recorded data sample. The mass and decay-time fits are repeated to obtain the residual distributions of $\phi^{\text{eff}}_{s,D_s^+ D_s^-}$ and $|\lambda_{D_s^+ D_s^-}|$. The observed standard deviations are in agreement with the uncertainties provided by the fit.

In contrast to the $B^0 \to D_s^+ D^-$ control channel, the $B_s^0 \to D_s^- \pi^+$ mode is kinematically different from the $B_s^0 \to D_s^+ D_s^-$ signal channel. These kinematic differences are known to affect the FT. Although the relevant kinematic distributions of the $B_s^0 \to D_s^- \pi^+$ sample are weighted to match the distribution of the $B_s^0 \to D_s^+ D_s^-$ sample, the portability of the FT calibration is not guaranteed. Simulated samples

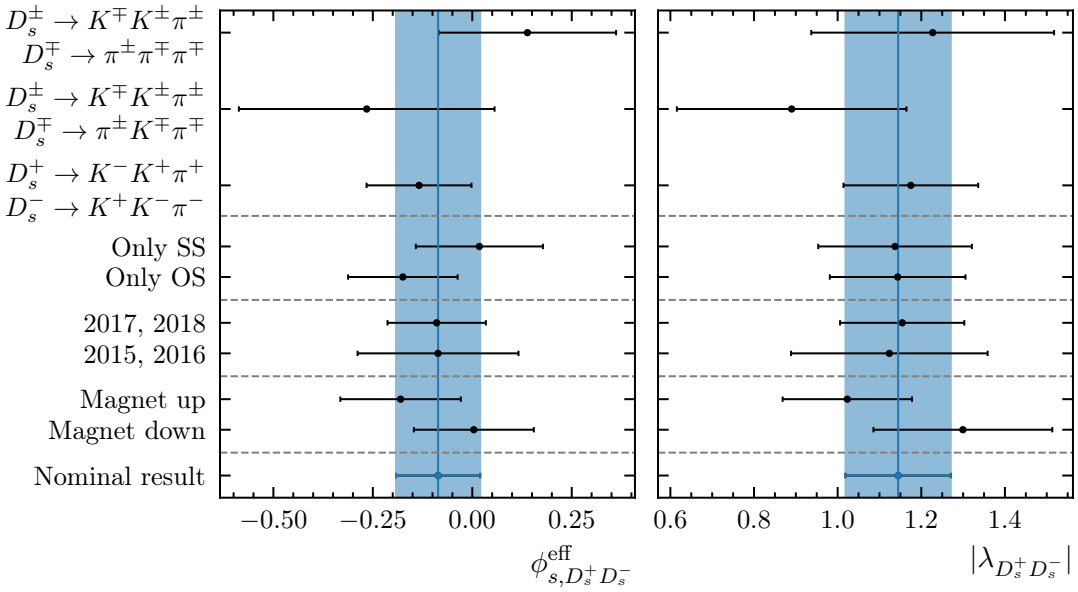

Figure 7.9: Results of the decay-time fit to different subsamples of the recorded $B_s^0 \to D_s^+ D_s^-$ data for (left) $\phi^{\text{eff}}_{s,D_s^+D_s^-}$ and (right) $|\lambda_{D_s^+D_s^-}|$. The black points show the results obtained from the subsamples. The results from the entire data sample are shown as blue points, and their uncertainties as blue bands.

are used for validation. As for the recorded data, the simulated $B_s^0 \to D_s^- \pi^+$ sample is weighted to match the simulated $B_s^0 \to D_s^+ D_s^-$ sample in the transverse momentum of the B_s^0 meson, the pseudorapidity, the number of tracks and the number of PVs. The calibration of the SS kaon tagger is performed on both simulated samples. No significant deviations between the two calibration functions are observed.

The resolution calibration suffers from the same problem. Differences between the resolution of $B_s^0 \to D_s^- \pi^+$ and $B_s^0 \to D_s^+ D_s^-$ decays are taken into account by the scale factor determined in Sec. 7.3.2. However, this does not guarantee the portability of the resolution function itself. As a cross-check, the resolution calibration is performed on simulated $B_s^0 \to D_s^- \pi^+$ and $B_s^0 \to D_s^+ D_s^-$ samples following the strategy explained in Sec. 7.3.2. The two calibration functions are found to be consistent within the statistical uncertainties.

Finally, the impact of the Gaussian constraints is evaluated by performing decay-time fits, where each parameter is independently fixed to its central value. The statistical uncertainties are determined in each case and subtracted in quadrature from the uncertainty of the nominal decay-time fit. The results are shown in Tab. 7.4. Due to their precise knowledge, the contribution of the external parameters is small. The largest effect is caused by the FT calibration, although it is still small compared to the uncertainty due to the finite size of the data sample.

Table 7.4: Impact of the Gaussian constraints on the statistical uncertainty of the measurement of $\phi^{\text{eff}}_{s,D_s^+D_s^-}$ and $|\lambda_{D_s^+D_s^-}|$.

Gaussian constraint	$\phi^{\text{eff}}_{s,D_s^+D_s^-}$ [rad]	$\lvert\lambda_{D_s^+D_s^-}\rvert$
FT calibration	0.013	0.014
A_{prod}	< 0.001	0.002
Δm_s	< 0.001	0.003
$\Delta\Gamma_s$	< 0.001	0.002
$\tau_{B_s^0}$	< 0.001	< 0.001

7.5 Systematic uncertainties

The systematic uncertainties are evaluated as described in Sec. 5.2. Most of the systematic uncertainties are determined using pseudoexperiments. The two components, $B_s^0 \to D_s^+ D_s^-$ signal and combinatorial background, are generated separately. First, the mass distributions are generated according to the model determined in Sec. 7.2. The number of generated candidates is drawn from a Poisson distribution whose expectation value corresponds to the respective yields of the mass fit. The estimated mistag distributions are generated using histograms of the OS combination and SS kaon mistag estimates from recorded data. The per-candidate decay-time uncertainty is similarly generated. The decay-time distribution of the signal component is generated according to the nominal model presented in Sec. 7.3. For combinatorial background, no *CP* violation or oscillation is assumed. The lifetime is set to 0.5 ps, which is determined using the upper-mass sideband of recorded data. The FT-calibration parameters are set to provide random tagging decisions. This is the baseline setup for the following systematic studies. It is adjusted to examine the effects of certain modifications in the model.

Fit bias

A study with 8000 pseudoexperiments is conducted to determine the fit bias. The pseudoexperiments are generated without any changes to the previously described strategy. The nominal mass and decay-time fits are performed to obtain the residual distributions of $\phi^{\text{eff}}_{s,D_s^+D_s^-}$ and $|\lambda_{D_s^+D_s^-}|$. Small biases of -0.002 rad in $\phi^{\text{eff}}_{s,D_s^+D_s^-}$ and 0.008 in $|\lambda_{D_s^+D_s^-}|$ are observed. As they are in the order of 2% and 8% of the respective statistical uncertainties, they are not considered significant. However, the systematic uncertainties in the following studies are corrected by subtracting the fit bias.

Mass model

In the nominal mass fit, a double-sided Hypatia function is used as the signal PDF. To assess the influence of the mass model, 1000 pseudoexperiments are generated

using the sum of two CB functions instead. The parameters are determined by performing consecutive mass fits to the simulated $B_s^0 \to D_s^+ D_s^-$ sample and the recorded data similar to the procedure described in Sec. 7.2. The study yields systematic uncertainties of 0.003 rad for $\phi^{\text{eff}}_{s,D_s^+D_s^-}$ and 0.005 for $|\lambda_{D_s^+D_s^-}|$.

Resolution model

The resolution model is expected to have a significant impact on the measurement and has to be modelled accurately. This is done by calibrating the per-candidate uncertainty of the decay time. The calibration is determined using a control sample that is assumed to be representative for the resolution in the $B_s^0 \to D_s^+ D_s^-$ sample. To validate this assumption and measure the impact of the calibration function on results, pseudoexperiments are generated with a different calibration function. The same prompt sample is used, however, no requirements on the number of PVs and the invariant K^-K^+ mass are applied. A calibration function is determined using the same procedure described in Sec. 7.3.2. This yields the alternative calibration function

$$\sigma(\delta_t) = 1.222 \cdot (0.0085 + 1.248\,\delta_t)\,. \tag{7.4}$$

The resulting resolution is, depending on the decay-time uncertainty, up to 16% larger than the resolution used in the baseline fit. The calibration function is used to generate pseudoexperiments resulting in systematic uncertainties of 0.011 rad for $\phi^{\text{eff}}_{s,D_s^+D_s^-}$ and 0.027 for $|\lambda_{D_s^+D_s^-}|$ are determined.

Decay-time bias

A small decay-time bias is observed in the studies of the prompt sample presented in Sec. 7.3.2. Multiple other decay-time-dependent analyses of Run 2 data confirm this observation [55, 120]. The bias is caused by a misalignment of the VELO. In this analysis, the largest bias is measured to be -10.5 fs. Pseudoexperiments with a fixed decay-time bias of -10.5 fs are generated yielding systematic uncertainties of 0.026 rad for $\phi^{\text{eff}}_{s,D_s^+D_s^-}$ and 0.014 for $|\lambda_{D_s^+D_s^-}|$.

Acceptance model

An alternative decay-time fit is performed using a different set of spline positions for the acceptance model. The spline positions are chosen to be (0.3, 1.3, 2.2, 6.3, 10.3) ps, which is validated on the simulated $B_s^0 \to D_s^+ D_s^-$ sample. Only small differences between the nominal and alternative decay-time fit results are observed and assigned as systematic uncertainties. This difference is 0.001 for $|\lambda_{D_s^+D_s^-}|$ while no significant effect is observed for $\phi^{\text{eff}}_{s,D_s^+D_s^-}$.

Table 7.5: Systematic uncertainties for the measurement of $\phi^{\text{eff}}_{s,D_s^+D_s^-}$ and $|\lambda_{D_s^+D_s^-}|$. The total systematic uncertainty is the quadratic sum of the individual contributions.

Source	$\phi^{\text{eff}}_{s,D_s^+D_s^-}$[rad]	$\lvert\lambda_{D_s^+D_s^-}\rvert$
Decay-time bias	0.026	0.014
Decay-time resolution	0.011	0.027
Mass model	0.003	0.005
Acceptance function	< 0.001	0.001
Total	0.028	0.031

Total systematic uncertainty

The systematic uncertainties are summarised in Tab. 7.5. The total systematic uncertainty is calculated as the quadratic sum of the individual contributions. The dominant contributions are the decay-time bias and the decay-time-resolution model. Both are related to the measurement of the decay time and are expected to have significant impact on the measurement of $\phi^{\text{eff}}_{s,D_s^+D_s^-}$ and $|\lambda_{D_s^+D_s^-}|$. This is caused by the short oscillation period of B_s^0 mesons, which is of the same order as the decay-time resolution. In comparison to the systematic uncertainties of the Run 1 measurement [118] the total systematic uncertainties are slightly larger. This is caused by the decay-time bias, which was not present in the Run 1 data.

7.6 Results and combination

The fit to the decay-time distribution of recorded $B_s^0 \to D_s^+ D_s^-$ candidates and the evaluation of the systematic uncertainties yield the final results

$$\begin{aligned}\phi^{\text{eff,Run 2}}_{s,D_s^+D_s^-} &= -0.086 \pm 0.106\,(\text{stat}) \pm 0.028\,(\text{syst})\,\text{rad}\,,\\ |\lambda|^{\text{Run 2}}_{D_s^+D_s^-} &= \quad 1.145 \pm 0.126\,(\text{stat}) \pm 0.031\,(\text{syst})\,,\end{aligned}$$

with a statistical correlation coefficient of $\rho(\phi^{\text{eff,Run 2}}_{s,D_s^+D_s^-}, |\lambda|^{\text{Run 2}}_{D_s^+D_s^-}) = -0.007$. This result is consistent with CP symmetry in $B_s^0 \to D_s^+ D_s^-$ decays.

The values obtained in this measurement are combined with the previous LHCb measurement of $\phi^{\text{eff}}_{s,D_s^+D_s^-}$ and $|\lambda_{D_s^+D_s^-}|$ [118], which used an independent data set recorded in the years 2011 and 2012 and obtained the results

$$\begin{aligned}\phi^{\text{eff,Run 1}}_{s,D_s^+D_s^-} &= 0.019 \pm 0.174\,(\text{stat}) \pm 0.019\,(\text{syst})\,\text{rad}\,,\\ |\lambda^{\text{Run 1}}_{D_s^+D_s^-}| &= 0.909^{+0.177}_{-0.151}\,(\text{stat}) \pm 0.017\,(\text{syst})\,,\end{aligned}$$

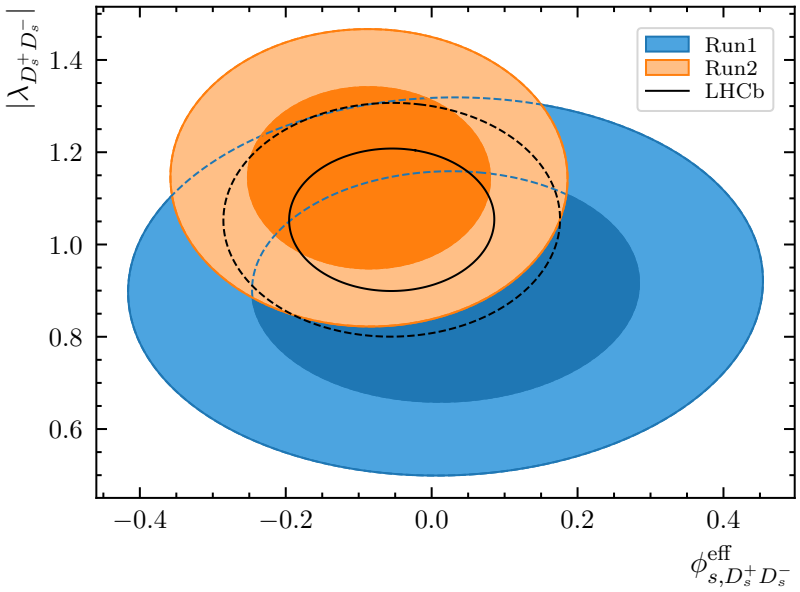

Figure 7.10: Two-dimensional likelihood scans of the *CP* observables $\phi^{\text{eff}}_{s,D_s^+D_s^-}$ and $|\lambda_{D_s^+D_s^-}|$ for the Run 1 and Run 2 measurements as well as their combination. The inner and outer contours correspond to the 68% and 95% confidence intervals, respectively.

with a statistical correlation coefficient of $\rho(\phi^{\text{eff,Run 1}}_{s,D_s^+D_s^-}, |\lambda^{\text{Run 1}}_{D_s^+D_s^-}|) = 0.03$. A combination of the two measurements using the strategy described in Sec. 6.6 yields

$$\begin{aligned}\phi^{\text{eff,LHCb}}_{s,D_s^+D_s^-} &= -0.055 \pm 0.090\,(\text{stat}) \pm 0.021\,(\text{syst})\,\text{rad}\\ |\lambda^{\text{LHCb}}_{D_s^+D_s^-}| &= \quad 1.054 \pm 0.099\,(\text{stat}) \pm 0.020\,(\text{syst}),\end{aligned}$$

with a correlation coefficient of $\rho(\phi^{\text{eff,LHCb}}_{s,D_s^+D_s^-}, |\lambda^{\text{LHCb}}_{D_s^+D_s^-}|) = 0.005$. The two-dimensional likelihood scans of the individual and combined results are shown in Fig. 7.10.

The analysis presented in this thesis represents the most precise single measurement of *CP* violation in $B_s^0 \to D_s^+ D_s^-$ decays to date. The measurement is in agreement with SM predictions [23] and the previous LHCb measurement [118]. At the current level of precision, the measurement of $\phi^{\text{eff}}_{s,D_s^+D_s^-}$ is compatible with the world-average value of $\phi_s = -0.052 \pm 0.013$ [28], obtained from various measurements over multiple decay channels. This combination is dominated by the LHCb measurement in $B_s^0 \to J/\psi\phi$ decays [14], which already entered the region where higher-order contributions have to be considered [121]. In $B_s^0 \to D_s^+ D_s^-$ decays, this can be achieved using the results of the $B^0 \to D^+ D^-$ analysis, which is presented in Chap. 6, and various other *CP*-violation measurements in the $B \to D\overline{D}$ system.

8 Conclusion

The Standard Model of particle physics comprises our current knowledge of the fundamental particles and their interactions. Despite its success, some phenomena, such as the matter-antimatter asymmetry in the universe, remain unexplained. One of the conditions required to produce this asymmetry is the violation of *CP* symmetry, which has been observed in the weak interaction and is, to this day, a subject of intense research. At the LHCb experiment, precision measurements of *CP* violation are performed in decays of b and c hadrons. The *CP* asymmetries may arise from Standard Model processes and New Physics effects. With increasing experimental precision, the control over higher-order effects is a major challenge in most decay modes. The $B \to D\overline{D}$ system offers a unique opportunity to constrain these contributions, which is achieved by performing a global analysis with a variety of branching-fraction and *CP*-violation measurements of U-spin-related decays.

This thesis presents two measurements of *CP* violation in the $B \to D\overline{D}$ system using data recorded by the LHCb experiment in proton-proton collisions at a centre-of-mass energy of 13 TeV [24]. The data set is collected during the years 2015–2018 and corresponds to an integrated luminosity of $6\,\text{fb}^{-1}$. In the measurement of *CP* violation in $B^0 \to D^+D^-$ decays, approximately 5 700 signal candidates are extracted, and the flavour-tagged decay-time-dependent analysis yields the *CP* observables

$$\begin{aligned} S_{D^+D^-}^{\text{Run 2}} &= -0.552 \pm 0.100\,(\text{stat}) \pm 0.010\,(\text{syst})\,, \\ C_{D^+D^-}^{\text{Run 2}} &= 0.128 \pm 0.103\,(\text{stat}) \pm 0.010\,(\text{syst})\,, \end{aligned}$$

with a statistical correlation coefficient of $\rho(S_{D^+D^-}^{\text{Run 2}}, C_{D^+D^-}^{\text{Run 2}}) = 0.472$. This result represents the most precise measurement of *CP* violation in $B^0 \to D^+D^-$ decays to date. In comparison to the previous LHCb measurement [106], the systematic uncertainties are significantly reduced due to the improved suppression of backgrounds from misidentified, single-charm and partially reconstructed decays. Due to the small systematic uncertainties, the measurement is limited by the size of the data set. The total uncertainty of $C_{D^+D^-}$ is in the same order of magnitude as for the previous world average, while the result of $S_{D^+D^-}$ is even more precise [28]. The central values of the *CP* observables are consistent with previous measurements [106–108] and Standard Model predictions [23]. For the first time, *CP* symmetry in $B^0 \to D^+D^-$ decays is excluded by a single measurement with a significance of more than six standard deviations. The results are combined with

the previous LHCb measurement [106] to obtain

$$\begin{aligned} S_{D^+D^-}^{\text{LHCb}} &= -0.549 \pm 0.085\,(\text{stat}) \pm 0.015\,(\text{syst})\,, \\ C_{D^+D^-}^{\text{LHCb}} &= 0.162 \pm 0.088\,(\text{stat}) \pm 0.009\,(\text{syst})\,, \end{aligned}$$

with a correlation coefficient of $\rho(S_{D^+D^-}^{\text{LHCb}}, C_{D^+D^-}^{\text{LHCb}}) = 0.474$. In combination with measurements using $B^0 \to \psi(nS)K_{\text{S}}^0$ decays, the phase shift

$$\Delta\phi_{d,D^+D^-} = -0.22 \pm 0.12\,\text{rad}\,,$$

is calculated, which represents the higher-order Standard Model contributions in $B^0 \to D^+D^-$ decays.

The phase shift determined in the first analysis can be used to constrain similar contributions in the *CP*-violation measurement of $B_s^0 \to D_s^+D_s^-$ decays, which is the second analysis presented in this thesis. In a flavour-tagged decay-time dependent analysis of approximately 13 000 $B_s^0 \to D_s^+D_s^-$ signal candidates, the *CP* observables are measured to be

$$\begin{aligned} \phi_{s,D_s^+D_s^-}^{\text{eff,Run 2}} &= -0.086 \pm 0.106\,(\text{stat}) \pm 0.028\,(\text{syst})\,\text{rad}\,, \\ |\lambda|_{D_s^+D_s^-}^{\text{Run 2}} &= 1.145 \pm 0.126\,(\text{stat}) \pm 0.031\,(\text{syst})\,, \end{aligned}$$

with a statistical correlation coefficient of $\rho(\phi_{s,D_s^+D_s^-}^{\text{eff,Run 2}}, |\lambda|_{D_s^+D_s^-}^{\text{Run 2}}) = -0.007$. This result updates the previous measurement by LHCb [118]. Apart from the LHCb collaboration, no other experiment has been able to perform this analysis. The systematic uncertainties are of the same order of magnitude as for the previous measurement and considerably smaller than the statistical uncertainties. The result is in agreement with the previous measurement and Standard Model predictions [23]. A combination of the two LHCb measurements yields

$$\begin{aligned} \phi_{s,D_s^+D_s^-}^{\text{eff,LHCb}} &= -0.055 \pm 0.090\,(\text{stat}) \pm 0.021\,(\text{syst})\,\text{rad}\,, \\ |\lambda_{D_s^+D_s^-}^{\text{LHCb}}| &= 1.054 \pm 0.099\,(\text{stat}) \pm 0.020\,(\text{syst})\,, \end{aligned}$$

with a correlation coefficient of $\rho(\phi_{s,D_s^+D_s^-}^{\text{eff,LHCb}}, |\lambda_{D_s^+D_s^-}^{\text{LHCb}}|) = 0.005$. These results are consistent with *CP* symmetry in $B_s^0 \to D_s^+D_s^-$ decays.

The framework developed for these measurements can be adapted to conduct further analyses in the $B \to D\overline{D}$ system. With minor modifications to the selection, the current branching fractions of $B_s^0 \to D^+D^-$ [122] as well as $B_s^0 \to D_s^-D^+$ decays [123] can be updated, and current predictions of the branching fraction of $B^0 \to D_s^+D_s^-$ decays indicate that it might be possible to observe the decay with the Run 2 data set [23]. Furthermore, the amount of observed $B_s^0 \to D^+D^-$ decays is sufficient to perform a first measurement of *CP* violation in this decay channel. The wide range of measurements will further improve the control over higher-order effects in these decays.

Due to the statistical limitations of the current measurements, gathering more data is essential to reach a level of precision that might reveal New Physics. In 2022,

the LHCb experiment started recording data with an upgraded detector [124]. In Run 3 of the LHC, the LHCb experiment aims to collect an additional data set corresponding to $50\,\text{fb}^{-1}$. As of today, the experiment has already recorded about $9.5\,\text{fb}^{-1}$ of data in Run 3, which is more than the data sets of Run 1 and Run 2 combined. Apart from the increasing amount of data, measurements in the $B \to D\overline{D}$ system, in particular, profit from the redesign of the LHCb trigger system. In Run 2, hadronic final states suffered from low efficiencies of the hardware trigger, which is replaced by a software-based trigger in Run 3 [125]. First studies confirm that the new trigger system increases the efficiency by at least a factor of two and even more for hadronic final states. Decay-time-dependent analyses significantly benefit from improvements in the flavour tagging due to new tagging algorithms using an inclusive approach [126]. These show promising results, which could further increase the sensitivity of *CP*-violation measurements. Assuming that the strategy remains the same as in the current analyses, the statistical sensitivity of the *CP* observables can be improved to about 0.025 (0.025) for $S_{D^+D^-}$ ($C_{D^+D^-}$) and 0.026 rad (0.031) for $\phi^{\text{eff}}_{s,D_s^+D_s^-}$ ($|\lambda_{D_s^+D_s^-}|$). Additional measurements in B^0 decays are expected by the Belle II experiment [127]. It is scheduled to collect a data set of approximately $50\,\text{ab}^{-1}$ over the next decade, which is about 50 times the amount of data recorded by the Belle experiment. Future measurements by Belle II in $B^0 \to D^+D^-$ decays are expected to be competitive with the foreseen LHCb results. In contrast, LHCb will be the leading experiment in the $B_s^0 \to D_s^+D_s^-$ measurement, as the Belle II experiment can only produce B_s^0 mesons in dedicated runs.

In conclusion, the additional data from both experiments will enable further measurements with unprecedented precision. This makes the control of higher-order effects even more important, which is a great opportunity for future measurements in the $B \to D\overline{D}$ system to contribute to the search for New Physics beyond the Standard Model.

Bibliography

[1] S. L. Glashow, *Partial-symmetries of weak interactions*, Nucl. Phys. **22** (1961) 579.

[2] S. Weinberg, *A Model of Leptons*, Phys. Rev. Lett. **19** (1967) 1264.

[3] A. Salam, *Weak and Electromagnetic Interactions*, Conf. Proc. **C680519** (1968) 367.

[4] ATLAS collaboration, G. Aad *et al.*, *Observation of a new particle in the search for the Standard Model Higgs boson with the ATLAS detector at the LHC*, Phys. Lett. **B716** (2012) 1, arXiv:1207.7214.

[5] CMS collaboration, S. Chatrchyan *et al.*, *Observation of a new boson at a mass of 125 GeV with the CMS experiment at the LHC*, Phys. Lett. **B716** (2012) 30, arXiv:1207.7235.

[6] Super-Kamiokande collaboration, Y. Fukuda *et al.*, *Evidence for Oscillation of Atmospheric Neutrinos*, Phys. Rev. Lett. **81** (1998) 1562, arXiv:9807003.

[7] SNO collaboration, Q. R. Ahmad *et al.*, *Direct Evidence for Neutrino Flavor Transformation from Neutral-Current Interactions in the Sudbury Neutrino Observatory*, Phys. Rev. Lett. **89** (2002) 011301, arXiv:0204008.

[8] N. Aghanim *et al.*, *Planck2018 results: VI. Cosmological parameters*, Astron. Astrophys. **641** (2020) A6.

[9] A. D. Sakharov, *Violation of CP invariance, C asymmetry, and baryon asymmetry of the universe*, Sov. Phys. Usp. **34** (1991) 392.

[10] C. S. Wu *et al.*, *Experimental Test of Parity Conservation in Beta Decay*, Phys. Rev. **105** (1957) 1413.

[11] J. H. Christenson, J. W. Cronin, V. L. Fitch, and R. Turlay, *Evidence for the 2π Decay of the K_2^0 Meson*, Phys. Rev. Lett. **13** (1964) 138.

[12] P. Huet and E. Sather, *Electroweak baryogenesis and standard model CP violation*, Phys. Rev. **D51** (1995) 379, arXiv:hep-ph/9404302.

[13] CKMfitter Group, J. Charles *et al.*, *Current status of the standard model CKM fit and constraints on $\Delta F = 2$ new physics*, Phys. Rev. **D91** (2015) 073007.

[14] LHCb collaboration, R. Aaij *et al.*, *Improved measurement of CP violation parameters in $B_s^0 \to J/\psi K^+K^-$ decays in the vicinity of the $\phi(1020)$ resonance*, Phys. Rev. Lett. **132** (2024) 051802, arXiv:2308.01468.

[15] CDF collaboration, T. Aaltonen *et al.*, *Measurement of the Bottom-Strange Meson Mixing Phase in the Full CDF Data Set*, Phys. Rev. Lett. **109** (2012) 171802, arXiv:1208.2967.

[16] D0 collaboration, V. M. Abazov *et al.*, *Measurement of the CP-violating phase $\phi_s^{J/\psi\phi}$ using the flavor-tagged decay $B_s^0 \to J/\psi\phi$ in 8 fb^{-1} of $p\overline{p}$ collisions*, Phys. Rev. **D85** (2012) 032006, arXiv:1109.3166.

[17] ATLAS collaboration, G. Aad *et al.*, *Measurement of the CP-violating phase ϕ_s in $B_s^0 \to J/\psi\phi$ decays in ATLAS at 13 TeV*, Eur. Phys. J. **C81** (2021) , arXiv:2001.07115.

[18] CMS collaboration, A. M. Sirunyan *et al.*, *Measurement of the CP-violating phase ϕ_s in the $B_s^0 \to J/\psi\phi(1020) \to \mu^+\mu^-K^+K^-$ decay at $\sqrt{s} = 13$ TeV*, Phys. Lett. **B816** (2021) 136188, arXiv:2007.02434.

[19] L. Bel *et al.*, *Anatomy of $B \to D\overline{D}$ decays*, JHEP **07** (2015) 108, arXiv:1505.01361.

[20] R. Fleischer, *Extracting γ from $B_{s(d)} \to J/\psi K_S$ and $B_{d(s)} \to D_{d(s)}^+ D_{d(s)}^-$*, Eur. Phys. J. **C10** (1999) 299, arXiv:hep-ph/9903455.

[21] R. Fleischer, *Exploring CP violation and penguin effects through $B_d^0 \to D^+D^-$ and $B_s^0 \to D_s^+D_s^-$*, Eur. Phys. J. **C51** (2007) 849, arXiv:0705.4421.

[22] M. Jung and S. Schacht, *Standard model predictions and new physics sensitivity in $B \to DD$ decays*, Phys. Rev. **D91** (2015) 034027, arXiv:1410.8396.

[23] J. Davies, M. Jung, and S. Schacht, *$\overline{B} \to \overline{D}D$ decays and the extraction of f_d/f_u at hadron colliders*, JHEP **2024** (2024) 191, arXiv:2311.16952.

[24] LHCb collaboration, R. Aaij *et al.*, *Measurement of CP violation in $B^0 \to D^+D^-$ and $B_s^0 \to D_s^+D_s^-$ decays*, JHEP **01** (2025) 061, arXiv:2409.03009.

[25] D. Griffiths, *Introduction to Elementary Particles*, John Wiley & Sons, New York, USA, 1987.

[26] M. E. Peskin and D. V. Schroeder, *An Introduction to Quantum Field Theory*, Westview Press, 1995.

[27] Particle Data Group, R. L. Workman *et al.*, *Review of particle physics*, Prog. Theor. Exp. Phys. **2022** (2022) 083C01.

[28] Y. Amhis *et al.*, *Averages of b-hadron, c-hadron, and τ-lepton properties as of 2021*, Phys. Rev. **D107** (2023) 052008, arXiv:2206.07501, updated results and plots available at https://hflav.web.cern.ch.

[29] BaBar collaboration, D. Boutigny *et al.*, *The BABAR physics book: Physics at an asymmetric B factory*, 1998.

[30] K. Anikeev *et al.*, *B physics at the tevatron: Run ii and beyond*, 2002.

[31] I. I. Bigi and A. I. Sanda, *CP Violation*, Cambridge University Press, 2nd ed., 2009.

[32] G. C. Branco, L. Lavoura, and J. P. Silva, *CP Violation*, vol. 103, 1999.

[33] Particle Data Group, N. S. *et al.*, *Review of particle physics*, to be published in Phys. Rev **D110** (2024) 030001.

[34] K. G. Wilson, *Confinement of quarks*, Phys. Rev. **D10** (1974) 2445.

[35] Belle Collaboration, S.-K. Choi *et al.*, *Observation of a narrow charmonium-like state in exclusive $B^{\pm} \to K^{\pm}\pi^{+}\pi^{-}j/\psi$ decays*, Phys. Rev. Lett. **91** (2003) 262001.

[36] LHCb collaboration, R. Aaij *et al.*, *Observation of exotic $J/\psi\phi$ structures from amplitude analysis of $B^{+} \to J/\psi\phi K^{+}$ decays*, Phys. Rev. Lett. **118** (2017) 022003, arXiv:1606.07895.

[37] LHCb collaboration, R. Aaij *et al.*, *Observation of structure in the J/ψ-pair mass spectrum*, Science Bulletin **65** (2020) 1983, arXiv:2006.16957.

[38] LHCb collaboration, R. Aaij *et al.*, *Observation of $J/\psi p$ resonances consistent with pentaquark states in $\Lambda_b^0 \to J/\psi p K^{-}$ decays*, Phys. Rev. Lett. **115** (2015) 072001, arXiv:1507.03414.

[39] LHCb collaboration, R. Aaij *et al.*, *Amplitude analysis of $B^{+} \to J/\psi\phi K^{+}$ decays*, Phys. Rev. **D95** (2017) 012002, arXiv:1606.07898.

[40] F. Englert and R. Brout, *Broken Symmetry and the Mass of Gauge Vector Mesons*, Phys. Rev. Lett. **13** (1964) 321.

[41] P. W. Higgs, *Broken Symmetries and the Masses of Gauge Bosons*, Phys. Rev. Lett. **13** (1964) 508.

[42] E. Noether, *Invariante Variationsprobleme*, Nachrichten von der Gesellschaft der Wissenschaften zu Göttingen, Mathematisch-Physikalische Klasse **1918** (1918) 235.

[43] G. Lüders, *On the Equivalence of Invariance under Time Reversal and under Particle-Antiparticle Conjugation for Relativistic Field Theories*, Kong. Dan. Vid. Sel. Mat. Fys. Med. **28N5** (1954) 1.

[44] G. Lüders, *Proof of the TCP theorem*, Ann. Phys. **2** (1957) 1.

[45] BaBar Collaboration, B. Aubert *et al.*, *Observation of CP Violation in the B^0 Meson System*, Phys. Rev. Lett. **87** (2001) 091801, arXiv:hep-ex/0107013.

[46] Belle Collaboration, K. Abe *et al.*, *Observation of Large CP Violation in the Neutral B Meson System*, Phys. Rev. Lett. **87** (2001) 091802, arXiv:hep-ex/0107061.

[47] LHCb collaboration, R. Aaij *et al.*, *First observation of CP violation in the decays of B_s^0 mesons*, Phys. Rev. Lett. **110** (2013) 221601, arXiv:1304.6173.

[48] LHCb collaboration, R. Aaij *et al.*, *Observation of CP violation in charm decays*, Phys. Rev. Lett. **122** (2019) 211803, arXiv:1903.08726.

[49] L.-L. Chau and W.-Y. Keung, *Comments on the Parametrization of the Kobayashi-Maskawa Matrix*, Phys. Rev. Lett. **53** (1984) 1802.

[50] L. Wolfenstein, *Parametrization of the Kobayashi-Maskawa Matrix*, Phys. Rev. Lett. **51** (1983) 1945.

[51] C. Jarlskog, *Commutator of the Quark Mass Matrices in the Standard Electroweak Model and a Measure of Maximal* CP *Nonconservation*, Phys. Rev. Lett. **55** (1985) 1039.

[52] CKMfitter group, J. Charles *et al.*, *CP violation and the CKM matrix: Assessing the impact of the asymmetric B factories*, Eur. Phys. J. **C41** (2005) 1, arXiv:hep-ph/0406184, updated results and plots available at http://ckmfitter.in2p3.fr/.

[53] LHCb collaboration, R. Aaij *et al.*, *Measurement of the semileptonic CP asymmetry in B^0–$\overline{B}^0$ mixing*, Phys. Rev. Lett. **114** (2015) 041601, arXiv:1409.8586.

[54] A. J. Buras, W. Slominski, and H. Steger, *B^0-B^0 mixing, CP violation and the B-meson decay*, Nucl. Phys. **B245** (1984) 369.

[55] LHCb collaboration, R. Aaij *et al.*, *Measurement of CP violation in $B^0 \to \psi(\to \ell^+\ell^-)K^0_S(\to \pi^+\pi^-)$ decays*, Phys. Rev. Lett. **132** (2024) 021801, arXiv:2309.09728.

[56] L. Evans and P. Bryant, *LHC Machine*, JINST **3** (2008) S08001.

[57] LHCb collaboration, R. Aaij *et al.*, *LHCb detector performance*, Int. J. Mod. Phys. **A30** (2015) 1530022, arXiv:1412.6352.

[58] LHCb collaboration, A. A. Alves Jr. *et al.*, *The LHCb Detector at the LHC*, JINST **3** (2008) S08005.

[59] C. Lefèvre, *The CERN accelerator complex. Complexe des accélérateurs du CERN*, https://cds.cern.ch/record/1260465, 2008.

[60] ALICE collaboration, K. Aamodt *et al.*, *The ALICE experiment at the CERN LHC*, JINST **3** (2008) S08002.

[61] ATLAS collaboration, G Aad and others, *The ATLAS Experiment at the CERN Large Hadron Collider*, JINST **3** (2008) S08003.

[62] CMS collaboration, S. Chatrchyan *et al.*, *The CMS experiment at the CERN LHC*, JINST **3** (2008) S08004.

[63] R. Alemany-Fernandez, F. Follin, and R. Jacobsson, *The LHCB Online Luminosity Control and Monitoring*, , `https://cds.cern.ch/record/1567250`.

[64] C. Ilgner *et al.*, *The Beam Conditions Monitor of the LHCb Experiment*, `arXiv:1001.2487`.

[65] R. Aaij *et al.*, *Performance of the LHCb Vertex Locator*, JINST **9** (2014) P09007, `arXiv:1405.7808`.

[66] P. d'Argent *et al.*, *Improved performance of the LHCb Outer Tracker in LHC Run 2*, JINST **12** (2017) P11016, `arXiv:1708.00819`.

[67] M. Adinolfi *et al.*, *Performance of the LHCb RICH detector at the LHC*, Eur. Phys. J. **C73** (2013) 2431, `arXiv:1211.6759`.

[68] A. A. Alves Jr. *et al.*, *Performance of the LHCb muon system*, JINST **8** (2013) P02022, `arXiv:1211.1346`.

[69] *LHCb Starterkit Lessons*, 2015. `https://lhcb.github.io/starterkit-lessons/first-analysis-steps/dataflow.html`.

[70] G. Barrand *et al.*, *GAUDI — A software architecture and framework for building HEP data processing applications*, Comp. Phys. Comm. **140** (2001) 45.

[71] R. Aaij *et al.*, *The Moore project*, `https://lhcbdoc.web.cern.ch/lhcbdoc/moore`.

[72] R. Aaij *et al.*, *The Brunel project*, `https://lhcbdoc.web.cern.ch/lhcbdoc/brunel`.

[73] R. E. Kalman, *A New Approach to Linear Filtering and Prediction Problems*, Journal of Basic Engineering **82** (1960) 35.

[74] R. Aaij *et al.*, *The DaVinci project*, `https://lhcbdoc.web.cern.ch/lhcbdoc/davinci`.

[75] W. D. Hulsbergen, *Decay chain fitting with a Kalman filter*, Nucl. Instrum. Meth. **A552** (2005) 566, `arXiv:physics/0503191`.

[76] M. Clemencic *et al.*, *The LHCb simulation application, Gauss: Design, evolution and experience*, J. Phys. Conf. Ser. **331** (2011) 032023.

[77] T. Sjöstrand, S. Mrenna, and P. Skands, *A brief introduction to PYTHIA 8.1*, Comput. Phys. Commun. **178** (2008) 852, arXiv:0710.3820; T. Sjöstrand, S. Mrenna, and P. Skands, *PYTHIA 6.4 physics and manual*, JHEP **05** (2006) 026, arXiv:hep-ph/0603175.

[78] D. J. Lange, *The EvtGen particle decay simulation package*, Nucl. Instrum. Meth. **A462** (2001) 152.

[79] N. Davidson, T. Przedzinski, and Z. Was, *PHOTOS interface in C++: Technical and physics documentation*, Comp. Phys. Comm. **199** (2016) 86, arXiv:1011.0937.

[80] Geant4 collaboration, J. Allison *et al.*, *Geant4 developments and applications*, IEEE Trans. Nucl. Sci. **53** (2006) 270; Geant4 collaboration, S. Agostinelli *et al.*, *Geant4: A simulation toolkit*, Nucl. Instrum. Meth. **A506** (2003) 250.

[81] R. Aaij *et al.*, *The* Boole *project*, https://lhcbdoc.web.cern.ch/lhcbdoc/boole.

[82] D. Müller, M. Clemencic, G. Corti, and M. Gersabeck, *ReDecay: A novel approach to speed up the simulation at LHCb*, Eur. Phys. J. **C78** (2018) 1009, arXiv:1810.10362.

[83] R. Aaij *et al.*, *Selection and processing of calibration samples to measure the particle identification performance of the LHCb experiment in Run 2*, Eur. Phys. J. Tech. Instr. **6** (2019) 1, arXiv:1803.00824.

[84] J. T. Wishahi, *Measurement of CP violation in $B^0 \to J/\psi K^0_S$ decays with the LHCb experiment*, PhD thesis, TU Dortmund University, 2014, doi: 10.17877/DE290R-13417.

[85] LHCb collaboration, R. Aaij *et al.*, *Opposite-side flavour tagging of B mesons at the LHCb experiment*, Eur. Phys. J. **C72** (2012) 2022, arXiv:1202.4979.

[86] LHCb collaboration, R. Aaij *et al.*, *B flavour tagging using charm decays at the LHCb experiment*, JINST **10** (2015) P10005, arXiv:1507.07892.

[87] LHCb collaboration, R. Aaij *et al.*, *New algorithms for identifying the flavour of B^0 mesons using pions and protons*, Eur. Phys. J. **C77** (2017) 238, arXiv:1610.06019.

[88] J. Wimberley *et al.*, *Espresso Performance Monitor*, https://gitlab.cern.ch/lhcb-ft/EspressoPerformanceMonitor.

[89] L. Breiman, J. H. Friedman, R. A. Olshen, and C. J. Stone, *Classification and regression trees*, Wadsworth international group, 1984.

[90] B. P. Roe *et al.*, *Boosted decision trees as an alternative to artificial neural networks for particle identification*, Nucl. Instrum. Meth. **543** (2005) 577–584, arXiv:physics/0408124.

[91] J. H. Friedman, *Greedy function approximation: A gradient boosting machine.*, Ann. Statist. **29** (2001) 1189 .

[92] A. Blum, A. Kalai, and J. Langford, *Beating the hold-out: bounds for K-fold and progressive cross-validation*, in *Proceedings of the Twelfth Annual Conference on Computational Learning Theory*, COLT '99, 203–208, Association for Computing Machinery, 1999.

[93] T. Chen and C. Guestrin, *XGBoost: A Scalable Tree Boosting System*, in *Proceedings of the 22nd ACM SIGKDD International Conference on Knowledge Discovery and Data Mining*, KDD '16, ACM, 2016, arXiv:1603.02754.

[94] R. Barlow, *Extended maximum likelihood*, Nucl. Instrum. Meth. **A297** (1990) 496.

[95] R. Brun and F. Rademakers, *ROOT — An object oriented data analysis framework*, Nucl. Instrum. Meth. **A389** (1997) 81.

[96] F. James and M. Roos, *Minuit - a system for function minimization and analysis of the parameter errors and correlations*, Comp. Phys. Comm. **10** (1975) 343.

[97] M. Pivk and F. R. Le Diberder, *sPlot: A statistical tool to unfold data distributions*, Nucl. Instrum. Meth. **A555** (2005) 356, arXiv:physics/0402083.

[98] C. Langenbruch, *Parameter uncertainties in weighted unbinned maximum likelihood fits*, Eur. Phys. J. **C82** (2022) , arXiv:1911.01303.

[99] B. Efron, *Bootstrap Methods: Another Look at the Jackknife*, Ann. Statist. **7** (1979) 1.

[100] S. S. Wilks, *The large-sample distribution of the likelihood ratio for testing composite hypotheses*, Ann. Math. Stat. **9** (1938) 60.

[101] A. Kordt, *Flavour Tagging Studien für eine Messung von CP-Verletzung im Zerfall $B_s^0 \to D_s^+ D_s^-$ mit Daten des LHCb-Experiments*, Bachelor's thesis, TU Dortmund University, 2020.

[102] P. Ibis, *Measurements of CP violation in $B^0 \to D\overline{D}$ decays at the LHCb experiment*, PhD thesis, TU Dortmund University, 2022, doi: 10.17877/DE290R-20349.

[103] A. Mödden, *Measurements of Decays in the $B \to D\overline{D}$ Family at the LHCb Experiment*, PhD thesis, TU Dortmund University, 2022, doi: 10.17877/DE290R-22907.

[104] LHCb collaboration, R. Aaij *et al.*, *Measurements of the B^+, B^0, B_s^0 meson and Λ_b^0 baryon lifetimes*, JHEP **04** (2014) 114, arXiv:1402.2554.

[105] T. M. Karbach, G. Raven, and M. Schiller, *Decay time integrals in neutral meson mixing and their efficient evaluation*, arXiv:1407.0748.

[106] LHCb collaboration, R. Aaij *et al.*, *Measurement of CP violation in $B \to D^+D^-$ decays*, Phys. Rev. Lett. **117** (2016) 261801, arXiv:1608.06620.

[107] BaBar collaboration, B. Aubert *et al.*, *Measurements of time-dependent CP asymmetries in $B^0 \to D^{(*)+}D^{(*)-}$ decays*, Phys. Rev. **D79** (2009) 032002, arXiv:0808.1866.

[108] Belle collaboration, M. Röhrken *et al.*, *Measurements of branching fractions and time-dependent CP violating asymmetries in $B^0 \to D^{(*)\pm}D^{\mp}$ decays*, Phys. Rev. **D85** (2012) 091106, arXiv:1203.6647.

[109] M. De Cian, S. Farry, P. Seyfert, and S. Stahl, *Fast neural-net based fake track rejection in the LHCb reconstruction*, LHCb-PUB-2017-011, 2017.

[110] Y. Xie, *Principles to optimize event selections for measurements of CP asymmetries*, LHCb-INT-2009-012, 2009.

[111] LHCb collaboration, R. Aaij *et al.*, *Measurement of the CP violating phase and decay-width difference in $B_s^0 \to \psi(2S)\phi$ decays*, Phys. Lett. **B762** (2016) 253, arXiv:1608.04855.

[112] LHCb collaboration, R. Aaij *et al.*, *Measurement of CP violation in $B^0 \to D^{*\pm}D^{\mp}$ decays*, JHEP **03** (2020) 147, arXiv:1912.03723.

[113] G. A. Cowan, D. C. Craik, and M. D. Needham, *RapidSim: an application for the fast simulation of heavy-quark hadron decays*, Comput. Phys. Commun. **214** (2017) 239, arXiv:1612.07489.

[114] D. Martínez Santos and F. Dupertuis, *Mass distributions marginalized over per-event errors*, Nucl. Instrum. Meth. **A764** (2014) 150, arXiv:1312.5000.

[115] T. Skwarnicki, *A study of the radiative cascade transitions between the Upsilon-prime and Upsilon resonances*, PhD thesis, Institute of Nuclear Physics, Krakow, 1986, DESY-F31-86-02.

[116] H.-G. Moser and A. Roussarie, *Mathematical methods for $B^0\overline{B}^0$ oscillation analyses*, Nucl. Instrum. Meth. **A384** (1997) 491.

[117] M. Kenzie *et al.*, *GammaCombo: A statistical analysis framework for combining measurements, fitting datasets and producing confidence intervals*, doi: 10.5281/zenodo.3371421; LHCb collaboration, R. Aaij *et al.*, *Measurement of the CKM angle γ from a combination of LHCb results*, JHEP **12** (2016) 087, arXiv:1611.03076.

[118] LHCb collaboration, R. Aaij *et al.*, *Measurement of the CP-violating phase ϕ_s in $\overline{B}_s^0 \to D_s^+D_s^-$ decays*, Phys. Rev. Lett. **113** (2014) 211801, arXiv:1409.4619.

[119] A. Rogozhnikov, *Reweighting with Boosted Decision Trees*, J. Phys. Conf. Ser. **762** (2016) 012036, arXiv:1608.05806.

[120] LHCb collaboration, R. Aaij *et al.*, *Precise determination of the B_s^0-$\overline{B}_s^0$ oscillation frequency*, Nature Physics **18** (2022) 1, arXiv:2104.04421.

[121] K. De Bruyn and R. Fleischer, *A roadmap to control penguin effects in $B^0 \to J/\psi K_S^0$ and $B_s^0 \to J/\psi\phi$*, JHEP **2015** (2015) , arXiv:1412.6834.

[122] LHCb collaboration, R. Aaij *et al.*, *First observations of $\overline{B}_s^0 \to D^+D^-, D_s^+D^-$ and $D^0\overline{D}^0$ decays*, Phys. Rev. **D87** (2013) 092007, arXiv:1302.5854.

[123] LHCb collaboration, R. Aaij *et al.*, *Study of beauty hadron decays into pairs of charm hadrons*, Phys. Rev. Lett. **112** (2014) 202001, arXiv:1403.3606.

[124] LHCb collaboration, *Framework TDR for the LHCb Upgrade: Technical Design Report*, CERN-LHCC-2012-007, 2012.

[125] LHCb collaboration, *Upgrade Software and Computing*, CERN-LHCC-2018-007, 2018.

[126] T. Likhomanenko, D. Derkach, and A. Rogozhnikov, *Inclusive Flavour Tagging Algorithm*, Journal of Physics: Conference Series **762** (2016) 012045, arXiv:1705.08707.

[127] Belle II collaboration, T. Abe *et al.*, *Belle II Technical Design Report*, arXiv:1011.0352.

Danksagung

An dieser Stelle möchte ich mich bei all den Menschen bedanken, die mich während meiner Promotion begleitet und unterstützt haben.

Ein besonderer Dank gilt Bernhard Spaan, der leider viel zu früh von uns gegangen ist. Er hat mir die einzigartige Möglichkeit gegeben, im Bereich der Teilchenphysik zu promovieren, und mich schon während meiner Bachelor- und Masterarbeit betreut. Mit seinem umfangreichen Wissen und seiner humorvollen Art hat er mich stets inspiriert und motiviert. Sein plötzlicher Tod war ein großer Verlust für die gesamte Arbeitsgruppe und alle, die ihm nahestanden.

In dieser schwierigen Zeit musste ich mir jedoch nie Sorgen um das Fortführen meiner Promotion machen, da Johannes Albrecht ohne zu zögern die Betreuung meiner Arbeit übernommen hat. Dafür bin ich ihm zutiefst dankbar. Johannes hat mich bereits mit seiner KET-Vorlesung für die Teilchenphysik begeistert und mich dadurch motiviert, in diesem Bereich zu forschen. Während meiner gesamten Zeit in der Arbeitsgruppe und insbesondere in der Promotionsphase hat er mich immer unterstützt und mir mit wertvollem Rat, auch über die wissenschaftliche Arbeit hinaus, zur Seite gestanden.

Ich danke auch Dominik Elsässer, der sich die Zeit genommen hat, meine Arbeit als Zweitgutachter zu bewerten. Sein Enthusiasmus in der Vorlesung für Astroteilchenphysik hat mich damals angesteckt, und ich hoffe, meine Dissertation konnte etwas von dieser Begeisterung zurückgeben.

Des Weiteren möchte ich mich bei all meinen Kollegen bedanken, mit denen ich während meiner Promotion zusammengearbeitet habe - viele von ihnen sind inzwischen zu guten Freunden geworden: Philipp, mit dem ich gemeinsam an vielen Projekten gearbeitet habe und der mir wahrscheinlich das meiste beigebracht hat; Antje, die mit Philipp und mir zusammen diese Analyse auf die Beine gestellt hat; Conor Fitzpatrick, whose help with the analysis has been invaluable and who has always been there to answer my questions; meinen Bürokollegen Antje, Kevin, Quentin, Fabio, Jan, Jannis, Vukan und Maik, mit denen ich viele schöne Momente geteilt habe; Fabio, Jannis, Jan W., Jan L., Henning, Maik, Martin, Nicole, Quentin und Vukan, die Teile meiner Dissertation gelesen haben und mir mit ihren Kommentaren und Verbesserungsvorschlägen sehr geholfen haben.

Mein Dank gilt auch meinen Freunden, die mich während dieser Zeit begleitet und unterstützt haben. Insbesondere möchte ich Alexander und Jan für die unvergessliche Studienzeit danken, die mir unfassbar viel Spaß gemacht hat.

Meiner Familie danke ich von Herzen für den stets verlässlichen Rückhalt und die Unterstützung, die sie mir während meines Studiums und meiner Promotion gegeben haben. Ohne sie wäre all das nicht möglich gewesen. Zuletzt möchte ich meiner Freundin Maria danken, die mir in dieser Zeit viel Kraft gegeben und mich immer wieder aufgebaut und motiviert hat.